A SUMMARY OF THE RADAR EQUATIONS AND MEASUREMENT TECHNIQUES USED IN THE SAMS RAIN EROSION PROGRAM AT WALLOPS ISLAND, VIRGINIA. AFCRS/SAMS REPORT NUMBER 1

Vernon G. Plank

Air Force Cambridge Research Laboratories
L. G. Hanscom Field, Massachusetts

25 January 1974

Unclassified

Security Classification

AD-778095

DOCUMENT CONTROL DATA - R&D

(Security classification of title, body of abstract and indexing annotation must be entered when the overall report is classified)

1. ORIGINATING ACTIVITY *(Corporate author)*
Air Force Cambridge Research Laboratories (LYC)
L. G. Hanscom Field
Bedford, Massachusetts 01730

2a. REPORT SECURITY CLASSIFICATION
Unclassified

2b. GROUP

3. REPORT TITLE
A SUMMARY OF THE RADAR EQUATIONS AND MEASUREMENT TECHNIQUES USED IN THE SAMS RAIN EROSION PROGRAM AT WALLOPS ISLAND, VIRGINIA. AFCRL/SAMS Report No. 1.

4. DESCRIPTIVE NOTES *(Type of report and inclusive dates)*
Scientific Interim

5. AUTHOR(S) *(First name, middle initial, last name)*
Vernon G. Plank

6. REPORT DATE	7a. TOTAL NO. OF PAGES	7b. NO. OF REFS
25 January 1974	104	40

8a. CONTRACT OR GRANT NO.	9a. ORIGINATOR'S REPORT NUMBER(S)
b. PROJECT, TASK, WORK UNIT NOS. 86200501	AFCRL-TR-74-0053
c. DOD ELEMENT 63311F	9b. OTHER REPORT NO(S) *(Any other numbers that may be assigned this report)*
d. DOD SUBELEMENT	Special Reports, No. 172

10. DISTRIBUTION STATEMENT
Approved for public release; distribution unlimited.

11. SUPPLEMENTARY NOTES	12. SPONSORING MILITARY ACTIVITY
	Air Force Cambridge Research Laboratories (LYC) L. G. Hanscom Field Bedford, Massachusetts 01730

13. ABSTRACT The radar concepts, definitions, and equations that related to the SAMS rain erosion program at Wallops Island, Virginia, are reviewed.

The several radars employed in the program are identified, and their nominal characteristics of usual reference performance are cited. The two methods of calibrating the primary radars are explained, and values of the calibration constants that pertain to the different radars and days of missile launches from 1970 through the spring of 1973 are listed.

The particular radar measurements for each of the three SAMS seasons of operations since 1970 are summarized, and plans for the forthcoming 1973-74 season are indicated.

An uncertainty analysis presented in an appendix permits assessment of the error bounds of the radar reflectivity factors for water and ice hydrometeors, providing that additional special data are obtained for individual Wallops storms.

DD FORM 1 NOV 68 1473

Unclassified

Security Classification

14. KEY WORDS	LINK A		LINK B		LINK C	
	ROLE	WT	ROLE	WT	ROLE	WT
Rain erosion						
Radar meteorology						
Radar calibration						
Precipitation physics						
SAMS - ABRES						
Wallops Island, Virginia						

Preface

The AFCRL program of radar measurements supporting the SAMS rain erosion project at Wallops Island, Virginia during the 1970-73 season was conducted as a joint team effort by various members of the Weather Radar and Convective Cloud Physics Branches of the Meteorology Laboratory, AFCRL. Contractual support was provided by the Applied Physics Laboratory of Johns Hopkins University. The program was directed by Dr. Robert M. Cunningham, of the Convective Cloud Physics Branch, and supervised by Dr. Kenneth R. Hardy, of the Weather Radar Branch.

The AFCRL and contract contributors to the radar measurement program are identified in the following list, and their efforts toward the accomplishment of the SAMS objectives are acknowledged. In addition, thanks are extended to Mr. Alfred A. Spatola and Dr. Kenneth Hardy of AFCRL and Mr. Hugh Church of the Sandia Laboratories, Albuquerque, New Mexico for their review and criticism of the manuscript. Their comments and suggestions were helpful and appreciated.

Name	Organization	Role
Dr. Morton L. Barad	LY*	Director, Meteorology Laboratory
Mr. Chankey N. Touart	LY	AFCRL Program Manager for Weather Erosion Programs June 1973 to present
Dr. Robert M. Cunningham	LYC**	Director of AFCRL Measurement Program at Wallops Island, Virginia

Name	Organization	Role
Dr. Kenneth R. Hardy	LYW†	Supervisor of AFCRL Radar Measurements Program at Wallops Island, Virginia
Mr. Kenneth M. Glover	LYW	
Dr. Arnold A. Barnes, Jr.	LYW	
Mr. Albert C. Chmela	LYW	
Mr. Graham M. Armstrong	LYW	
Dr. Roland J. Boucher	LYW	
Mr. Michael J. Kraus	LYW	
Mr. William E. Lamkin	LYW	
Mrs. Rosemary M. Dyer	LYW	
Mr. Edward F. Duquette	LYW	
Mr. Kenneth J. Banis	LYW	
Mr. Alexander W. Bishop	LYW	
Mr. William A. Smith	LYW	
1/Lt James Metcalf	LYW	
Mr. Hugh J. Sweeney	LYW	
Mr. Wilbur H. Paulsen	LYW	
Mr. Pio J. Petrocchi	LYW	
Mr. Ruben Novack	LYW	
Mr. Vernon G. Plank	LYC	
Mr. Alfred A. Spatola	LYC	
Mr. Donald W. McLeod	LYC	
Mr. Morton Glass	LYC	
Mr. George Ritscher	LYC	
Mr. Elefterios J. Georgian	LYC	
Mr. Russell M. Peirce Jr.	LYC	
Mrs. Elizabeth Kintigh	LYC	
Ms. Barbara Main	LYC	
Ms. JoAnne E. Waters	LYC	
Mr. Jack Howard	APL††	Radar Station mgr. at Wallops Island, Va.
Mr. Norris Beasley	APL	
Mr. Norm Gebo	APL	
Mr. Charles Ponder	APL	
Mr. Herbert Seeman	APL	
Mr. Norman Parker	APL	
Mr. Harold Lord	APL	
Mr. Richard Gagnon	APL	

Name	Organization	Role
Mr. Larry Greer	APL	
Dr. Isadore Katz	APL	
Dr. Thomas Konrad	APL	
Mr. James Meyer	APL	
Mrs. Ella Dobson	APL	
Mr. Donald Takeuchi	MRI†††	
Mr. Alfonso Ollivares	MRI	
Mr. Ralph Martin	MRI	
Mr. Larry Boardman	MRI	

* LY - Meteorology Laboratory, Air Force Cambridge Research Laboratories.
** LYC - Convective Cloud Physics Branch, Meteorology Laboratory.
† LYW - Weather Radar Branch, Meteolology Laboratory.
†† APL - Applied Physics Laboratory, Johns Hopkins University, Silver Springs, Maryland.
††† MRI - Meteorology Research Inc., Altadena, California.

Contents

Contents

Illustrations

Tables

A Summary of the Radar Equations and Measurement Techniques Used in the SAMS Rain Erosion Program at Wallops Island, Virginia

AFCRL/SAMS Report No. 1

1. INTRODUCTION

The general objective of the SAMS rain erosion program at Wallops Island, Virginia is the determination of the erosion effects on the nose-cones of missiles caused by hydrometeors located along the trajectory paths. Missiles are launched into storm situations that move across the Wallops area during the late Fall, Winter and early Spring. Erosion data are obtained from the missiles by in-flight telemetry and by nose-cone recovery and examination, following the flight. Comparison radar, aircraft and surface data are acquired concerning the type, size-distribution and liquid-water-content of the cloud and precipitation particles that existed along the trajectories, or in their vicinity. The erosion and latter data are then correlated in attempts to explain the observed erosion effects and to design theoretical models describing the physical processes involved.

This report, which is the first of a series describing the contributions of the Air Force Cambridge Research Laboratories (AFCRL) to the SAMS program, is concerned with the quantitative radar measurements. The report consists of two major parts. The first part describes the radar concepts, definitions and equations that establish the background of the measurement and analytical

(Received for publication 28 January 1974)

procedures involved. The subject matter, although primarily based on radar theory and literature references, is specifically directed toward the SAMS program, in the sense that the radar systems and parameters discussed are those immediately pertinent to the program.

The second major part of the report, commencing with Section 3, describes the particulars of the Wallops Island radars, the calibration methods, the missile-trajectory measurements and the analyses that were employed during the three seasons of SAMS operation since 1970.

Specific data for individual missile flights are not supplied in the present report. The single exception is the listing of the radar calibration constants. The particular data for the separate flights will be presented in later reports of the series.

Because of report completion deadlines, the subject matter herein is treated in a summary fashion, rather than in comprehensive detail. Also, regarding the various references cited, these are merely particular examples of the work efforts of certain authors in the field. Thus, credit reference is neglected for numerous other authors who have contributed importantly to the theoretical-experimental background.

Various symbols used in this report depart from the standards recommended by the AMS* Committee on Radar Meteorology. Such departures, although minimized, were required because the SAMS program encompasses disciplines other than radar meteorology. Additional parameters will be defined in later reports and there is a need for consistent, non-redundant symbology throughout the totality of the descriptive reporting.

The numerical system of equation reference is used herein. Thus, the equations, in most cases, are referenced by number only.

Forthcoming reports of the series, as presently visualized, will:

(1) Provide background information and explain how the precipitation liquid-water-content and other parameters of erosion interest were determined from the radar data.

(2) Describe the aircraft and surface measurements that provide knowledge of the types and quantities of the cloud and precipitation hydrometeors that existed in the Wallops storm.

(3) Discuss the correlation analyses, involving the aircraft and radar data, which are designed to improve the accuracy of the empirical equations relating the radar-reflectivity-factor (Z) and the precipitation liquid-water-content (M).

(4) Summarize the storm situations of each of the SAMS seasons of operations and present the data results, in profile and tabular form, for the trajectory paths of the eleven SAMS storm missiles launched in the 1970-73 season.

*American Meteorological Society.

These reports will be submitted as analytical and literary progress permits, not necessarily in the order indicated above.

2. REVIEW OF THE PERTINENT RADAR CONCEPTS, DEFINITIONS AND EQUATIONS RELATING TO THE SAMS PROGRAM

Radar equations will be developed in this section which pertain to single, point-source targets and to multiple, hydrometeor, scattering targets. Pulse integration and video integration will be described and the radar equations will be modified for application to radar data acquired by video integration.

2.1 Gain and Beamwidth of a Parabolic Antenna

2.1.1 ISOTROPIC RADIATOR

The power density in space at any given distance from a source of microwave energy that radiates isotropically, is

$$S_I = \frac{P_t}{4\pi r^2} \tag{1}$$

where P_t is the radiated, or transmitted, power at the source, r is the range from the place of power measurement to the source, and S_I is the power per unit area normal to any radial line drawn outward from the source.

2.1.2 RADIATOR WITH GAIN

If the microwave energy emanates from a transmitting antenna, or array, which is shaped or arranged such that the power density in the transmission direction exceeds that of an isotropic radiator, then the maximum power per unit area, or maximum power density, is

$$S_{max} = \frac{P_t G_t}{4\pi r^2} \quad , \tag{2}$$

where G_t is the "antenna gain for transmission".

The general definition of G_t, for example see Kerr[1], is that it is the ratio of the power radiated by an isotropic antenna that is required to produce the same field strength at the same range as that produced by the directional antenna in its direction of maximum transmission. Thus,

---

1. Kerr, D. E. (1951) Propagation of Short Radio Waves, McGraw-Hill, New York.

$$G_t = \frac{S_I \int_{4\pi} d\Omega}{S_o \int_{4\pi} |f(\theta', \phi')|^2 d\Omega} \tag{3}$$

where S_o is the average field strength in the direction of maximum transmission, and $d\Omega$ is a unit solid angle viewed from the transmitter. If the direction of maximum transmission is defined as the polar axis of a spherical coordinate system with its origin at the antenna, the angles θ' and ϕ' are, respectively, the zenith angle from the polar axis and the angle from this axis in the plane perpendicular to the zenith plane. The function, $f(\theta', \phi')$, is the "pattern function" of the particular antenna and is, in general, a complex function of the angles. The term $|f(\theta', \phi')|^2$ describes the range-normalized, polar diagram of the antenna.

If S_I and S_o, in Eq. (3), are set equal, using the general definition of gain stated previously, then, since the numerator term, $\int_{4\pi} d\Omega$, is equal to 4π, the equation may be rewritten as

$$G_t = \frac{4\pi}{\int_{4\pi} |f(\theta', \phi')|^2 d\Omega} . \tag{4}$$

This defines the transmission gain of an antenna.

2.1.3 DEFINITIONS OF BEAMWIDTH AND GAIN FOR A PARABOLIC ANTENNA

If the transmitting antenna is a parabolic dish, as is the case with the Wallops Island radars used for quantitative storm measurements in the SAMS program, the beam pattern that emanates from the antenna consists of a very sharp, well-defined primary lobe of radiation plus various secondary or side lobes. All of these lobes are symmetrical about the polar axis.

The power density of the radiation is a maximum along the polar axis and quickly drops off in value with increasing angular distance from the axis (as viewed from the antenna). If a cross section is drawn through the primary lobe, normal to the polar axis, at any given range which is large compared to the antenna dimensions, the isolines of constant power density on such a spherical section are approximate circles concentric about the polar axis. The particular circle along which the power density is half the maximum defines the "half power circle" of the radiation. The conic surface formed by the integral of all such circles at all ranges has been conventionally employed to define the so-called "beam" of the antenna. This cone, or beam, has a total angular width θ, from one side of the cone to the other, across any plane containing the polar axis. The angle θ is referred to as the "beamwidth".

It is presumed, in this definition, that the actual lobe pattern of radiation can be approximated by a pattern that has uniform intensity out to the conic boundaries. With such a presumption, it may be demonstrated—for example see Austin and Williams[2]—that the transmission gain for a perfectly constructed and illuminated parabolic antenna is related to the beamwidth as

$$G_t = \frac{16}{\theta^2} \quad . \tag{5}$$

Probert-Jones[3] has discussed the several erroneous assumptions that led to this formerly-used relationship. He has demonstrated that the theoretical relationship between the gain and beamwidth of a parabolic antenna is more correctly given by

$$G_t = \frac{\pi^2 K_a^2}{\theta^2}, \tag{6}$$

where

$$K_a^2 = \alpha \beta f^2(\beta) \quad . \tag{7}$$

In this latter equation, α is the fraction of the total power from the feed intercepted by the antenna and β is a factor specifying the uniformity of the antenna illumination. For a perfect antenna, Probert-Jones states that $\alpha = \beta = 1.0$, while $f^2(\beta) = 1.04$, giving $K_a \simeq 1.02$. He also cites other theoretical work to show that K_a, in the ideal case, has a value close to unity.

Of course actual antennas, which are used operationally, depart from the ideal. In such a case, the parameter K_a may be regarded as a "calibration constant" that specifies the actual performance relative to the theoretical. Certain waveguide and radome losses of the transmission system may also be included in K_a, depending on the particular calibration methods used.

For the primary radars employed for the SAMS measurement program at Wallops Island (reference Section 3 for specific identification), it may be stated that the K_a values range from 0.88 to 0.95.

---

2. Austin, P.M., and Williams, E.L. (1951) Comparison of Radar Signal Intensity with Precipitation Rate, Technical Report No. 14, Weather Radar Research Project, M.I.T., Cambridge, Massachusetts.

3. Probert-Jones, J.R. (1962) The radar equation in meteorology, Quart. J. Roy. Meteorol. Soc. 88:485-95.

2.1.4 GAIN IN TERMS OF EFFECTIVE ANTENNA AREA

An alternate expression for the gain of a parabolic antenna, which is important to the subsequent derivations, is (see Silver[4])

$$G_t = \frac{4\pi A_e}{\lambda^2}, \tag{8}$$

where λ is the wavelength of the radiation and A_e is the "effective area" of the antenna. The effective area is related to the actual cross-sectional area of the parabolic dish (across its face, normal to the principal axis) as

$$A_e = K_o A_p, \tag{9}$$

where A_p is the actual area and K_o is a constant of correspondence. From Eqs. (6), (8) and (9), it follows that

$$K_o = \frac{\pi \lambda^2 K_a^2}{4 A_p \theta^2}. \tag{10}$$

The values of this constant, for the primary radars of the SAMS program mentioned earlier, range from 0.44 to 0.66. This is stated without proof, but is easily demonstrated from the radar performance values listed in Tables 4, 5 and 6.

2.2 Single Targets and Continuous Wave Transmission

2.2.1 INCIDENT AND REFLECTED POWER FOR SINGLE ISOTROPIC AND NON-ISOTROPIC TARGETS WITHIN THE BEAM

If a single target of cross-sectional area A_t is present within the antenna beam, the target intercepts an incident amount of microwave power

$$S_i = \frac{P_t G_t A_t}{4\pi r^2}. \tag{11}$$

---

4. Silver, S. (1951) Microwave Antenna Theory and Design, McGraw-Hill, New York.

If the target has a reflection coefficient*, ρ_t, and if it reradiates or "scatters" the incident power isotropically, the power density of the reradiation at any particular range r' from the target, is

$$S_r = \frac{S_i \rho_t}{4\pi r'^2}, \tag{12}$$

or, from Eq. (11)

$$S_r = \frac{P_t G_t \rho_t A_t}{(4\pi)^2 r^2 r'^2}. \tag{13}$$

If the target does not scatter isotropically, it is conventional to define a "backscatter cross section", σ, to replace the geometric cross section $\rho_t A_t$. The values of σ will depart from those of $\rho_t A_t$ depending on such things as the target dimensions relative to the wavelength of the radiation, the aspect angle and curvature properties of the target in the beam, and the wave polarization. However, it is always possible in principle to determine the σ value for any prescribed target.

With σ used to replace $\rho_t A_t$, Eq. (11) becomes

$$S_i = \frac{P_t G_t \sigma}{4\pi r^2 \rho_t} \tag{14}$$

and Eq. (13) is written as

$$S_r = \frac{P_t G_t \sigma}{(4\pi)^2 r^2 r'^2}. \tag{15}$$

2.2.2 POWER RECEIVED FROM A SINGLE TARGET UNDER CONDITIONS OF CONTINUOUS WAVE TRANSMISSION

The equation development is best illustrated at this point by first describing the power received from a single target under conditions of continuous wave (CW) transmission. We may then proceed logically to the more complicated situation of pulsed radar.

---

*The reflection coefficient for metal is 1.0; for other dielectrics, such as water, it is less than 1.0.

As demonstrated in the previous section, the power density of the backscattered radiation from a single target is governed by Eq. (13). Then, assume that this backscattered radiation is received by a second parabolic antenna which is located adjacent to the transmitter and is pointing in the same direction (toward the target) such that the polar axes of the two antennas are closely parallel. Also, assume that there is appropriate shielding between the two such that none of the transmitted radiation directly enters the receiver.

If the effective area of the receiving antenna is A_e', the power intercepted and received by the antenna will be

$$P_r = S_r A_e' \ , \tag{16}$$

where S_r is the power density of the backscattered signal from the target as specified by Eq. (15). With Eq. (15) substituted in Eq. (16),

$$P_r = \frac{P_t G_t \sigma}{(4\pi)^2 r^2 r'^2} A_e' \ . \tag{17}$$

The gain of the receiving antenna G_r is related to the effective area of the antenna A_e' by an equation analogous to Eq. (8); that is,

$$G_r = \frac{4\pi A_e'}{\lambda^2} . \tag{18}$$

This equation, when solved for A_e' and substituted in Eq. (17), yields

$$P_r = \frac{P_t G_t G_r \lambda^2 \sigma}{(4\pi)^3 r^2 r'^2} , \tag{19}$$

which specifies the power received from the target under CW conditions of transmission.

2.3 Radar Equation for a Single Target

Let us now consider the situation in which the transmitting and receiving antennas of the previous example are one and the same, such that

$$G_r = G_t \ , \tag{20}$$

with

$$r' = r \ . \tag{21}$$

Equation (19) then becomes

$$P_r = \frac{P_t G_t^2 \lambda^2 \sigma}{(4\pi)^3 r^4}, \tag{22}$$

which is the "radar equation" for a single target of backscattering cross-section σ.

This equation for single targets may be employed in radar calibrations involving the tracking of a target of known dimensions and backscattering properties, such as a metal-coated sphere suspended by a balloon or parachute. Later reference will be made to this equation in this context.

2.4 Radar Parameters and Equations for Multiple, Hydrometeor Targets

2.4.1 RADAR PULSE LENGTH AND PULSE VOLUME

A radar systematically transmits pulses of brief time duration at a particular pulse repetition frequency (prf). Part of the power in these pulses, as they move out from the radar, is intercepted by any target present within the beam and is scattered back toward the radar, where it is detected by the receiver during the time intervals between pulses.

The radar determines the distance, or range, to the given target by measuring the time interval between the transmission time of the outgoing pulses, to the reception time of the backscatter return pulses. Thus, the range to the target is

$$r = \frac{v_p \Delta t}{2}, \tag{23}$$

where Δt is the time interval measured by the radar and v_p is the velocity of microwave propagation (equal to 3.0×10^{10} cm sec^{-1}). The factor 2 in the denominator accounts for the fact that the radar waves travel a two-way path, to the target and return. Hence, the range is half the total path length.

If the time duration of the transmitted radar pulse is h', then the physical length of the traveling wavetrain that moves outward along the beam, in the r direction, is

$$h = v_p h' \ . \tag{24}$$

Both of these parameters, h', measured in time, and h, measured in length, are customarily referred to as the "pulse length" of the radar. Sometimes they are also referred to as the "pulse width".

The volume of the traveling wavetrain of the radar pulse, as it moves outward within the confines of the conical beam, is

$$V_{WT} = \frac{\pi(r \tan \theta)^2 h}{4}, \tag{25}$$

where $r \tan \theta$ is the diameter of the beam across any major chord, normal to the polar axis, which is measured at the mid-range of the pulse. If θ is a small angle, a fraction of a degree to several degrees, the approximation

$$\theta \simeq \tan \theta , \tag{26}$$

with θ specified in radians, is valid without sensible error, such that Eq. (25) may be simplified to

$$V_{WT} = \frac{\pi(r\theta)^2 h}{4}. \tag{27}$$

Without detailed explanation, it may be stated that the return pulses, which are scattered back to the radar from any ensemble of targets, emanate from within a volume section of the beam that has a length equal to half the pulse length. This occurs, primarily, because the transmitted pulse, and the definition of pulse length, involves a train of waves that are moving in a single direction, outward from the transmitter. The backscatter pulse from the illuminated targets, on the other hand, involves the two-way propagation of radio waves, from transmitter to targets and return. This causes the time duration, or length, of the return pulse to be half the transmitted pulse. (The length of the illuminated volume containing targets, in other words, is half the pulse length.)

Thus, with reference to Eq. (27), the pulse volume of a radar (having a parabolic antenna) is defined to be

$$V = \frac{V_{WT}}{2} = \frac{\pi(r\theta)^2 h}{8} . \tag{28}$$

2.4.2 ECHO RETURN FROM AN ENSEMBLE OF SCATTERERS AND THE CONCEPT OF VOLUME REFLECTIVITY

If an ensemble of scattering targets is present within the pulse volume, each target of which has a particular radar cross-section σ, the summation of the total

backscatter signal within the volume is

$$B = \sum_i \sigma_i \quad . \tag{29}$$

The volume reflectivity, η, is the summed backscatter cross section per unit volume. Hence,

$$\eta = B/V \quad , \tag{30}$$

or, from Eqs. (28) and (30)

$$\eta = \frac{8 \sum_i \sigma_i}{\pi (r\theta)^2 h} \quad . \tag{31}$$

The dimensions of η are L^{-1}.

2.4.3 BASIC RADAR EQUATION FOR HYDROMETEOR PARTICLES

By replacing the σ parameter of Eq. (22), which pertains to a single target, with the analogous $\sum_i \sigma_i$ parameter for an ensemble of hydrometeors, the basic radar equation describing the power received from hydrometeors may be obtained. Specifically, if Eq. (31) is solved for $\sum_i \sigma_i$ and substituted in Eq. (22) to replace σ,

$$P_r = \frac{P_t \lambda^2 G_t^2 \theta^2 h \eta}{512 \pi^2 r^2} \quad . \tag{32}$$

This specifies the amount of power that will be received from hydrometeors within the pulse volume which have a volume reflectivity η.

It should be noted that the received power from hydrometeors decreases as the inverse square of the radar range. In contrast, see Eq. (22), the received power from a single target decreases as the inverse fourth power of the range.

2.5 Other Factors Involved in the Radar Equations

There are five other factors that enter the radar equations in their fully developed form. The first four are factors which, depending on the radar wave length and conditions of operation and whether the targets are point-source targets or multiple hydrometeor targets, act to decrease the received power relative to the amounts specified by Eqs. (22) or (32). The last factor is a units conversion factor that is required because of the non-consistent set of parameter units used operationally.

Each of these factors will be discussed in turn in this Section. However, the radar equations will not be rewritten at each step. They will only be rewritten after all five factors have been described. The work will be summarized at this point and the radar equations will be presented in their fully developed forms.

2.5.1 PROBERT-JONES FACTOR

Probert-Jones[3] has demonstrated that the beamwidth of a parabolic (or other) antenna, for the radar case of two-way transmission with the pulse volume filled with hydrometeors, differs importantly from the beamwidth as defined conventionally for one-way transmission. His work was based on a detailed consideration of the pattern function integrals of the antenna, see Eqs. (3) and (4), and of the shape of the power density profile of the primary lobe of radiation that existed within the conical boundaries of the antenna beam of normal definition.

He found, in essence, that the "effective solid angle", Ω_e, of the conic surface bounding the pulse volume—from which the backscatter contribution to the received power was approximately 99.7 percent of the total (the remainder being contributed by sidelobes)—was related to the solid angle, Ω, of conventional beamwidth definition, as

$$\Omega_e = \frac{\Omega}{2 \ln 2} . \tag{33}$$

This means, from the definition of a solid angle, that the "effective beamwidth", θ_e, for two-way radar transmission with hydrometeor targets, is related to the beamwidth, θ, for one way transmission, as

$$\theta_e^2 = S_B \theta^2 , \tag{34}$$

where S_B, which will be referred to as the Probert-Jones factor, or "beam shape factor", is

$$S_B = \frac{1}{2 \ln 2} = 0.721 . \tag{35}$$

2.5.2 PARTIALLY-FILLED PULSE VOLUME

If the pulse volume is not completely filled with hydrometeors and if there is any way of recognizing such situation a-priori*, it is possible, in theory, to

* The reference is to situations that occur at the side and top boundaries of storm clouds. The radar pulse volume at the boundary range, which intercepts the boundary, contains hydrometeors in one part of the volume but none, only clear air, in the remaining part.

introduce a correction factor, ψ, into the numerator of Eq. (32), to account for the fractional reduction of received power that would occur.

In practice, however—particularly with high performance, high resolution radars having a very narrow beam and small pulse volume—this factor is seldom, if ever, considered, and is, implicitly, assumed to have the value unity.

The assumption that $\psi = 1.0$ was used in all of the radar work and analyses of the SAMS program at Wallops Island.

2.5.3 ATTENUATION FACTOR

Another factor that acts to reduce the received power in precipitation and cloud situations is attenuation. This is a wavelength dependent factor that is normally of negligible importance at the longer wavelengths, longer than S band ($\sim$ 10 cm), but becomes increasingly important as the wavelength is decreased, from S to C band ($\sim$ 5.7 cm), through X band ($\sim$ 3.2 cm) to K band ($\sim$ 0.9 cm).

Attenuation occurs because the microwaves, in traveling to any given range location in the beam, are forced to traverse a two-way path through intervening hydrometeors, which absorb or otherwise (by various scattering mechanisms) cause the microwaves to lose a certain fraction of their power per unit path length. The fraction depends on the type of hydrometeors, on their precipitation rate (or liquid water content, in the case of clouds) and on the radar wavelength, as previously noted.

The attenuation factor, A, which is introduced into the numerator of Eq. (32) or Eq. (22) whenever attenuation is a matter of concern, is specified by

$$A = a_1^{n_1} \times a_2^{n_2} \times \cdots\cdots \times a_i^{n_i} , \tag{36}$$

where a_1, a_2 ..... a_i are the fractional or decimal attenuation values, per unit path length, which pertain to the different types (and quantities) of the hydrometeors that exist along the radar beam at ranges smaller than the particular "target range". The n_1, n_2 ..... n_i exponents of the equation are the number of unit path lengths contained in the two-way traverse distances through each of the hydrometeor regions.

Attenuation equations and values are commonly expressed in decibel form. In such a case, the total dB attenuation is

$$10 \log A = L_1 \times 10 \log a_1 + L_2 \times 10 \log a_2 + \cdots\cdots + L_i \times \log a_i , \tag{37}$$

where 10 log a_1, 10 log a_2, ... 10 log a_i are the "attenuation rates" for the different hydrometeors, in dB per unit path length, and L_1, L_2, ... L_i are the two-way traverse distances through the specific regions.

Particular attenuation equations and values are presented in Table 1, for rain, snow, water cloud and ice cloud. Four radar wavelengths are considered and the equations and values are listed for temperatures, precipitation rates and liquid water contents that are typical of the ones observed in the winter storm situations at Wallops Island during the 1972 and 1973 seasons. The tabulations for the different radar wavelengths are included because of the possibility that C, X or K band radars might be employed in the SAMS program in the future.

The typical, maximum values of attenuation that would be anticipated in the "average" winter storm at Wallops Island are summarized in Table 2. Typical thickness values are listed for the different hydrometeor regions and for the storm in total. Also listed are the two-way traverse distances through the regions for an assumed radar elevation angle of 20°. This angle was chosen because the slant ranges through the regions and storm at such angle are about the maximum to be expected under the SAMS conditions of operation. The attenuation values for these maximum traverse paths are given, in dB, for the same radar wavelengths, precipitation rates and liquid water contents as specified in Table 1.

The table shows that attenuation at S band, even for the maximum values listed, is negligible and can be ignored. Attenuation at C band is indicated to be generally negligible, except under conditions of long traverse distance (to target) or of atypically severe storms. Attenuation at X band is a factor of importance, which should be considered in the radar equations and not neglected. Attenuation at K band is very severe, so severe, in fact, as to suggest that quantitative measurements in this wavelength region would be extremely difficult.

2.5.4 SYSTEM LOSS FACTOR

There are various losses in any radar system that will cause the power received from single targets or hydrometeors to be less than predicted from radar theory. Also, there are various uncertainties concerning the true values of the various parameters that enter the radar equations. For example, it is difficult, if not impossible, to state that the transmitted power, or the pulse length, or even the wavelength, the gain or the beamwidth, had definite, specific values on any given day or period of radar operation.

However, if the radar is calibrated as a system entity—as is the case with the Wallops Island radars used for quantitative measurements, as will be described in a following section—it is possible to collect all of the system losses and uncertainties into a particular "loss factor", L. This factor—if used in the numerator of the radar Eqs. (22) or (32) in conjunction with the particular P_t, h, λ, G_t and θ values, which are the theoretical values for the radar system or are any reference values which reflect the nominal, usual radar performance—provides the means of specifying the actual system performance relative to the theoretical or reference standard.

Table 1. Attenuation Due to Precipitation or Cloud, for a One-way Path. Extracted from Table 13.5 of the Handbook of Geophysics (1960). The decibel values of attenuation, 10 log a, are given for the temperature, precipitation rate and liquid water content values that are typical of the ones observed in the Wallops Island storms of the 1972 and 1973 seasons. The corresponding decimal values of "a", are also listed. P is precipitation rate, in mm hr^{-1}, M is liquid water content, in gm m^{-3}. The P value for snow is in mm hr^{-1} of melted water

Hydrometeor Type and Description of Line Tabulated Item	Wavelength Band and Particular Radar Wavelength			
	S Band λ = 10 cm	C Band λ = 5.7 cm	X Band λ = 3.2 cm	K Band λ = 0.9 cm
RAIN at 18°C				
Attenuation Equation	$10 \log a = -0.0003\ P^{1.0}$	$10 \log a = -0.0022\ P^{1.17}$	$10 \log a = -0.0074\ P^{1.31}$	$10 \log a = -0.22\ P^{1.0}$
For P = 5 mm hr^{-1}, 10 log a =	0.0039 dB km^{-1}	0.0145 dB km^{-1}	0.0609 dB km^{-1}	1.10 dB km^{-1}
For P = 5 mm hr^{-1}, a =	0.9997 km^{-1}	0.9967 km^{-1}	0.9861 km^{-1}	0.7762 km^{-1}
SNOW at -10°C				
Attenuation Equation	$10 \log a = -(0.035\ P^{1.6} + 7.3P) \times 10^{-5}$	$10 \log a = -(0.33\ P^{1.6} + 12.9P) \times 10^{-5}$	$10 \log a = -(3.3\ P^{1.6} + 22.9P) \times 10^{-5}$	Mie Region, Raleigh Approximation not valid
For P = 3 mm hr^{-1}, 10 log a =	0.00022 dB km^{-1}	0.00041 dB km^{-1}	0.00088 dB km^{-1}	------
For P = 3 mm hr^{-1}, a =	0.9999 km^{-1}	0.9999 km^{-1}	0.9998 km^{-1}	------
WATER CLOUD at 0°C				
Attenuation Equation	$10 \log a = -0.0090\ M$	$10 \log a = -0.0272\ M$	$10 \log a = -0.0858\ M$	$10 \log a = -0.99M$
For M = 0.2 gm m^{-3}, 10 log a =	0.0018 dB km^{-1}	0.0054 dB km^{-1}	0.0172 dB km^{-1}	0.1980 dB km^{-1}
For M = 0.2 gm m^{-3}, a =	0.9996 km^{-1}	0.9987 km^{-1}	0.9961 km^{-1}	0.9554 km^{-1}
ICE CLOUD at -20°C				
Attenuation Equation	$10 \log a = -1.80 \times 10^{-4}\ M$	$10 \log a = -3.16 \times 10^{-4}\ M$	$10 \log a = -5.63 \times 10^{-4}\ M$	$10 \log a = -20.0 \times 10^{-4}\ M$
For M = 0.05 gm m^{-3}, 10 log a =	9.0×10^{-6} dB km^{-1}	1.58×10^{-5} dB km^{-1}	2.82×10^{-5} dB km^{-1}	1.0×10^{-4} dB km^{-1}
For M = 0.05 gm m^{-3}, a =	0.999998 km^{-1}	0.999996 km^{-1}	0.999994 km^{-1}	0.999977 km^{-1}

Table 2. Maximum Attenuation Values for Typical Winter Storm at Wallops Island, Virginia. The values are listed for four hydrometeor regions and for the total, two-way, maximum traverse-distances through the regions and storm. A radar elevation angle of 20^{o} is assumed and the P, M and λ values are the same as those of Table 1

Hydrometeor Region	Typical Vertical Depth (including the half depth of the transition zones) (km)	Two Way Traverse Distance for a Radar Elevation Angle of 20^{o} (km)	Maximum Attenuation Values at			
			S Band λ = 10 cm (dB)	C Band λ = 5.7 cm (dB)	X Band λ = 3.2 cm (dB)	K Band λ = 0.9 cm (dB)
1. Rain Region	3.0	17.5	0.0263	0.254	1.066	19.25
2. Snow Region (both large and small snow)	4.5	26.3	0.00577	0.0108	0.0231	--
3. Ice Crystal Region	1.0	5.9	0.000052	0.000092	0.000164	0.00058
4. Water Cloud (summed vertical depth amounts)	5.0	29.2	0.053	0.1577	0.5022	5.78
Maximum Total Values for Storm	8.5 (Sum of 1, 2 + 3 Water Cloud Layers are superimposed)	78.9	0.1271	0.4226	1.5915	> 25.031
		Corresponding A values ⟶	0.9712	0.9073	0.6932	0.00314

The nominal performance characteristics of the Wallops Island radars are listed in Table 3. For purposes of the present report, these listed values are defined to be the ones that specify the reference performance of the radars.

Thus the loss factor L, as defined herein, is the system calibration factor (established for the given day or period) which—if employed in the radar Eqs. (22) or (32) in conjunction with the reference values of P_t, h, λ, G_t and θ, stated in the tables—will permit the numerical evaluation of the constant of relationship between the volume reflectivity η and the received power P_r (for the particular day or period).

These loss factors will be discussed at greater length in Sections 3.3 and 3.4, which are concerned with radar calibrations.

2.5.5 UNITS CONVERSION FACTOR

It has been conventional in the past, or operationally convenient, to employ a variety of units for the different parameters entering the radar equation which do not comprise a consistent set. For example, it is conventional to express P_t in watts or milliwatts, λ in meters or centimeters, r in statute or nautical miles, h in microseconds (whereas h is actually a length unit as it enters the radar equation), and η in m^{-1} or cm^{-1}. The use of such inconsistent units requires that a "units conversion factor", U, be introduced into the radar equations to establish numerical correspondence with a common system of units. Additionally, it should be noted that different units conversion factors will be required, depending on which form of the radar equation is used; that is, "point target form" versus multiple-scattering, "hydrometeor form," and on the specific parameter-units chosen.

It might be contended that, normally, the problem of units conversion should be left to the user of any given equation. However, in the case of the radar equation—with the great diversity of units employed operationally and in view of the fact that improper conversion can cause large errors, if unrecognized—it was deemed essential to define and employ this factor herein.

2.6 Summary and Presentation of the Fully-Developed Equations

To summarize the five factors discussed in the preceding sections, we will rewrite Eqs. (22) (for a point-source target) and (32) (for hydrometeor targets) with all pertinent factors included. The assumptions made for the SAMS radar measurements will then be reviewed and the equations presented in their fully-developed forms.

In the case of a point-source target, the fully-developed equation becomes, from Eq. (22),

$$P_r = \frac{P_t G_t^2 \lambda^2 \sigma A L U_s}{(4\pi)^3 r^4} , \tag{38}$$

where U_s is the particular units conversion factor for the different parameter units employed. The factors S_B and ψ do not enter this equation, since they pertain only to hydrometeor targets.

For hydrometeor targets, Eq. (32) rewritten becomes

$$P_r = \frac{P_t \lambda^2 G_t^2 \theta^2 h \eta S_B \psi A L U}{512 \pi^2 r^2} , \tag{39}$$

where U is another units conversion factor, different than U_s.

It was mentioned in previous sections that $S_B = \frac{1}{2 \ln 2}$ and $\psi = 1.0$ for all SAMS work, and that the attenuation factor A for typical winter storms at Wallops Island, Virginia, was generally negligible at S and C band but was important at X and K band.

With these values inserted in Eq. (39), the radar equation for hydrometeor targets in its fully-developed form, is

$$P_r = \frac{P_t \lambda^2 G_t^2 \theta^2 h \eta A L U}{1024 \ln 2 \pi^2 r^2} , \tag{40}$$

where A is either included or excluded, depending on the particular radar employed. This equation, in its essential respects, was originally derived by Marshall et al.[5]

2.7 Pulse Integration and Video Integration

2.7.1 PULSE INTEGRATOR

In the cloud and precipitation situations of the atmosphere, the radar volume reflectivity η and the associated received power P_r vary widely in value, in an incoherent manner, both temporally, from pulse to pulse of the radar at any given range, and spatially, between range-adjacent pulse volumes during any given pulse. Pulse-to-pulse and range variations of 5 to 10 dB in P_r are common and usual with hydrometeor targets.

5. Marshall, J.S., Langille, R.C., and Palmer, W.M.K. (1947) Measurement of rainfall by radar, J. Meteorol. 4(No. 6): 186-192.

These incoherent signal variations result from the constant "position reshuffling" of the hydrometeor particles within the radar beam. This reshuffling occurs because of the differential fall velocities of the particles of different size, also because of atmospheric turbulence. It causes the summed backscatter cross sections to vary from pulse to pulse and, additionally, there are reinforcements and cancellations of the wavetrains of microwave radiation emanating from the pulse volumes, which also contribute to the incoherent fluctuations.

Atlas[6] has shown that the time required for the scatterers to redistribute themselves sufficiently, by turbulent and differential-fall-velocity motions, to give non-autocorrelated, independent data is

$$\tau \sim 0.00171\,\lambda\,, \tag{41}$$

where λ is in centimeters and τ is in seconds. He also notes that the equation values are in good accord with the times reported by other investigators, such as Bartnoff et al,[7] Fleisher,[8] and Stone and Fleisher.[9]

An instrument component of a radar system, called a pulse integrator, was developed by Williams[10] to provide stable, average values of received power, $\bar{P}_r$, from the pulse-variable, instantaneous values of P_r. The integrator provided an electronic average for the pulses received from a range interval (range gate) equal to one-half the pulse length. From initial data obtained with the instrument, Williams and also Austin and Richardson,[11] found that integration times of one-half second or longer were required to obtain a good statistical average. This corresponded to an average of about 250 separate pulses of the radar. The pulse length of their radar was 1 μsec; the prf was 500, as best judged from their paper.

---

6. Atlas, D. (1964) Advances in radar meteorology, from Advances in Geophysics, 10:317-478, Academic Press, New York.

7. Bartnoff, S., Atlas, D., and Paulsen, W. H. (1952) Experimental Statistics in Cloud and Rain Echoes, Proceedings 3rd Weather Radar Conference, McGill University, 15-17 Sept 1952, G1 to G7.

8. Fleisher, A. (1953, 1954) Information Contained in Weather Noise, M. I. T. Department of Meteorology, Weather Radar Research Technical Report No. 22 A. B.

9. Stone, M. L., and Fleisher, A. (1956) The Measurement of Weather Noise, M. I. T. Dept. of Meteorol, Weather Radar Res, Report No. 26.

10. Williams, E. L. (1949) The Pulse Integrator, Part A: Description of the Instrument and its Circuitry, Technical Report No. 8A, Weather Radar Research Project, M. I. T., Cambridge, Massachusetts.

11. Austin, P. M., and Richardson, C. (1952) A Method of Measuring Rainfall Over an Area by Radar, Proceedings 3rd Weather Radar Conference, McGill University, 15-17 Sept 1952, D-13 to D-20.

The pulse integrator, following these initial experiments, was quickly applied to the hydrological problem of determining areal rainfall amounts from radar measurements. Austin and Richardson[11] and Farnsworth and Mueller[12] described particular versions of the instrument that were designed for this purpose. Considerable development work along these lines was also accomplished during the 1950's and 1960's, which led to further refinements of the Williams' instrument.

The first pulse integrators were essentially analogue devices which provided a temporal-spatial average of the square of the voltage amplitude of the instantaneous received signals. The signals were averaged for a selectable number of individual radar pulses, n_p, and number of range cell elements, n_c. Each of the latter had a length, in the r direction, equal to that of the pulse volume, which is h/2. Thus the integrator, in essence, provided a measure of the average received power

$$\bar{P}_r = \frac{\gamma}{n_c n_p I_m} \sum_{i=1}^{i=n_c} \sum_{j=1}^{j=n_p} E_{ij}^2 \qquad (42)$$

where E is the voltage amplitude of the received signals, I_m is the circuit impedance and γ is a particular constant reflecting the differences between the electronic average and a true average.

Because of the practical difficulties of obtaining $\bar{P}_r$ values for a large number of independent samples spanning the total azimuth angle, range and altitude regions of observational interest to radar meteorologists, and also because of the degradation of signal resulting from integration by analog methods, Marshall and Hitchfield[13] suggested that $\bar{P}_r$ could be determined by counting the fraction of signals exceeding preset threshold levels. This count, assuming that the probability distribution of voltage amplitude is known, is directly related to the average. Confidence limits can also be specified in terms of the ratio of the number of pulses to the number of independent samples, which tells how well the electronic average corresponds to the "true average".* Marshall and Hitchfield presented equations and graphs, based on the so-called "weak law of large

---

* The true average is the arithmetic average over time approaching infinity.

12. Farnsworth, G.W., and Mueller, E.A. (1953) Radar Rainfall Area Integrator, Proceedings Conference on Radio Meteorology, Art. IX-3, University of Texas, Austin.

13. Marshall, J.S., and Hitchfield, W. (1953) The interpretation of the fluctuating echo for randomly distributed scatteres, Part I, Can. J. Phys. 31: 962-994.

numbers", of mathematical statistics—for example see Lindgren and McElrath[14]—which described the relationships between the probability distributions, the radar pulses counted and the independence of the samples. Atlas[6] has reviewed the subject and extended some of the concepts.

Various types of pulse integrators exist, for example see Schaffner[15] and Groginsky,[16] that incorporate different methods of averaging and data presentation. These include (1) analogue techniques of averaging, (2) the classification of signal counts exceeding specified thresholds of signal intensity and (3) computer methods of averaging, classification and processing. In general, though, the measured average received power is related to the true average received power as

$$\overline{P}_r \quad \gamma \overline{P_{r_t}} \quad , \tag{43}$$

where $\overline{P_{r_t}}$ is the true average and γ is an "averaging factor" that depends on the nature of the electronic averaging performed by the pulse integrator, when coupled to a particular radar receiver and when the threshold is adjusted in a prescribed manner. For example, Kodaira[17] has shown that when a logarithmic receiver is used, $\overline{P}_r$ departs probabilistically from the true average dependent on the number of independent data samples averaged by the integrator. When integration is performed for a very large number of samples approaching infinity, $\overline{P}_r \sim 0.562\ \overline{P_{r_t}}$ (that is, $\gamma \quad 0.562$, or -2.5 dB)*. For single independent samples, on the other hand, 50 percent of the received power measurements exceed a threshold level that lies 1.8 dB below the true average such that $\overline{P}_r \quad 0.661\ \overline{P_{r_t}}$ (that is, $\gamma = 0.661$, or -1.8 dB). This illustrates the magnitude of the γ values for one type of receiver and set of assumptions.** Independent samples are discussed at greater length in Appendix A.

---

*Kodaira's equations were actually written in terms of mean square voltage amplitude. However, since the circuit impedance, see Eq. (42), is a constant for any given circuit, the above discussion can be expressed equally well in terms of received power.

**Reference Austin and Schaffner[18] for discussion of the dependence of γ on the spacing of the input quantization.

14. Lindgren, B.W., and McElrath, G.W. (1963) Introduction to Probability and Statistics, The Macmillan Company, New York.

15. Schaffner, M. (1966) A Digital Sweep Integrator for Weather Radar, Proceedings 12th Conference on Radar Meteorology, 17-20 October 1966, Norman, Oklahoma.

16. Groginsky, H.L. (1966) Digital Processing of the Spectra of Pulse Doppler Radar Precipitation Echoes, 12th Conference on Radar Meteorology, 17-20 October 1966, Norman, Oklahoma.

17. Kodaira, N. (1960) The Characteristics of the Averaged Echo Intensity Received by the Logarithmic I.F. Amplifier, Proceedings 8th Weather Radar Conference, Am. Meteorol. Soc., Boston, Massachusetts, pp. 255-261.

18. Austin, P.M., and Schaffner, M.R. (1970) Computations and Experiments Relevant to Digital Processing of Weather Radar Echoes, Proceedings 14th Weather Radar Conference, 17-20 November 1970, Tucson, Arizona.

When a pulse integrator is used as part of a radar system, the radar equation specifying the measured average power received from hydrometeor targets becomes—from Eqs. (40) and (43), assuming that the details of integration are incorporated in the factor γ—

$$\overline{P}_r = \frac{\gamma P_t{}^2 G_r^2 \theta^2 h \bar{\eta} A L U}{1024 \ln 2 \pi^2 r^2}, \tag{44}$$

where $\bar{\eta}$ is the spatial-temporal average of the volume reflectivity, corresponding to that of the integrator. More conveniently, Eq. (44) may be written as

$$\overline{P}_r = \frac{C_r L \bar{\eta}}{r^2}, \tag{45}$$

where

$$C_r = \frac{P_t \lambda^2 G_t^2 \theta^2 h A \gamma U}{1024 \ln 2 \pi^2} \tag{46}$$

is a constant that is herein defined to be "the radar constant of system reference performance". It is seen that the "averaging factor", γ, discussed above, is included in this constant.

It might be noted that the radar equation for a single target, Eq. (38), remains unchanged, in the case of pulse integration. The single target gives a steady, coherent echo (relatively), hence $\overline{P}_r = P_r$, and either the average value or the instantaneous can be employed in the equation.

2.7.2 AFCRL VIDEO INTEGRATOR

The video integrator is a particular modification and developmental extension of the pulse integrator. This instrument, in several versions, was designed by the Weather Radar Branch of AFCRL, for example see Glover,[19] in conjunction with the Raytheon Corporation. Two different models of the instrument were employed in the SAMS program at Wallops Island, Virginia from 1970 to the present.

The AFCRL video integrator, in essence, provides "range normalized" values of a decibel parameter, $\underline{\bar{I}}$, which is related to the integrated volume reflectivity as

$$\underline{\bar{I}} = \underline{\kappa} + 10 \log \bar{\eta}, \tag{47}$$

19. Glover, K. M. (1972) A Precision Digital Video Integrator. Proceedings 15th Weather Radar Conference, Am. Meteorol. Soc., Boston, Massachusetts, p. 193-198.

where $\underline{\kappa}$ is a dB constant that depends on the calibration constant of the radar (discussed in Sections 3.2 and 3.3) and also depends on the particular "sensitivity threshold" that is specified for the integrator when coupled to the radar receiver.*

If the radar equation, Eq. (45), is solved for $\bar{\eta}$ and substituted in Eq. (47) and written in decibel form, we obtain the "operating equation of the video integrator",

$$\underline{\bar{I}} = \underline{\kappa} + 10 \log \left(\frac{P_r r^2}{C_r L} \right). \tag{48}$$

This shows that the integrator, in its effective operation and dependent on the particular calibration and threshold values of L and κ, determines the pulse integrated values of $\bar{P}_r$, provides electronic multiplication or "range normalization" by r^2, and presents the $\underline{\bar{I}}$ values based on the relationship of Eq. (48). This is an oversimplification of the actual operational details of the instrument but basically, the dB values of the integrated signal $\underline{\bar{I}}$ are obtained in this manner.

The AFCRL video integrator also has the design capability to categorize the storm-received $\underline{\bar{I}}$ signals in classes of threshold exceedence. For example, seven selectable classes were available in the video integrator used in the 1971-72 SAMS season. These were set at threshold levels some 3 to 7 dB apart (usually, although 1 dB intervals were also possible), which would subdivide the total $\underline{\bar{I}}$ span of the storm or cloud system into seven different categories of signal intensity. Thus, with the radar in operation in the RHI or PPI scanning modes, the signal levels within the storm could be established for these seven categories for all ranges, elevation angles and azimuth angles of operational interest.

The video integrator additionally permits the signal level classes to be displayed on RHI or PPI scopes, in different "gray shade levels" of video contrast (black, dark gray, light gray and white, with the same shading sequence being repeated once again in an analytically unambiguous fashion). Color contrasts, with television presentation, can also be used to differentiate the various classes of signal level. The Weather Radar Branch of AFCRL is currently designing and contracting for a new video integrator that will provide as many as sixteen classes of color contrast. This integrator will be available for the 1974 season of SAMS operations.

---

*It will be conventional, herein, to use the "bracket underline" symbol "$\underline{\ }$" to specify the decibel equivalent of any given parameter. Thus, with reference to Eq. (47), $\underline{\bar{I}}$ and $\underline{\kappa}$ are, respectively, the decibel equivalents of the actual signal value $\bar{I}$ and the actual calibration constant κ.

To summarize, the AFCRL video integrator provides recorded and real time information about the internal, volume-reflectivity structure of storms and cloud systems. The received signals are averaged for a selectable number of radar pulses, n_p, and for an also selectable number of range cell elements, n_c. The averages are determined and categorized by signal level using the basic, threshold-exceedence techniques of Marshall and Hitchfield.[13] The real time data are graphically portrayed on RHI or PPI scopes, in contoured form with video shading. The recorded data are processed by computer and used in the quantitative analyses of the SAMS program. The nature of the display, recording and processing during the different seasons of operation is discussed in Section 4.

It is pertinent to note that for purposes of the subsequent equation derivations and manipulations herein, considerable simplification is achieved by writing the equations of the video integrator, Eqs. (47) and (48), in their basic, non-dB form. Doing this, Eq. (47) becomes

$$\overline{I} = \kappa \overline{\eta}, \tag{49}$$

and Eq. (48) simplifies to

$$\overline{I} = \frac{\kappa \overline{P_r} r^2}{C_r L}, \tag{50}$$

where $\overline{I}$ and κ are the actual values of the integrated signal and calibration constant, rather than the dB equivalents.

2.7.3 THRESHOLD OR SCALE SETTING OF THE VIDEO INTEGRATOR

When the AFCRL or other video integrator is used as an instrument component of a radar system (coupled to the output of the radar receiver), it is necessary to establish or set the integrator during the process of coupling such that a particular, constant relationship,

$$c = \frac{\overline{I}}{\overline{P_r} r^2} \tag{51}$$

exists among the integration signal $\overline{I}$, the received power $\overline{P_r}$ and the square of the radar range. The constant c will be referred to as the "coupling constant".

In the SAMS program at Wallops Island, the coupling constant was established by determining the particular integration signal $\overline{I}^*$ that corresponded to the minimum received power $\overline{P_r}_{min}$, and was "threshold detectable" at a specified "normalization range", r_n. Under these coupling conditions, Eq. (51) was written as

$$c = \frac{\overline{I}^*}{\overline{P}_{r_{min}} r_n^2} \tag{52}$$

and, since $\overline{I}^*$, $\overline{P}_{r_{min}}$ and r_n were all known, the value of c was computable.

For example, with the FPS-18 radar at Wallops Island in the 1971-72 SAMS season, the threshold received power was set at -90 dBm ($\overline{P}_{r_{min}} = 10^{-9}$ mW) at $r_n = 1.0$ NM. The corresponding value of $\overline{I}^*$ was "set to be" 495.45 (or $\overline{I}^* = 26.95$ dB). Under these conditions, $c = 4.95 \times 10^{11}$ $mW^{-1}cm^{-1}(NM)^{-2}$.

The discussion of the scale-set conditions for the video integrator will not be carried past this point of illustration, at the moment. The specific conditions for the different Wallops radars and SAMS seasons will be described later in Section 3.

2.7.4 RESOLUTION, REPRESENTATIVENESS AND UNCERTAINTY CONSIDERATIONS

When radar data are acquired by use of a pulse or video integrator, various factors must be considered to permit the quantitative assessment of (1) the temporal and spatial resolution of the measurements, (2) the independence and representativeness of the hydrometeor samples included in the integration, and (3) the variance of the measurement values about the probable "true values".

The discussion of these factors is quite involved and hence is presented in Appendix A. Comments about the possible uncertainties of the SAMS radar measurements are included in Appendix B.

Certain of the principal facts and findings of the first of these appendices are summarized below:

(1) Pulse or video integration with hydrometeor targets is necessary in order to obtain stable values of $\overline{P}_r$ or $\overline{I}$, and to permit signal level categorization for purposes of real-time video display of storm echoes and for photographic and/or magnetic tape recording.

(2) Stabilization of the integration signals may be defined as the minimization of the variance of the $\overline{P}_r$ or $\overline{I}$ values, which is achieved by averaging the instantaneous received signals over a number of radar pulses and over multiple range-cell elements.

(3) Excellent signal stabilization may be achieved by integration, but the consequence is that the temporal and spatial resolution of the integrated data are substantially degraded, relative to the resolution values without integration.

(4) The degradation of the temporal resolution is of no practical importance to the SAMS program, since the integration times normally employed are relatively short, on the order of a few tenths of seconds (constant for all radar ranges), which would seem eminently suitable for SAMS purposes.

(5) The degradation of the spatial resolution is a matter of SAMS concern, however, for two reasons: first, that the integration volume (particularly its range extent if multiple range-cells are integrated) is large compared to the spatial resolution of the telemetry data from the missile, the erosion data; and second, that the integration volume is also large relative to the sample volumes of the aircraft measurements (which are correlated with the radar data as will be described in a subsequent report).

(6) The standard deviation of the radar signals received and averaged by a pulse or video integrator is specified approximately by Eq. (A26) of Appendix A. The equation shows that for any given radar having a particular wavelength λ, beamwidth θ and pulse repetition frequency (prf), the standard deviation of the $\overline{P}_r$ or $\overline{I}$ values measured with the integrator will decrease (a) with the number of pulses integrated, that is, with the integration period, (b) with the number of range cells included in the averaging, and (c) with the scan rate of the antenna and wind speed, within certain limitations.

(7) For a radar having a selectable prf, the standard deviation of the pulse or video integrated signals will be minimized by the selection of the largest prf combined with a long integration period and will be maximized by the reverse combination.

(8) The average level of received power or $\overline{I}$, with pulse or video integration, remains the same within the variance limits prescribed by the equation cited above, for any given value of the radar pulse length. Changes in the average power level can only be effected by changing the pulse length; the level increases with h, both for $\overline{P}_r$ and $\overline{I}$.

2.8 The Reflectivity Factor

Up until now, we have not specified the exact nature of the hydrometeor particles which are the scattering targets. This was deliberate, since such consideration involves factors other than purely radar factors.

As can be seen from the radar equation, Eq. (44), a weather radar provides measurements of the volume reflectivity, of the scatterers contained within the radar pulse volume. Thus, a calibrated radar will provide true values of η (or $\overline{\eta}$, in the case of pulse or video integration), irrespective of the nature of the scatterers. The scatterers could be water droplets, ice particles, or even insects or birds. The radar in each case will give an accurate measure of the summed, backscattering, cross-section per unit volume, which is η. It is essential that this fact be clearly understood. To reiterate, the fundamental atmospheric parameter measured by a weather radar is η.

If we have independent knowledge of the nature of the scatters being observed by a radar, microwave scattering theory can then be used to establish the

relationships between the quantity and size distribution of the scatterers and the radar volume reflectivity. In the case of atmospheric clouds and storms, the scattering particles will consist of water droplets, for temperatures above freezing, and ice particles, for temperatures below freezing. There is the additional case of supercooled clouds, which can exist in water form to temperatures well below freezing.

For Rayleigh scattering from an ensemble of water droplets (rain or water cloud), assuming no coherent scattering and ignoring radar pulse-shape considerations, the radar volume reflectivity is given by (see Ryde[20])

$$\eta = \frac{\pi^5}{\lambda^4} k |K|^2 \sum_i N(D_i) D_i^6 , \tag{53}$$

where $N(D_i)$ is the number of droplets per unit volume which have the diameter D_i, and k is a particle shape factor that considers bulk departures of the water drops from spherical shape. The factor $|K|^2$ is a refractive index factor, specified by

$$K = \frac{\epsilon - 1}{\epsilon + 2} = \frac{m^2 - 1}{m^2 + 2} , \tag{54}$$

where ϵ is the dielectric constant of water and

$$m = n - jk' , \tag{55}$$

where n is the refractive index of water, $j = \sqrt{-1}$ and k' is the absorption coefficient for water.

A radar reflectivity factor,

$$Z_W = \sum_i N(D_i) D_i^6 \tag{56}$$

has been defined by Ryde which permits Eq. (53) to be expressed more conveniently as

$$\eta = \frac{\pi^5}{\lambda^4} k |K|^2 Z_W . \tag{57}$$

---

20. Ryde, J.W. (1946) Echo Intensities and Attenuation Due to Clouds, Rain, Hail, Sand and Dust Storms at Centimetre Wavelengths, GEC Report No. 7831, October 1941, also GEC Report No. 8516, Aug. 3, 1944, by J.W. Ryde and D. Ryde, corrections.

The shape factor k in this equation is normally assumed to be unity, that is, the water drops are assumed to have spherical shape.

The refractive index factor, $|K|^2$, for water (see Gunn and East[21]) varies by about 3 percent with the radar wavelength over the λ range from X band (~3.2 cm) to S band (~10 cm). It also varies by about 0.5 percent with temperature, over the temperature range from $0^{\circ}C$ to $20^{\circ}C$.

If we assume an average temperature of $10^{\circ}C$, the Gunn-East data give values of $|K|^2$ of 0.931 at S band, 0.928 at C band, 0.915 at X band, and 0.873 at K band.

Since most of the SAMS radar measurements at Wallops Island were made at S band, it was assumed herein that

$$|K|^2 = 0.93. \tag{58}$$

With this assumption, and with the assumption about the shape factor, Eq. (57) converts to

$$\eta = \frac{0.93\,\pi^5}{\lambda^4} Z_W \ , \tag{59}$$

where the subscript W on Z denotes that this reflectivity factor pertains specifically to water droplets, in the form of rain or water cloud.

For Rayleigh scattering from ice particles (snow, graupel, ice crystals, etc.), the radar volume reflectivity (see Ryde[20]) is given by

$$\eta = \frac{\pi^5}{\lambda^4} k|K|^2 \sum_i N(D_{I_i}) D_{I_i}^6 \ , \tag{60}$$

where D_I is some physical measurement, imprecisely defined, of the actual size of the ice particles, and $N(D_I)$ is the number of particles of this size per unit volume. The other parameters are as previously defined.

Since the refractive index factor divided by particle density, that is, K/ρ_I, is a constant, from the theory of Debye,[22] Mason[23] has defined an effective density-normalized-refractive-index-factor

---

21. Gunn, K.L.S., and East, T.D.R. (1954) The microwave properties of precipitation particles, Quart. J. Roy. Met. Soc. 80:522. (427-8).

22. Debye, P. (1929) Polar Molecules, Chemical Catalog Co., New York, Section 8.1 and Chapter V.

23. Mason, B.J. (1971) The Physics of Clouds, Second Edition, Clarendon Press, Oxford, England.

$$|K'|^2 = \left(\frac{|K|\rho_W}{\rho_I}\right)^2 , \tag{61}$$

where ρ_W is the density of water (equal to unity) and ρ_I is the density of solid ice. By use of this factor, Mason writes Eq. (60) as

$$\eta = \frac{\pi^5}{\lambda^4} k |K'|^2 \sum_i N(D_{e_i}) D_{e_i}^6 , \tag{62}$$

where D_e is the melted, or water equivalent, diameter of the ice particles. He then defines a reflectivity factor, analogous to that for water,

$$Z_I = \sum_i N(D_{e_i}) D_{e_i}^6 , \tag{63}$$

such that Eq. (62) becomes

$$\eta = \frac{\pi^5}{\lambda^4} k |K'|^2 Z_I . \tag{64}$$

Since $|K|^2 = 0.176$ for solid ice, and since $\rho_I = 0.917$ gm cm^{-3}, lensity-adjusted refractive-index-factor of Mason is, from Eq. (61)

$$|K'|^2 = \frac{0.176}{0.917^2} = 0.209 . \tag{65}$$

This value, when inserted in Eq. (64), yields

$$\eta = \frac{0.209\pi^5}{\lambda^4} k Z_I . \tag{66}$$

This gives η for a distribution of ice particles in which the particle sizes are measured in terms of their melted-equivalent diameters. The particle shape factor k, in lieu of other knowledge—and since it is probabilistically likely that irregularly-shaped particles will be randomly oriented within the radar pulse volume—is customarily assumed to be unity.

The η equations for water and ice, Eqs. (59) and (66), when written in terms of the measurement units conventionally employed, become for water

$$\eta = \frac{0.93\pi^5}{\lambda^4} \times 10^{-12} Z_W , \tag{67}$$

with Z_W in $mm^6 m^{-3}$, λ in cm and η in cm^{-1}, and, for ice, with k = 1.0,

$$\eta = \frac{0.209\pi^5}{\lambda^4} \times 10^{-12} Z_I , \tag{68}$$

where the units are the same.

The review of the radar concepts, definitions and equations pertaining to the SAMS measurement program at Wallops Island is terminated at this point. The applications of the equations to the program objectives will be described in the following sections.

3. THE RADAR MEASUREMENT PROGRAM AT WALLOPS ISLAND, VIRGINIA

The general nature of radar measurements and end-product data obtained at Wallops Island, Virginia will be discussed first in this section. The different radars and their performance characteristics will then be described and the two methods of radar calibration will be explained.

3.1 The General Nature of the Radar Measurements and the End-Product Data

During each of the first three SAMS seasons, the general procedure has been to launch the test missiles from the coastline, from "launch pad zero" (see map Figure 1) in the 146° azimuth direction. Thus, the trajectory paths of the missiles were contained in the vertical plane of the 146° azimuth angle from pad zero. The details of the two-stage rockets and payloads have been described by Cole and Robinett, and Cole, Church, and Marshall.

The 146° launch direction was chosen because the primary radars on Wallops Island, used for the SAMS measurements, are located at the Radar Atmospheric Research Facility* (RARF) site, which lies in the 326° azimuth direction from pad zero at a distance of 1.8 NM. This is the reciprocal of the launch direction. In other words, radar measurements made in RHI scan at an azimuth angle of 146° were coplanar with the trajectory paths of the missiles.

The primary radar measurements during each of the seasons were obtained from an S band radar operating in the RHI mode. The end-product data desired from the measurements were the values of the radar reflectivity factor along the course of the missile trajectories at the time of the missile firing, to the best time correspondence possible, dependent on the RHI sweep rate and timing

* This facility is operated by the Applied Physics Laboratory, Johns Hopkins University. The facility is also called the JAFNA (Joint Air Force - NASA) site.

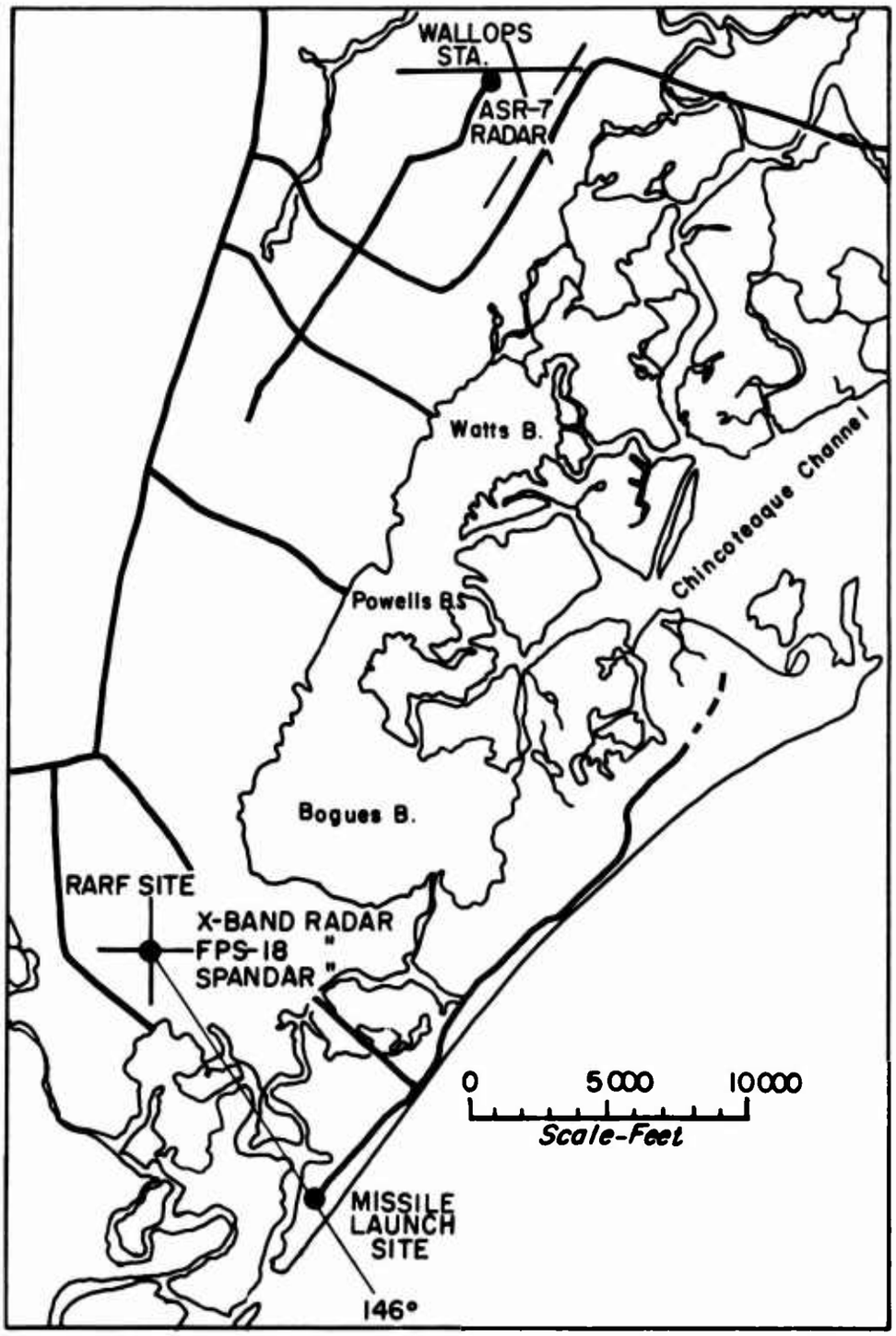

Figure 1. Map of the Wallops Island Area Showing Wallops Station, the RARF Radar Site, and the Missile Launch Site

of the radar antennas. (The hydrometeor parameters were determined from these reflectivity-factor values, as will be described in the second report of the series.) Other radar data of auxiliary type were additionally acquired, as will be explained later.

The values of the radar reflectivity factor were established in the following, step-by-step fashion.

The values of the video-integrated signal, $\overline{I}$, along the missile trajectories were first determined from the launch-time RHI photographs (in the 1970-71 and 1971-72 seasons) or from magnetic-tape records (in the 1972-73 season). Then, from Eq. (49) inverted, that is,

$$\overline{\eta} = \frac{\overline{I}}{\kappa}, \tag{69}$$

and with knowledge of the radar calibration constant κ, the values of the volume reflectivity were computed for each of the trajectory paths. Finally, with cognizance of the height of the melting level within the Wallops storms determined by radar, radiosonde or aircraft, the reflectivity factor Z_W, for the "water hydrometeors" present in the lower portion of the storms, was computed from the $\overline{\eta}$ values by use of Eq. (67) inverted, that is,

$$Z_W = \frac{1.08\,\lambda^4\overline{\eta}}{\pi^5} \times 10^{12}. \tag{70}$$

Likewise, the reflectivity factor Z_I for the "ice hydrometeors" existent in the upper portion of the storms, was computed from Eq. (68) inverted, or

$$Z_I = \frac{4.78\,\lambda^4\overline{\eta}}{\pi^5} \times 10^{12}. \tag{71}$$

Across the melting zone itself, the values of the reflectivity factor were indeterminate. This zone has a finite altitude extent, because the snow particles falling from aloft into warmer, above-freezing temperatures melt gradually with fall distance. The zone is composed of a mixture of water-coated snow particles and liquid droplets, and the radar backscattering properties of the mixture cannot be determined without gross, questionable assumptions.

---

*Radar information about the melting level can be acquired because this level commonly, but not invariably, shows up on the RHI or other scope presentations as a distinctive "bright band". Reference page 66 for additional comments about the melting level and bright band.

Comparing Eq. (69) with Eqs. (70) and (71), it is readily seen that the end-product values of Z_W and Z_I could have been computed directly from the $\overline{I}$ data. The average volume reflectivity, $\overline{\eta}$, is merely an intermediate parameter in the calculations and was computed only because of its fundamental importance in radar meteorology. In other words, $\overline{\eta}$ may be eliminated between Eqs. (69) and (70) to obtain

$$Z_W = \frac{1.08\,\lambda^4 \overline{I}}{\pi^5 \kappa} \times 10^{12}, \tag{72}$$

and between Eqs. (69) and (71) to obtain

$$Z_I = \frac{4.78\,\lambda^4 \overline{I}}{\pi^5 \kappa} \times 10^{12}. \tag{73}$$

These equations show the direct relationship between the radar signal values measured by the video integrator and the desired end-product values of Z_W and Z_I. The only parameter of these equations not yet described is the radar calibration constant κ. We will explain how the values of this constant were determined following the description of the Wallops Island radars and their particular performance characteristics.

3.2 The Radars and Their Performance Characteristics

Although casual reference has been made to the several radars employed in the SAMS program, we have not specifically identified the radars nor stated their locations and performance characteristics. With the background terminology and equations now established, we may proceed to these descriptions.

Five radars have been employed in the SAMS program to date, for various purposes.* Their specific locations and nominal performance characteristics are given in Table 3. Their map locations, except for the WSR-57 radar at Patuxent River, Maryland are shown in Figure 1.

The primary radars used for quantitative measurements were the FPS-18, S band radar (employed in all seasons to date), the RARF X band radar (utilized in the 1970-71 season) and the Spandar, S band radar (used in the 1971-72 and 1972-73 seasons).** All of these radars are located at the RARF, JAFNA, site on Wallops Island, referenced previously.

*These do not include the radars used for missile-tracking or aircraft tracking.

**The FPS-18 radar is also called the "monopulse radar".

Table 3. Nominal Performance Characteristics of Reference for the Radars Employed in the SAMS Program. The values stated are the values normally used in the SAMS program, although various ranges and choices could be selected concerning certain of the parameters

Item or Parameter	Symbol	RADARS					Units
		RARF FPS-18 S Band	RARF Spandar S Band	RARF X Band	ASR-7 S Band	WSR-75 S Band	
Location						Patuxent River, Maryland	
Latitude		$37^{o}51'23''$	$37^{o}51'17''$	$37^{o}51'20''$	$37^{o}56'$	$38^{o}17'$	North
Longitude		$75^{o}30'41''$	$75^{o}30'47''$	$75^{o}30'44''$	$75^{o}28'$	$76^{o}25'$	West
Frequency	f	2807	2840	9280	2800	2880	MHz
Wavelength	λ	10.7	10.5	3.23	10.7	10.4	cm
Trans. Power	P_t	3.05×10^{9}	4.02×10^{9}	1.0×10^{9}	0.425×10^{9}	0.5×10^{9}	mW
Pulse Duration	h'	0.5	2.0	2.1	0.833	4.0	μsec
Pulse Length	n	1.5×10^{4}	6.0×10^{4}	6.3×10^{4}	2.5×10^{4}	12.0×10^{4}	cm
Pulse Rep. Freq.	prf	960	328	320	1200	545	pulses per sec
Antenna Type		Parabolic	Parabolic	Parabolic	Cosecant Squared	Parabolic	
Antenna Dimen.		18.29 dia	18.29 dia	10.36 dia	2.74×5.18	3.66 dia	m
Antenna Area	A_p	262.7	262.7	84.34	11.16	10.51	m^2
Antenna Gain	G_t	1.259×10^{5}	1.259×10^{5}	6.310×10^{5}	0.0251×10^{5}	0.0724×10^{5}	non-dimensional
Antenna Beamwidth	θ	0.48	0.42	0.21	1.5×30	2.2	degrees
Antenna Scan Rate	β	0 to 4 in El.	0 to 17 in El.	0 to 4 in El.	No Capability		deg sec^{-1}
Antenna Scan Rate	β	0 to 8 in Az.	0 to 12 in Az.	0 to 8 in Az.	0-72 in Az.	0-24 in Az.	deg sec^{-1}
Revr. Sensitivity	$P_{r_{min}}$	6.31×10^{-12}	2.00×10^{-12}	2.51×10^{-11}	1.58×10^{-11}	1.58×10^{-11}	mW
Beam Shape Factor	S_B	0.721	0.721	0.721	0.721	0.721	non-dimensional
Beam Filled Factor	ψ	1.0	1.0	1.0	1.0	1.0	non-dimensional
Attenuation Factor	A	Negligible =1.0	Negligible =1.0	To be considered	Negligible =1.0	Negligible =1.0	non-dimensional non-dimensional
Units Conversion Factors							
For Single Target	U_s	8.480×10^{-22}	8.480×10^{-22}	8.480×10^{-22}	8.480×10^{-22}	8.480×10^{-22}	$(NM)^4\ cm^{-4}$
For Hydrometeor Targets	U	8.736×10^{-7}	8.736×10^{-7}	8.736×10^{-7}	8.736×10^{-7}	8.736×10^{-7}	$(NM)^2\ cm^{-1}\ (\mu sec)^{-1}$

Table 3 (Contd.) Nominal Performance Characteristics of Reference for the Radars Employed in the SAMS Program. The values stated are the values normally used in the SAMS program, although various ranges and choices could be selected concerning certain of the parameters

Parameter of Item	Symbol	RADARS AND SEASONS OF USE								Units
		FPS-18 Radar			Spandar Radar		RARF X Band	ASR-7	WSR-57	
		1970-71	1971-72	1972-73	1971-72	1972-73	1970-71	1970-73	1970-73	
Constant of Radar Reference Performance for single targets	k_r	2.36×10^{-3}	2.36×10^{-3}	2.36×10^{-3}	3.00×10^{-3}	3.00×10^{-3}	1.78×10^{-3}	1.31×10^{-3}	1.21×10^{-3}	mW $(NM)^4$ cm^{-2}
Typical or Assumed Value of System Loss Factor	L	~0.05 Assumed	0.057	0.074	~0.022 Assumed	0.022	~0.016 Assumed	~0.05 Assumed	~0.05 Assumed	Non-dimensional
Was Video Integrator Used		Yes	Yes	Yes	No	Yes	No	No	No	-----
Averaging Factor	γ	0.398	0.537	0.537	1.0*	0.537	1.0*	1.0*	1.0*	Non-dimensional
Coupling Constant	c	Unknown	1.30×10^{7}	1.30×10^{7}	--	5.14×10^{7}	--	--	--	$mW^{-1} cm^{-1} (NM)^{-2}$
Radar Constants of Reference for Hydrometeor Targets and Minimum Detectable Values of the Reflectivity Factors for water and ice hydrometeors										
a. Without Video Integration for r = 10 NM	C_r	2.43×10^{7}	2.43×10^{7}	2.43×10^{7}	9.42×10^{7}	9.42×10^{7}	1.46×10^{7}	**4.37×10^{5}	2.09×10^{6}	$(NM)^2$ cm mW
(assumes $P_{r_{min}}$ Receiver sensitivity)	$Z_{w_{min}}$	0.0233	0.0204	0.0157	0.00412	0.00412	0.00411	3.33	0.622	mm^6 m^{-3}
	$Z_{I_{min}}$	0.106	0.0934	0.0719	0.0183	0.0183	0.0183	14.8	2.77	mm^6 m^{-3}
b. With Video Integration, for r = 10 NM	C'_r	9.67×10^{6}	1.30×10^{7}	1.30×10^{7}	--	5.06×10^{7}	--	--	--	$(NM)^2$cm mW
	$Z_{w_{min}}$	† Unknown	6.24	2.83	--	†† 2.11 1.22	--	--	--	mm^6 m^{-3}
	$Z_{I_{min}}$	† Unknown	27.6	12.5	--	9.43 5.42	--	--	--	mm^6 m^{-3}

* When video integrator not used, the values of γ = 1.0, by implication.

** Assumes that a cosecant squared antenna can be approximated by one of elliptical type.

† Unknown because coupling constant unknown, due to use of variable coupling attenuator.

†† See footnote (†) of explanation for two sets of numbers at bottom of Table 4.

Video integrators were used as system components for all quantitative measurements obtained from the FPS-18 radar and also from the Spandar radar, in the 1972-73 season. Several types of integrators were used and improved, season by season. Different methods of data recording and analysis were also used, as will be explained in Section 4.

In addition to these primary, data-gathering radars, there were two other radars that were utilized in a qualitative manner, for storm monitoring and launch-planning purposes. These were the ASR-7 airport surveillance radar located at Wallops Station about 6 miles NNE of the RARF site (see Figure 1), and the WSR-57 radar located at Patuxent River, Maryland, about 60 NM to the NW. The PPI pictures of the ASR-7 radar were transmitted to the RARF site and presented on closed-circuit television for real-time viewing. Facsimile reproductions of the WSR-57 radar PPI photos were available at the U.S. National Weather Service facility at Wallops Station and were used for mission-planning purposes.

The information for the ASR-7 and WSR-57 radars is presented herein because questions about the relative detection capabilities of these radars and the primary radars occasionally arise during planning operations. Table 3 provides approximate answers.

The reader will note that certain of the parameter values in Table 3 have been estimated or left unstated. This reflects a lack of calibration information or knowledge about the particular parameter.

3.3 Sphere Calibration of the Primary Radars

One method of calibrating the primary radars was the so-called "sphere calibration method". A metal-coated sphere, of known diameter, radar reflectivity and backscattering cross section was either carried aloft by a balloon or suspended from a parachute (dropped from a balloon or aircraft) and was tracked by the radar. The range of the sphere from the radar was known, from the echo distance, and the calibration procedure involved the monitoring and recording of the power received from the sphere as a function of range.

In the performance of such calibration, the equation for a point-source target, Eq. (38), is rewritten as

$$P_r = \frac{k_s \sigma}{r^4} , \tag{74}$$

where k_s is the "sphere calibration constant", specified by

$$k_s = k_r L_r , \tag{75}$$

where L is the system loss factor, as defined in Section 2.5.4, and

$$k_r = \frac{P_t G_t^2 \lambda^2 A U_s}{(4\pi)^3} \tag{76}$$

is the constant of radar reference performance, for a point-source target.

In the sphere calibration, the values of k_s are determined directly from the measurements of received power versus range. Thus, Eq. (74) is written as

$$k_s = \frac{P_r r^4}{\sigma}, \tag{77}$$

and, since the σ of the target-sphere is known, and since paired data sets of the P_r and r values are also known by measurement, the particular constant value of k_s can be determined. It might be mentioned that the sphere calibration can be performed either with or without video integration, since the single, spherical, target scatters coherently, without (appreciable) pulse to pulse variation of received power. Hence, $\overline{P}_r \sim P_r$, and either can be employed in Eq. (77).

Once k_s is known, it is a simple matter to ascertain the associated values of the system loss factor L. The constant k_r is first evaluated, from Eq. (76), for the reference performance values listed in Table 3. (In fact, k_r is one of the listed items.) Then, from Eq. (75), written as

$$L = \frac{k_s}{k_r}, \tag{78}$$

the loss factors may be computed.

Sphere calibrations were performed for the FPS-18 radar for all seasons, for the X band radar in the 1970-71 season and for the Spandar radar in the 1971-72 and 1972-73 seasons. The values of k_s and L for these radars and seasons are shown in Table 4. The dates listed are those of the missile launchings. The sphere calibrations were not performed on these exact dates, only during the general periods. However, the values are presumed applicable to the identified days of missile firing.

The particular calibration constant that directly enters the basic computational equations of the SAMS radar program, see Eqs. (72) and (73), is the system calibration constant κ. The values of this constant were determined from those of k_s as follows.

Table 4. Values of Sphere Calibration Constant, Loss Factor, Coupling Constant and System Calibration Constant, Plus Associated Parameters, for the SAMS Primary Radars Used in the Three Seasons Since 1970

Season and Date	Radar	Sphere Calibration Constant and System Loss Factor			Parameters of Coupling Equation and Coupling Constant				Ref. Const. of Radar Eqn.	Corresponding Values of	
		$^{*}k_s$	k_r	L	$\bar{P}_{r_{min}}$	r_n	$\bar{I}^{*}$	c	C_r	System Calibration Constant κ	Calibrated Constant of Radar Eqn. C
		$mW(NM)^4cm^{-2}$	$mW(NM)^4cm^{-2}$	(non-dim).	(mW)	(NM)	(cm^{-1})	$mW^{-1}cm^{-1}(NM)^{-2}$	$(NM)^2cm\,mW$	(non-dim.)	$(NM)^2cm\,mW$
1970-71											
15 Mar 71	FPS-18	1.14×10^{-4}	2.36×10^{-3}	0.0483	(Unknown, Coupling Attenuator Used)				9.67×10^{6}	Unknown	4.67×10^{5}
26 Mar 71		1.259×10^{-4}	2.36×10^{-3}	0.0533	(Unknown, Coupling Attenuator Used)				9.67×10^{6}	Unknown	5.15×10^{5}
March 71	X Band	2.82×10^{-4}	1.78×10^{-3}	~0.0158	(Video Integrator not used)				1.46×10^{7}	Non-Pertinent	$\sim 2.31 \times 10^{5}$
1971-72**											
3 Feb 72	FPS-18	0.724×10^{-4}	2.36×10^{-3}	0.0307	1.0×10^{-9}	1.0	495.5	4.96×10^{11}	1.30×10^{17}	1.98×10^{17}	3.99×10^{5}
17 Feb 72		1.445×10^{-4}	2.36×10^{-3}	0.0612	1.0×10^{-9}	1.0	495.5	4.96×10^{11}	1.30×10^{7}	3.95×10^{17}	7.96×10^{5}
17 Mar 72		1.259×10^{-4}	2.36×10^{-3}	0.0533	1.0×10^{-9}	1.0	495.5	4.96×10^{11}	1.30×10^{7}	3.44×10^{17}	6.93×10^{5}
22 Mar 72		1.259×10^{-4}	2.36×10^{-3}	0.0533	1.0×10^{-9}	1.0	495.5	4.96×10^{11}	1.30×10^{7}	3.44×10^{17}	6.93×10^{5}
Feb & Mar 72	Spandar	$\sim 0.661 \times 10^{-4}$	3.00×10^{-3}	~0.0220	(Video Integrator not used)				9.42×10^{7}	Non-Pertinent	$\sim 2.07 \times 10^{6}$
1972-73											
2 Feb 73	FPS-18	1.778×10^{-4}	2.36×10^{-3}	0.0753	5.89×10^{-10}	1.0	495.5	8.42×10^{11}	1.30×10^{7}	8.24×10^{17}	9.79×10^{5}
27 Feb 73		1.698×10^{-4}	2.36×10^{-3}	0.0719	5.89×10^{-10}	1.0	495.5	8.42×10^{11}	1.30×10^{7}	7.87×10^{17}	9.35×10^{5}
Feb 73 †	Spandar	0.661×10^{-4}	3.00×10^{-3}	0.0220	5.37×10^{-10} also 3.16×10^{-10}	1.0	495.5	9.23×10^{11} also 15.68×10^{11}	5.06×10^{7} 5.06×10^{7}	10.03×10^{17} also 17.45×10^{17}	1.13×10^{6}

* The k_s values were measured in units of $mW(NM)^4m^{-2}$ and converted into the equation units indicated.

** The table values for 3 Feb 1972 apply to one transmitter operation of the FPS-18, as was the situation for the data obtained.

† Two different values of $\bar{P}_{r_{min}}$, that is, values of -92.7 and -95.0 dBm, were used with the Spandar radar in the 1972-73 season, hence the explanation of the dual values of $\bar{P}_{r_{min}}$, c and κ.

From Eq. (50), the equation of the video integrator, we may solve for κ to obtain

$$\kappa = \frac{C_r L \bar{I}}{\bar{P}_r r^2}, \tag{79}$$

where C_r is the reference constant of the radar equation pertaining to hydrometeor targets, as given by Eq. (46)

Since the system loss factor L is specified by Eq. (78), we may also write Eq. (79) as

$$\kappa = \frac{C_r c k_s}{k_r}, \tag{80}$$

where

$$c = \frac{\bar{I}}{\bar{P}_r r^2} \tag{81}$$

is the "coupling constant" that depends on the particular "scale set relationship" that is established among $\bar{I}$, $\bar{P}_r$ and r when the video integrator is coupled to the radar receiver and used to obtain measurements.

The AFCRL video integrator, as discussed in Section 2.7.3, was coupled to the receiver such that a particular integration signal $\bar{I}^*$ was received in association with a specified minimum received power $\bar{P}_{r_{min}}$, that was "threshold detectable" at a normalization range r_n(1 NM). Under these coupling conditions the constant c, of Eq. (81), had (was "set" to have) the definite value

$$c = \frac{\bar{I}^*}{\bar{P}_{r_{min}} r_n^2} . \tag{82}$$

Different coupling relations were used for the different radars and SAMS seasons of operations. The particular $\bar{P}_{r_{min}}$, r_n, $\bar{I}^*$ and c values are listed in Table 4, columns 6 through 9.

The desired values of the system calibration constant κ were computed from the k_s values, utilizing Eq. (80) and knowing the values of k_r, C_r and c. The resultant κ values for the different radars and seasons are presented in Table 4, column 11.

One other parameter was also computed. This was the "calibrated value" of the constant,

$$C = C_r L , \tag{83}$$

of the basic radar equation for hydrometeor targets, Eq. (45), which permitted the specific equations for the individual days to be written as

$$\bar{P}_r = \frac{C\bar{\eta}}{r^2} . \tag{84}$$

The C values are shown in the last column of Table 4.

3.4 The Disdrometer Method of Radar Calibration

The second method of radar calibration, which will be called the "disdrometer method", is a more direct and straightforward method, equationwise, than that of the sphere method, but it is also considerably more difficult to accomplish, instrumentally and analytically.

The disdrometer method of calibration is based on the fact that the system calibration constant κ can be computed directly from Eq. (72), when it is written as

$$\kappa = \alpha \frac{\bar{I}}{Z_W} , \tag{85}$$

where

$$\alpha = \frac{1.08\,\lambda^4 \times 10^{12}}{\pi^5} . \tag{86}$$

The values of Z_W, of Eq. (85), were determined from surface measurements of the size distribution of raindrops. The measurements were made with "disdrometer instruments", as will be described. Simultaneous radar measurements of the video-integrated signal $\bar{I}$, in the numerator of Eq. (85), were obtained from the spatial volume of the storm located as close as possible, above the site location of the disdrometers. Independent sets of Z_W and $\bar{I}$ values were acquired for a period of dual measurement which extended an hour or so (usually) on either side of the launch time(s) of the missiles. These sets of values were then employed, in conjunction with Eq. (85), in comparison and correlation analyses that led to the establishment of the average value of κ that pertained to the calibration periods.

Two disdrometer instruments were employed for radar calibration. (Other instruments were also operated but for other purposes.) These two disdrometers were located at the launch site of the missiles, at "pad zero" (see the map of Figure 1). The second instrument provided a "data consistency check and back-up capability" for the first. These disdrometers, on days of planned missile launching, were operated from about 1 1/2 hours prior to the scheduled launch time to about 1 1/2 hours following launch.

Comparison radar data were obtained throughout the operational period of the disdrometers. The radar being calibrated was periodically aimed in the 146° azimuth direction of the disdrometer site and RHI, A scope, or other data were obtained. From analyses of these data, the $\bar{I}$ values were determined which prevailed about 1.3 km offshore of the disdrometer site at altitudes about 0.2 to 0.4 km above the sea surface. Radar data could not be obtained from directly above the disdrometer site, because the coastline, the launch towers and the other buildings at the site produced "ground clutter return" that masked the desired precipitation echoes. Radar data had to be obtained from beyond the shoreline and the 1.3 km distance-discrepancy between the site locations of the disdrometer and radar measurements had to be tolerated in the calibration .

With these introductory comments, we may now describe how size-distribution and Z_W information was acquired from the disdrometer instruments.

The disdrometers used in the SAMS program were designed and constructed by Joss and Waldvogel.[24-26] These instruments, in essence, measure the impact momentum of raindrops of the various sizes that fall on an exposed sensing head (of 50 cm^2 area).* The instrument is primarily sensitive to the vertical component of momentum resulting from the gravitational fall of the drops, and is relatively insensitive to the horizontal components of momentum associated with wind and turbulent transport.

*The sensing head consists basically of a receiving body of inverted, conical shape which is composed of styrofoam and capped by an aluminum disk. This receiving body is spring-suspended within a containing cylinder such that the capping disk is horizontally-exposed to the precipitation. Two coils are attached to the lower part of the receiving body, their axes vertical. These coils, on droplet impact, are forced downward through a surrounding electromagnetic field. The current induced in the lower coil is amplified and used to provide a counter restoring-current and force in the upper coil. The amplitude of the current in the upper coil is a measure of the drop size.

24. Joss, J., and Waldvogel, A. (1970a) A Disdrometer for Raindrops, Instruction Manual, Marc Weibel Dipl. Ing., ETH, Kapellenstrasse 20, 4000 Basel, Switzerland.

25. Joss, J., and Waldvogel, A. (1970b) Disdrometer RD-69, Instruction Manual. Marc Weibel Dipl. Ing., ETH, Kapellenstrasse 20, 4000 Basel, Switzerland.

26. Joss, J., and Waldvogel, A. (1970c) Analyses AD-69, Instruction Manual. Marc Weibel Dipl. Ing., ETH, Kapellenstrasse 20, 4000 Basel, Switzerland.

The electronic measure of impact momentum, assuming careful calibration of the instrument components (sensing head, processor and recorder), is converted into counts of the number of drops in 20 diameter classes (as many as 20, depending on the size range of the rain) that have fallen onto the sensing head in a fixed time interval. To be more specific, the instrument provides a measure of the number flux of the drops, $N_f(D_i)$, of a classified, mid-diameter-size D_i, that have fallen on the sensing area A_s in the time interval Δt_s.

The rainfall rate, R, is directly determinable from these number flux measurements. It is given by

$$R \quad \frac{6\pi}{A_s \Delta t_s} \sum_{i=D_{min}}^{i=D_{max}} N_f(D_i) D_i^3 \quad \frac{mm}{hr} \quad , \tag{87}$$

where D_i is measured in mm, D_{min} and D_{max} are the minimum and maximum diameters observed, and A_s is specified in cm^2 with Δt_s in seconds.

The number-flux data acquired by disdrometers may be utilized to reconstruct, or synthesize, the probable concentration-and-size-distribution-properties of the raindrops in space, as they existed per unit volume above the disdrometer sensing head just prior to their gravitational fall onto the head. Marshall et al[5] have described the mathematics of this reconstruction, which involves an assumption about the fall velocity of the raindrops as a function of their diameter.

The experiments of Spilhaus,[27] Gunn and Kinzer,[28] Liu and Orville[29] and others have shown that the fall velocity of raindrops, within the restricted size range of normal drop sizes, varies with diameter approximately as

$$V_R = a D_i^b \ \frac{cm}{sec} \quad , \tag{88}$$

for D_i (classified data) specified in mm. The constant a, depending on investigator, varies from about 300 to 500 in equation consistent units, and the exponent b varies from about 0.5 to 0.8.

---

27. Spilhaus, A.F. (1948) Raindrop size, shape, and falling speed, J. Meteorol. 5:108-110.

28. Gunn, R., and Kinzer, G.D. (1949) The terminal velocity of fall for water droplets in stagnant air, J. Meteorol. 6:243. (565, 594, 596-7).

29. Liu, J.Y., and Orville, H.D. (1968) Numerical Modelling of Precipitation Effects on Cumulus Cloud, Report 68-9 Inst. Atmos. Sci., South Dakota School of Mines and Technology, Rapid City, South Dakota.

From this equation for fall velocity, the volumetric concentration of the raindrops in space, $N(D_i)$, can be deduced from the number flux data provided by the disdrometer instruments. Thus, for any given diameter class D_i,

$$N(D_i) = \frac{N_f(D_i)}{A_s \Delta t_s V_R} \quad \frac{No.}{cm^3} \quad , \tag{89}$$

or, from Eq. (88),

$$N(D_i) = \frac{N_f(D_i) \times 10^6}{a D_i^b A_s \Delta t_s} \quad \frac{No.}{m^3} \quad , \tag{90}$$

where $N(D_i)$ in the latter equation is expressed in the conventional units of number per m^3.

With knowledge of $N(D_i)$ thus determined, the values of the radar reflectivity factor for water drops could be computed by writing Eq. (56) as

$$Z_{W_D} = \sum_{i=D_{min}}^{i=D_{max}} N(D_i) D_i^6 \tag{91}$$

and employing Eq. (90) to obtain the computational equation

$$Z_{W_D} = \frac{10^6}{a A_s \Delta t_s} \sum_{i=D_{min}}^{i=D_{max}} N_f(D_i) D_i^{(6-b)} \quad \frac{mm^6}{m^3} \quad . \tag{92}$$

The subscript "D" on Z_W signifies that this is a particular reflectivity factor, computed from disdrometer measurements.

The Z_{W_D} values, in practice, were determined by computer from magnetic-tape records of the number flux data of the disdrometers. Numerous other cloud physics and radar parameters, such as the precipitation liquid water content

$$M = \frac{\pi \rho_w \times 10^3}{6 a A_s \Delta t_s} \sum_{i=D_{min}}^{i=D_{max}} N_f(D_i) D_i^{(3-b)} \quad \frac{gm}{m^3} \quad , \tag{93}$$

where ρ_W is the density of water in gm cm^{-3}, were also computed, as will be mentioned in subsequent reports.

With this background about the disdrometer instruments and about the Z_{W_D} computations, we may now return to the subject of radar calibration.

It should first be noted that the only RARF radar that was calibrated by the disdrometer method was the FPS-18. Calibrations were performed for the 1970-71 and 1971-72 seasons but none was accomplished for the 1972-73 season. Initial attempts were made to calibrate the FPS-18 radar for the 1972-73 season but the results, at least for the day of 27 February 1973, revealed an apparent, substantial discrepancy between the disdrometer and sphere method results. This discrepancy has not yet been resolved. It is suspected that the disdrometer data for the day may have been inaccurate, due to lack of instrument sensitivity or possibly because of improper instrument exposure. (The sites and exposure were changed between the 1971-72 and 1972-73 seasons.)

The following discussion pertains strictly to the disdrometer calibrations that were performed for the FPS-18 radar during the 1971-72 season. This will serve to illustrate the general method of calibration.

The radar data provided for calibration purposes in the 1971-72 season consisted of A scope values of the video-integrated signal $\underline{\bar{I}}$ (in dB) that were obtained from the "low elevation angle" portion of RHI sweeps that had been made in the 146° azimuth direction on the days of missile firing. The data were read from the recorded A scope traces at radar ranges of 4.6 and 5.6 km and at elevation angles of 0.5° and 0.75°. The four values obtained were averaged and this average was presumed representative of the radar echo conditions in the rain at a distance 1.2 to 2.3 km offshore of the disdrometer site at altitudes 0.04 to 0.07 km above the sea surface.

These average $\underline{\bar{I}}$ values were obtained for most RHI scans that were made in the 146° azimuth direction. The values, on most days, were acquired for the period from approximately 1 1/2 hours preceding launch to 1 1/2 hours after launch. The time period between RHI scans varied from one minute (minimum) to as much as 10 to 30 minutes. This depended on the scanning program of the particular day.*

It was assumed that each of the $\underline{\bar{I}}$ values was representative of a one minute time period, which corresponded to the minimum spacing period between the radar data points. The comparison Z_{W_D} values from the disdrometers were likewise computed for one minute periods of sampling.

---

*The RHI scans with the FPS-18 radar were made preferentially in the 146° azimuth direction. However, during the aircraft measurement period following the missile firing, RHI scans were also made in the azimuth directions of the aircraft locations, which sometimes differed from 146°.

Considerable effort was expended in the correlation analyses of the $\underline{\bar{I}}$ and Z_{W_D} data which will not be reported in detail herein. In summary, though, there were two important findings. First, it was discovered that the correlations and correlation coefficients of the data sets for the different days, were appreciably improved by the exclusion of the radar and disdrometer data for precipitation rates smaller than about 0.5 mm/hr. The comparative data for rates smaller than this evidenced large scatter and were deemed non-representative, and were eliminated. Second, it was also apparent, because of the distance separation of the sites of the disdrometer and radar measurements (1.3 km), and because of the occasional-to-frequent presence of spatial inhomogeneities in the storm rainfall at this distance scale, that some selection-rejection criteria were required to minimize the inhomogeneity effects. The criteria adopted were based on the assumption that temporal uniformity of the rainfall, as observed at the disdrometer site, was likely to be associated with spatial uniformity of the rainfall, extending seaward of the disdrometer site out to the place of the radar measurements. With this assumption, particular data points of $\underline{\bar{I}}$ and Z_{W_D} were eliminated from the data sets whenever the rainfall rates at the disdrometer site evidenced large temporal changes that departed from the normal, typical variability that characterized the particular day.

The details of the disdrometer method of calibration can best be illustrated by reference to a particular case example. The day selected for illustration is that of 17 February 1972. The dual sampling period on this day was sufficiently short to allow convenient tabulation of the data. The day was also one, incidentally, when two separate missiles were fired into the storm.

The radar $\underline{\bar{I}}$ values for the calibration period on this day are shown in the second column of Table 5. The corresponding $\underline{Z_{W_D}}$ values (the dB equivalent of Z_{W_D}) are shown in the third column and were obtained from one of the two disdrometers located at the launch site, identified as "Disdrometer B".

Decibel-equivalent values of the system calibration constant, that is, values of $\underline{\kappa}$, were determined for each pair of the $\underline{\bar{I}}$ and $\underline{Z_{W_D}}$ values as follows: Equation (85) was written in dB form as

$$10 \log \kappa = 10 \log \alpha + 10 \log \bar{I} - 10 \log Z_{W_D} , \tag{94}$$

or, in the dB equivalent form defined herein, as

$$\underline{\kappa} = \underline{\alpha} + \underline{\bar{I}} - \underline{Z_{W_D}} . \tag{95}$$

Table 5. Example of Disdrometer Method of Radar Calibration for 17 February 1972, Disdrometer B, Decibel Values, Geometric Averaging

Time	$\underline{Z_{W_D}}$ (dB)	$\underline{\bar{I}}$ (dB)	$\underline{\kappa}$ (dB)	$\underline{\kappa - \bar{\kappa}}$ (dB)	$(\underline{\kappa - \bar{\kappa}})^2$ (dB^2)
1458Z	34.33	73.0	175.32	+ 0.517	0.27
1502	33.84	70.8	173.61	- 1.193	1.42
1503	32.42	69.3	173.53	- 1.273	1.62
1504	31.14	68.5	174.01	- 0.793	0.63
1505	30.36	66.3	172.59	- 2.213	4.90
1506	28.61	68.8	176.84	+ 2.037	4.15
1508	27.57	65.4	174.48	- 0.323	0.10
1509	31.00	67.1	172.75	- 2.053	4.21
1510	28.75	66.8	174.70	- 0.103	0.01
1511	28.23	67.8	176.22	+ 1.417	2.01
1512	29.61	67.0	174.04	- 0.763	0.58
1513	29.97	68.1	174.78	- 0.023	0.00
1514	30.81	67.1	172.94	- 1.863	3.47
1515	29.60	66.7	173.75	- 1.053	1.11
1516	31.67	68.8	173.78	- 1.023	1.05
1517	29.65	65.3	172.30	- 2.503	6.27
1518	26.67	65.3	175.28	+ 0.477	0.23
1519	28.11	67.3	175.84	+ 1.037	1.08
1520	26.92	67.6	177.33	+ 2.527	6.39
1521	28.94	68.3	176.01	+ 1.207	1.46
1522	28.12	69.1	177.63	+ 2.827	7.99
1523	27.77	68.9	177.78	+ 2.977	8.86
1524	28.56	69.1	177.19	+ 2.387	5.70
1525	32.98	68.3	171.97	- 2.833	8.03
1526	31.04	69.8	175.41	+ 0.607	0.37
$\sum_{n=25}$ =	746.67	1700.5	4370.08	+ 0.005	71.91
Mean	29.867	68.02	174.803	+ 0.000	2.876

Standard Deviation = $\sigma_{\underline{\kappa}}$ = ± 1.696

Then, since α for the FPS-18 radar, see Table 3 and Eq. (86), has the value 4.63×10^{13} mm^{6}cm m^{-3} giving $\underline{\alpha}$ = 136.65 dB, Eq. (95) reduces to

$$\underline{\kappa} = 136.65 + \underline{\bar{I}} - \underline{Z_{W_D}} , \tag{96}$$

thereby permitting the $\underline{\kappa}$ computations cited above.

The mean value of $\underline{\kappa}$ was next computed for the n samples of the calibration period. This mean value,

$$\underline{\kappa}_M = \frac{1}{n} \sum_{i=1}^{i=n} \underline{\kappa}_i , \tag{97}$$

was assumed to be the value of the system calibration constant that pertained to the particular disdrometer and calibration period. For the B disdrometer on 17 February 1972, the Table 5 data gave the value

$$\underline{\kappa}_M = 174.80 \text{ dB} . \tag{98}$$

The $\underline{\kappa}_M$ values for the other disdrometers and days of the 1971-72 season were computed in an identical manner. The resultant values, including the above, are listed in Table 6.

Additional information was sought in the 1971-72 season concerning the standard deviation of the $\underline{\kappa}$, $\underline{\bar{I}}$ and $\underline{Z_{W_D}}$ values, also regarding the correlation coefficient (r) and the standard error of estimate (S.E.) of the $\underline{\bar{I}}$ versus $\underline{Z_{W_D}}$ data. The values of these parameters are also shown in Table 6 for the different disdrometers and days of the 1971-72 season.

The only parameters, of these tabulated, that warrant special comment are the standard deviation of $\underline{\kappa}$, that is $\sigma_{\underline{\kappa}}$, and the correlation coefficient.

It should be emphasized that the $\sigma_{\underline{\kappa}}$ values of Table 6 are not indicative of the uncertainties of radar calibration under the disdrometer method. The values merely indicate the uncertainty of $\underline{\kappa}$ that would have resulted if any single pair of the $\underline{\bar{I}}$ and $\underline{Z_{W_D}}$ values had been used, by themselves, for radar calibration purposes. This, of course, was not done since it was the mean value $\underline{\kappa}_M$, for the entire sampling period, that was used to define the calibration constant.

The correlation coefficients shown in Table 6 must be interpreted with extreme care. The correlation coefficient for the $\underline{\bar{I}}$ and $\underline{Z_{W_D}}$ values of the data sets is dependent on the range of the rainfall rates that occurred within the calibration periods. Thus, the correlation coefficients will (and do) have larger

Table 6. Values of the System Calibration Constant, Standard Deviation Values and Correlation Parameters Obtained by the Disdrometer Method for the FPS-18 Radar for the 1971-72 Season

Date and Disdrometer Employed	Number of Paired Measurement Samples	Calibration Constant and Standard Deviation		Correlation Parameters, of the $\underline{\bar{I}}$ versus Z_{W_D} values			
		κ_M (dB)	σ_κ (dB)	$\sigma_{\underline{\bar{I}}}$ (dB)	$\sigma_{Z_{W_D}}$ (dB)	r	*S. E. (dB)
3 February 1972							
Disdrometer A	12	172.8	1.8	2.9	2.6	0.791	1.6
Disdrometer B	12	173.4	1.2	2.9	2.9	0.907	1.2
17 February 1972							
Disdrometer A	25	175.8	2.0	1.7	2.1	0.432	1.9
Disdrometer B	25	174.8	1.7	1.7	2.1	0.590	1.7
17 March 1972							
Disdrometer A	45	178.8	2.3	3.6	3.9	0.807	2.3
Disdrometer B	45	179.9	2.9	3.6	4.7	0.786	2.9
22 March 1972							
Disdrometer A	28	177.2	4.1	3.8	4.6	0.553	3.9
Disdrometer B	28	175.4	4.3	3.8	4.4	0.453	3.9

* S. E. $= \sigma_{Z_{W_D}} \sqrt{1 - r^2}$

values for data sets in which there is a substantial range of the rainrate values (implying an also substantial range of the separate $\underline{\bar{I}}$ and $\underline{Z_{W_D}}$ values) than for data sets in which the rainrates are more or less constant and uniform throughout the calibration periods. To state this another way, the regression line for the $\underline{\bar{I}}$ and $\underline{Z_{W_D}}$ points, as plotted on a scatter diagram, will tend to be "flat" (horizontal) for a uniform rainrate situation, since there is no association trend of the $\underline{\bar{I}}$ and $\underline{Z_{W_D}}$ values, only scatter.* The correlation coefficient in such a case has a small and relatively meaningless value. The scatter of the data is given by the $\sigma_{\underline{\kappa}}$ and S. E. values. Conversely, when the range of the rainrates during the calibration period is substantial, the regression line fitting the data points now has "slope" and the correlation coefficient has a larger value than before (assuming no greater scatter of the data). Some significance can be attached to the value of the correlation coefficient but interpretative care must be exercised, because the value,

*Strictly speaking, depending on which parameter is correlated with the other, the regression line may be horizontal, vertical, or undefined; hence, cease to exist.

in part and degree, is still dependent on the particular range of the rainrate values within the calibration period. The scatter of the data, as before, is given by the $\sigma_{\underline{\kappa}}$ and S. E. values.

The methods used to obtain the system calibration constants for the FPS-18 radar in the 1971-72 season have been explained in the preceding paragraphs. It should be noted that the constants were determined by averaging decibel values to obtain geometric means.

A question may be raised concerning the differences in the means and standard deviations that would have resulted if the actual, or absolute, values of $\overline{I}$ and Z_{W_D} had been averaged to obtain arithmetic means. These differences were explored for the data of the B disdrometer for 17 February 1972, the same data set used previously for illustration. The results are shown in Table 7.

A comparison of Tables 5 and 7 shows that the κ_M value determined by arithmetic averaging has the dB-equivalent value of 175.14, which differs by +0.34 dB from the $\underline{\kappa}$ value of Table 5. It is also seen that the standard deviation value of Table 7 in terms of its dB-equivalent, computed as indicated at the bottom of the table, is ±1.835 dB as opposed to a $\sigma_{\underline{\kappa}}$ value, from Table 5, of ±1.696 dB, a difference of ±0.139 dB.

This indicates the magnitude of the differences between the values of the calibration constants that might be anticipated from arithmetic averaging as opposed to geometric averaging. The differences are relatively small but are nevertheless significant, particularly in view of the SAMS objective of minimizing all possible sources of error and uncertainty. The question of which method of averaging is preferred is really an open question since many radar parameters, such as $\underline{\overline{I}}$, are measured as dB averages; complex problems exist concerning the relationship of these averages, and standard deviations, to the absolute values. For example, see Lhermitte,[30] Lhermitte and Kessler,[31] and Austin and Schaffner.[18]

To summarize the discussions of the present section concerning the disdrometer method of calibration, reference is made to Table 8. The system calibration constants for the FPS-18 radar in the 1971-72 season are listed in this table in terms of their absolute values, rather than the dB values of Table 6.

---

30. Lhermitte, R. M. (1963) Motions of Scatterers and the Variance of the Mean Intensity of Weather Radar Signals, Research Report 63-57, Sperry Rand Research Center, Sudbury, Massachusetts.

31. Lhermitte, R. M., and Kessler, E. (1966) Estimation of the Average Intensity of Precipitation Targets, Proceedings 12th Conference on Radar Meteorology, 17-20 October 1966, Norman, Oklahoma.

Table 7. Example of Disdrometer Method of Radar Calibration for 17 February 1972, Disdrometer B, Absolute Values, Arithmetic Averaging

Time	Z_{W_D} ($mm^6 m^{-3}$)	$\bar{I}$ (cm^{-1})	κ	$\kappa - \bar{\kappa}$	$(\kappa - \bar{\kappa})^2$
1458Z	2710	19.95×10^6	3.41×10^{17}	$+0.143 \times 10^{17}$	0.20×10^{33}
1502	2421	12.02	2.30	-0.967	9.35
1503	1744	8.51	2.26	-1.007	10.14
1504	1299	7.08	2.52	-0.747	5.58
1505	1087	4.27	1.82	-1.447	20.94
1506	726	7.59	4.84	+1.573	24.74
1508	571	3.47	2.81	-0.457	2.09
1509	1258	5.13	1.89	-1.377	18.96
1510	750	4.79	2.95	-0.317	1.00
1511	666	6.03	4.19	+0.923	8.52
1512	914	5.01	2.54	-0.727	5.29
1513	992	6.46	3.01	-0.257	0.66
1514	1206	5.13	1.97	-1.297	16.82
1515	913	4.68	2.37	-0.897	8.05
1516	1470	7.59	2.39	-0.877	7.69
1517	923	3.39	1.70	-1.567	24.55
1518	465	3.39	3.37	+0.103	0.11
1519	647	5.37	3.84	+0.573	3.28
1520	492	5.75	5.41	+2.143	45.92
1521	784	6.76	3.99	+0.723	5.23
1522	649	8.13	5.79	+2.523	63.65
1523	598	7.76	6.00	+2.733	74.69
1524	717	8.13	5.25	+1.983	39.32
1525	1988	6.76	1.57	-1.697	28.80
1526	1270	9.55×10^6	3.48×10^{17}	$+0.213 \times 10^{17}$	0.45×10^{33}
$\sum_{n}^{25}$ =	27260	172.7×10^6	81.67×10^{17}	-0.005×10^{17}	426.0×10^{33}
Mean =	1040.4	6.908×10^6	3.267×10^{17}	-0.000×10^{17}	17.04×10^{33}

Standard Deviation = $\sigma_\kappa = \pm 1.305 \times 10^{17}$

$\bar{\kappa} + \sigma_\kappa = 4.572 \times 10^{17}$ = 176.60 dB

$\bar{\kappa} - \sigma_\kappa = 1.962 \times 10^{17}$ = 172.93 dB

Difference = 3.67 dB $\div 2 \cong \sigma_{dB} \cong \pm 1.835$ dB

Table 8. Absolute Values of the System Calibration Constant κ and Associated Radar Parameters Determined by the Disdrometer Method for the FPS-18 Radar for the 1970-72 Season

Date and Disdrometer Employed	Calibration Constant κ	Corresponding Values of		
		l.	k_s $mW(NM)^4cm^{-2}$	C $(NM)^2cm\ mW$
*15 March 1971	Unknown	0.0533	1.259×10^{-4}	5.14×10^5
*26 March 1971	Unknown	——	——	——
3 February 1972				
Disdrometer A	1.91×10^{17}	0.0296	0.699×10^{-4}	3.85×10^5
Disdrometer B	2.19×10^{17}	0.0340	0.802×10^{-4}	4.42×10^5
17 February 1972				
Disdrometer A	3.80×10^{17}	0.0589	1.390×10^{-4}	7.66×10^5
Disdrometer B	3.02×10^{17}	0.0468	1.104×10^{-4}	6.08×10^5
17 March 1972				
Disdrometer A	7.59×10^{17}	0.1177	2.778×10^{-4}	15.30×10^5
Disdrometer B	9.77×10^{17}	0.1515	3.575×10^{-4}	19.70×10^5
22 March 1972				
Disdrometer A	6.76×10^{17}	0.1048	2.473×10^{-4}	13.62×10^5
Disdrometer B	3.71×10^{17}	0.0575	1.357×10^{-4}	7.48×10^5

* The κ values for the 1970-71 seasons are unknown because a variable coupling attenuator was used with the video integrator. The other values listed, however, are values determined from disdrometer calibration.

Also listed are the values of the system loss factor,

$$l. \quad \frac{\kappa}{C_r c}, \tag{99}$$

see Eqs. (78) and (80), the sphere calibration constant,

$$k_s = lk_r, \tag{100}$$

see Eq. (78), and the calibrated constant C of the radar equation for hydrometeor targets, computed from Eq. (83). The C_r and c values which enter Eq. (99) are given in Table 4.

The κ, L, k_s and C values for the 1970-71 season have also been included at the top of Table 8.

3.5 The Calibration Constants of Application and Estimates of the Possible Uncertainties of Calibration

Since two different methods of radar calibration were employed for the FPS-18 radar in the 1970-71 and 1971-72 seasons, there was the obvious question of which of the calibration-constant values should actually be applied to the radar data for the SAMS missile trajectories. This question will be considered in the present section and we will begin by discussing the relative merits and disadvantages of the two calibration methods. Comments will also be made about the possible uncertainties of calibration.

The sphere method of calibration has the rather obvious advantage of simplicity. The value of the calibration constant is readily obtained from the spherical targets tracked by the radar. The method has one severe disadvantage, however, in that the calibration is almost invariably performed on a day other than that of missile-launch operations. Thus, if the calibration constant obtained from sphere calibration is applied to the radar data along the missile trajectories, it is implicitly assumed that the radar on the launch day was operating the same as it was on the calibration day. This may or may not be true.

There are several reasons why sphere calibrations are performed on days other than the launch days. First of all, the calibration operations require about a one to two hour period of radar time, together with the time of the personnel operating the radar. On a day of launch operations, since the radar is used for launch planning purposes, it is difficult to schedule the time needed for sphere calibration and also tolerate the diversion of personnel to the task. More fundamental though, it has been found that if a sphere calibration is attempted on the day of launch operations—which is usually a stormy day, almost by definition—the balloon or parachute suspending the sphere becomes wet from the precipitation and gives echo return on the radar that destroys the validity of the calibration measurements.

It is difficult to estimate the uncertainties of radar calibration associated with the sphere method. To enable such estimates, comparison calibrations would have to be performed on one single day. Such comparisons, to the author's knowledge, have not been made.

The disdrometer method of radar calibration, in contrast to the sphere method, has the advantage of being conducted on the same day as the launch operations, in the same storm conditions (or very similar) encountered by the missiles. The prime disadvantage, at least in the past, is that the radar and disdrometer measurements required for calibration, also the computations and analyses, are

considerable and time-consuming such that the values of the calibration constants could not be obtained until some weeks or months following the launch day.

There are several other problems and questions concerning the disdrometer method of calibration that are worthy of mention. There is the problem of the distance separation of the places of disdrometer and radar measurement. This separation undoubtedly contributes importantly to the rather large scatter of the comparative data. The calibration constant itself, which is a mean obtained for the entire period of common sampling, should in theory be reasonably valid, providing that the spatial inhomogeneities of rainfall are more-or-less randomly distributed throughout the Wallops storms. But whether this is actually the case and, if not, whether "separation bias" exists within the data are unanswered questions.

There are also questions concerning the proper sensitivity tests, calibration-procedures, and siting and exposure methods that should be used with the disdrometer instruments to insure their accurate, optimum performance. In fact, quantitative information is lacking as to what really constitutes optimum performance under the variety of storm conditions encountered at Wallops Island. Problems likewise exist concerning the large disparity between the sample volumes of the disdrometers (of the order of 0.3 to $3m^3$) and those of the radar (of the order of 10^5 to 10^7 m^3).

In view of these several questions and problems, it is as difficult to assess the possible uncertainties of calibration for the disdrometer method, as for the sphere method. It might be argued that the uncertainties for the disdrometer method might be given by the differences in the calibration constants computed from the data of two adjacent disdrometers on the same calibration day. This might be true, to a first approximation, but it should also be pointed out that the data sets for the two disdrometers are not truly independent, since the same radar signal values were employed commonly in both.

Because of the difficulties with the two calibration methods indicated above, it was decided, at least for the 1971-72 season, that the final calibration values to be applied to the radar measurement data for the missile trajectories would be the simple average of (1) the sphere value, (2) the value for disdrometer A and (3) the value for disdrometer B. This was an arbitrary decision that effectively weighted the values of the disdrometer method twice those of the sphere method.

These final calibration constants, thus computed for the FPS-18 radar for the 1971-72 season, are shown in Table 9. Also shown are the values of the calibration constants that were applied to the FPS-18, the X band and the Spandar radars during the other SAMS seasons.

---

*This will be ameliorated in the future by greater automation of the disdrometer equipment and recording, plus a more extensive use of computers.

Table 9. Final Values of the System Calibration Constant and Associated Parameters Used for the SAMS Radar Measurements of the Different Seasons

Season and Date	Radar	System Calibr. Constant		Corresponding Values of		
		κ	$\underline{\kappa}$ (dB)	L	k_s $mW(NM)^4\ cm^{-2}$	C $(NM)^2 cm\ mW$
1970-71						
15 March 71	FPS-18	*Unknown	*Unknown	0.0533	1.259×10^{-4}	5.14×10^5
26 March 71	FPS-18	*Unknown	*Unknown			
March 71	X Band	Non-Pertinent (Video Integrator Not Used)	Non-Pertinent	~0.0158	$\sim 2.82 \times 10^{-4}$	$\sim 2.31 \times 10^5$
1971-72						
3 Feb 72	FPS-18	2.04×10^{17}	173.1	0.0316	0.746×10^{-4}	4.11×10^5
17 Feb 72	FPS-18	3.55×10^{17}	175.5	0.0551	1.300×10^{-4}	7.16×10^5
17 Mar 72	FPS-18	6.31×10^{17}	178.0	0.0979	2.310×10^{-4}	12.73×10^5
22 Mar 72	FPS-18	3.98×10^{17}	176.0	0.0617	1.459×10^{-4}	8.03×10^5
February-March 1972	Spandar	Non-Pertinent (Video Integrator Not Used)	Non-Pertinent	~0.0220	$\sim 0.661 \times 10^{-4}$	$\sim 2.07 \times 10^6$
1972-73						
2 Feb 73	FPS-18	8.24×10^{17}	179.2	0.0753	1.778×10^{-4}	9.79×10^5
27 Feb 73	FPS-18	7.87×10^{17}	179.0	0.0719	1.699×10^{-4}	9.35×10^5
Feb 73	Spandar					
**Coupling	1 Spandar	10.03×10^{17}	180.0	0.0220	0.661×10^{-4}	1.13×10^6
**Coupling	2 Spandar	17.45×10^{17}	182.4	0.0220	0.661×10^{-4}	1.13×10^6

*Unknown because variable coupling attenuator used.

**See Table 4 footnote (†) for explanation of the two coupling relations used with the Spandar radar in the 1972-73 season.

As a last comment concerning the uncertainties of calibration, it is suggested that these, for the FPS-18 radar in the 1971-72 season, might be indicated to a first, gross approximation by the differences in the two disdrometer values and the sphere value that were used to compute the Table 9 averages. The difference spread of the values on the four days of the 1971-72 season, see Tables 4 and 8, ranged from 0.6 to 4.6 dB (equivalent) and it may be stated that the standard error of estimate varied from ±0.4 dB to ±3.3 dB. The calibration uncertainties are probably of this order.

3.0 Review of the Trajectory Measurement Procedures

The discursive continuity of the report has been interrupted, in the last three sections, by the necessity of describing the radar calibration methods in some detail. Therefore, it would seem beneficial, at this point, to review and consolidate the material presented thus far and to summarize it in the context of its direct application to the SAMS measurement objectives.

In review, then, we might first reiterate that the SAMS missiles were fired in the 146° azimuth direction from launch pad zero at Wallops Island and that the nominal, average elevation angle of the trajectories from the launch pad was about 26° to 31°.

Radar data for the missile trajectories were obtained from the RARF radars which were located 1.8 NM to the NW of the launch pad. The data were obtained primarily in RHI scan in the 146° azimuth direction from the radars, which very nearly corresponded within 1/2° or so, to the 146° direction from the launch pad. Video integration was used and the $\overline{I}$ signal values for each of the RHI scans were photographically recorded, in the 1970-71 and 1971-72 seasons (as gray scale regions of shading contrast), and were recorded on video tape for computer processing, in the 1972-73 season.

Once the missile trajectories had been established from the NASA, postflight tracking-data, the $\overline{I}$ values along the course of the trajectories were determined from the radar RHI photographs, or computer products, that pertained to the launch times of the missiles. These $\overline{I}$ values then became the initial, input data for the computation of the desired end-product values of the reflectivity factors Z_W for water hydrometeors, and Z_I for ice hydrometeors.

To obtain quantitative values of Z_W and Z_I, two things had to be accomplished. Both were essential and the order of mention is unimportant. First, the radar had to be calibrated. This was accomplished by the two methods described previously. The particular calibration constant of computational interest was the system calibration constant, κ, the final values of which are shown in Table 9. Second, independent knowledge was required for the Wallops storms concerning the precise altitude bounds of the melting zone, which separated the region of ice hydrometeors

aloft (the ice crystal and snow particles) from the rain region below. Knowledge of the storm top altitude was also required, since the RARF radars, except under particular conditions (of near vertical incidence) are insufficiently sensitive to detect the storm top boundary. This knowledge was obtained from aircraft measurements and observations, as will be elaborated in a subsequent report.

With the radars calibrated, the water and ice regions defined, and the storm top altitude established, the Z_W values for the water region and particular radar were computed from the $\overline{I}$ data using Eq. (72), that is,

$$Z_W = \frac{1.08\,\lambda^4\,\overline{I}}{\pi^5 K} \times 10^{12} \quad \frac{mm^6}{m^3} \quad , \tag{72}$$

and the Z_I values for the ice region and particular radar were computed from Eq. (73), that is,

$$Z_I = \frac{4.78\,\lambda^4\,\overline{I}}{\pi^5 K} \times 10^{12} \quad \frac{mm^6}{m^3} \quad . \tag{73}$$

For example, for the FPS-18 radar on 17 February 1972—a radar and a day previously used in illustration—Eqs. (72) and (73) immediately reduce to (see Tables 3 and 9)

$$Z_W = 1.303 \times 10^{-4}\,\overline{I} \quad \frac{mm^6}{m^3} \tag{101}$$

and

$$Z_I = 5.767 \times 10^{-4}\,\overline{I} \quad \frac{mm^6}{m^3} \quad . \tag{102}$$

Within the melting zone, as noted in Section 3.1, the values of the reflectivity factor are indeterminate. The values of both Z_W and Z_I were computed for the segments of the missile trajectories that passed through this zone. The Z_W values are indicative of the small-value limits of the reflectivity factor across the zone and the Z_I values provide some indication of the reflectivity factor values which are equaled or exceeded within the zone. The explanation of this last statement is that snowflakes, which fall into the melting zone and acquire a thin water coating without appreciable size change, can produce radar returns greatly exceeding those of dry snowflakes of equal size.

Another special-case situation was also mentioned previously. This was the case of supercooled clouds, which exist in water form at temperatures well below freezing. It may be stated that no analytical problems existed with the radar data regarding such clouds, or regarding water clouds in general, either warm or supercooled, since the RARF radars are presently incapable of detecting water droplets in the cloud-size range. SAMS information about water clouds had to be acquired necessarily from aircraft measurements.

4. DESCRIPTION AND PROGRESS REPORT OF THE SAMS RADAR MEASUREMENTS OF THE DIFFERENT SEASONS

The general nature of the SAMS operations and radar measurements of the different seasons to date will be described in this section and comments will be made about plans for the 1973-74 season.

These descriptions will serve two purposes. They will indicate the particular types of radar measurements that were made in the different years and they will provide a progress report to show how the specificity and accuracy of measurement have been improved, season by season, to better satisfy the SAMS overall objectives.

It should be noted that missiles of the Terrier-Recruit type were used throughout all of the previous seasons. These missiles and flights have been reported by Cole and Robinett, and Cole, Church and Marshall.

4.1 The 1970-71 Season

The SAMS program at Wallops Island was in its infancy in the 1970-71 season. AFCRL had no prior, extensive experience with radar measurements of the type required for the program. The Wallops Island radars and video integrator were untested and the calibration, measurement and analytical procedures had to be developed as the season progressed.

Both the FPS-18 and X Band radars were used to obtain data along the missile trajectories. The FPS-18 data consisted of RHI and A scope photographs of the RHI sweeps made in the launch direction. The X band data consisted of graphical records of received power versus range that were acquired for a fixed elevation angle corresponding approximately to the mid-trajectory angle of the missile, as measured from the origin at the radar site. The records were nicknamed the "Bloody Reds", since the traces were highly variable and copious amounts of red ink were expended in the recording process.

The X band data for this season were analyzed by the Applied Physics Laboratory of Johns Hopkins University. The results have been reported by Meyer.[32]

The calibration constants for the FPS-18 radar were obtained by both the sphere and disdrometer methods. Those for the X band radar were obtained by the sphere method. The values of the constants, as best known to the author, are shown in Tables 4 and 8.

Video integration was used just with the FPS-18 radar. The integrator provided a running-mean average of the signal ($\underline{\bar{I}}$) values which was "weighted" in an exponential fashion. The averaging was performed for single range cells. The integrator also had an "attenuator" which, in effect, permitted the values of the coupling constant, see Eq. (81), to be changed at will.

The averaging factor γ for this integrator and season, see Eq. (44), was assumed to have the value 0.398 (or -4.0 dB), a value obtained from the work of Austin and Schaffner.[18]

It is the author's understanding that the video integrator of the 1970-71 season was deficient in two primary respects. First, it failed to provide integration for a sufficient number of independent samples, which, combined with the exponential weighting of the averages, resulted in the $\underline{\bar{I}}$ signal output being somewhat "jittery". This tended to degrade the quality of the gray-scale photographs showing the signal levels within the Wallops storms. The integrator also failed to accomplish the "range normalization function", see Section 2.7.2, with complete fidelity, such that range corrections had to be applied in certain instances.

The $\underline{\bar{I}}$ data for each missile were obtained from the RHI photographs taken at the launch times. The course of the given missile trajectory across the photograph was known and the $\underline{\bar{I}}$ signal values could be accurately determined for each point where the trajectory intersected with a boundary of the gray-scale regions shown on the photographs. The $\underline{\bar{I}}$ values between points, that is the values along the trajectories within the photographic gray-regions themselves, could only be inferred, or estimated, by interpolation.

The trajectory values of Z_W and Z_I were determined from the $\underline{\bar{I}}$ data following the procedures outlined in Section 3.6. Information about the altitudes of the melting zone and storm top level was acquired by the AFCRL, C-130, cloud-physics aircraft.

---

32. Meyer, J.H. (1971) Precipitation Rates and Liquid Water Content Measured by the JAFNA X-band Radar for the Rain Erosion Test, 26 March 1971, Informal Report, Applied Physics Laboratory, Johns Hopkins University, BPD714-19, 24 June 1971.

4.2 The 1971-72 Season

The FPS-18 radar was used as the pri -y radar, as in the previous season, and RHI and A scope data were obtained for e missile trajectories in a manner similar to the first season, but with certain improvements. The Spandar radar, rather than the X band, was used to secure the "Bloody Red" records of P_r versus range, for the trajectories.

The FPS-18 radar was calibrated by both the sphere and disdrometer methods, as described in Sections 3.3, 3.4 and 3.5 herein. The Spandar radar was calibrated by the sphere method only. The calibration constants of final application are listed in Table 9.

A video integrator of new design was utilized in the 1971-72 season. This provided logarithmic, running-mean averaging of the instantaneous signal values and its versatility, in terms of the selectable choices of integration period, number of range cells included, number of signal level outputs, and output format, was a considerable improvement over the integrator used in the previous season. The averaging factor γ for this integrator and season, was assumed to be 0.537 (or -2.7 dB), a value again obtained from the work of Austin and Schaffner.[18]

The quality of the gray-scale, RHI photographs acquired from the FPS-18 radar was enhanced by the employment of the new integrator. A larger number of shading differentiations of signal level was provided on the photographs, than formerly, and the contrast definition of the gray-shade regions provided better and more accurate picture resolution. The photography was accomplished using polaroid film, which was developed for viewing some 30 seconds following the termination of the RHI sweep. Thus, the photographs could be used for real-time planning purposes and were also available for later analyses.

The $\underline{\overline{I}}$ values for the missile trajectories were obtained from the launchtime, RHI photographs in the same manner as in the previous season. The values were determined for each point along the trajectory which intersected the boundaries of the gray-scale regions shown on the photographs. The trajectory values between points were inferred by interpolation.

The Z_W and Z_I values for the trajectories were established from the $\underline{\overline{I}}$ data using Eqs. (72) and (73), which were programmed for computer solution and plotting. Information about the altitudes of the boundaries of the melting zone and storm top was secured by the AFCRL, C-130 aircraft and/or by an Aztec aircraft flown contractually by Meteorology Research, Inc. (MRI).

The trajectory data acquired from the Spandar radar were never fully-analyzed for the 1971-72 season. The analyses, begun by APL, were time-consuming and there was an apparent general realization among the AFCRL and APL personnel, which was never verbalized, that the Spandar data were not likely to provide much of additional value to the information already obtained

from the FPS-18 photographs. The analyses were discontinued, essentially by default of interest.

1.3 The 1972-73 Season

The FPS-18 radar was also used as the primary radar in the 1972-73 season. The "Bloody Red" recordings were discontinued and the Spandar radar was diverted to operation in the PPI mode, to secure PPI and sector-scan photographs of polaroid type.

Video integrators were used with both of these radars which were of the same type as the previous season. The integrator for the FPS-18 radar provided contoured RHI information, as before, and the Spandar radar provided contoured PPI and sector-scan data.

A major change was effected in the 1972-73 season concerning the methods of recording the primary data from the FPS-18 radar. Although photographic recording was still used for real-time planning purposes, the integrator output for the RHI sweeps was also recorded on video tape. These tapes were processed by computer using programs designed by the Weather Radar Branch of AFCRL. Various kinds of information, in RHI format, were provided and greatly simplified the analytic procedures of determining the $\underline{\bar{I}}$ signal values for the missile trajectories. The accuracy and resolution of the analyses were also enhanced, relative to the photographic procedures used previously.

The method of determining the $\underline{\bar{I}}$ values along the missile trajectories is illustrated in Figure 2. A rectangular gridwork is shown which encompasses a part of the range-altitude section of one of the RHI sweeps of the FPS-18 antenna. (The date and time are unimportant, since the illustration is schematic only.) It is seen that a typed letter, number, or other symbol appears within each of the boxes. These provide coded, computer-output information about the average $\underline{\bar{I}}$ signal values that existed within the range-altitude boundaries of the boxes. The box dimensions are 600 ft in horizontal extent by 180 ft in vertical extent, dimensions that are dictated in part by the letter and line spacing of the teletype printer of the computer.

The beginning, lower portion of a simulated missile trajectory has been drawn on the diagram which cuts through and between the various boxes along its course. It is seen that, with knowledge of the symbol code, the $\underline{\bar{I}}$ values along the trajectory can be readily established as a function of distance. Some interpolation is required but this poses no particular problem.

This procedure was used to secure the trajectory data for the 1972-73 season. It will also be used in the 1973-74 season.

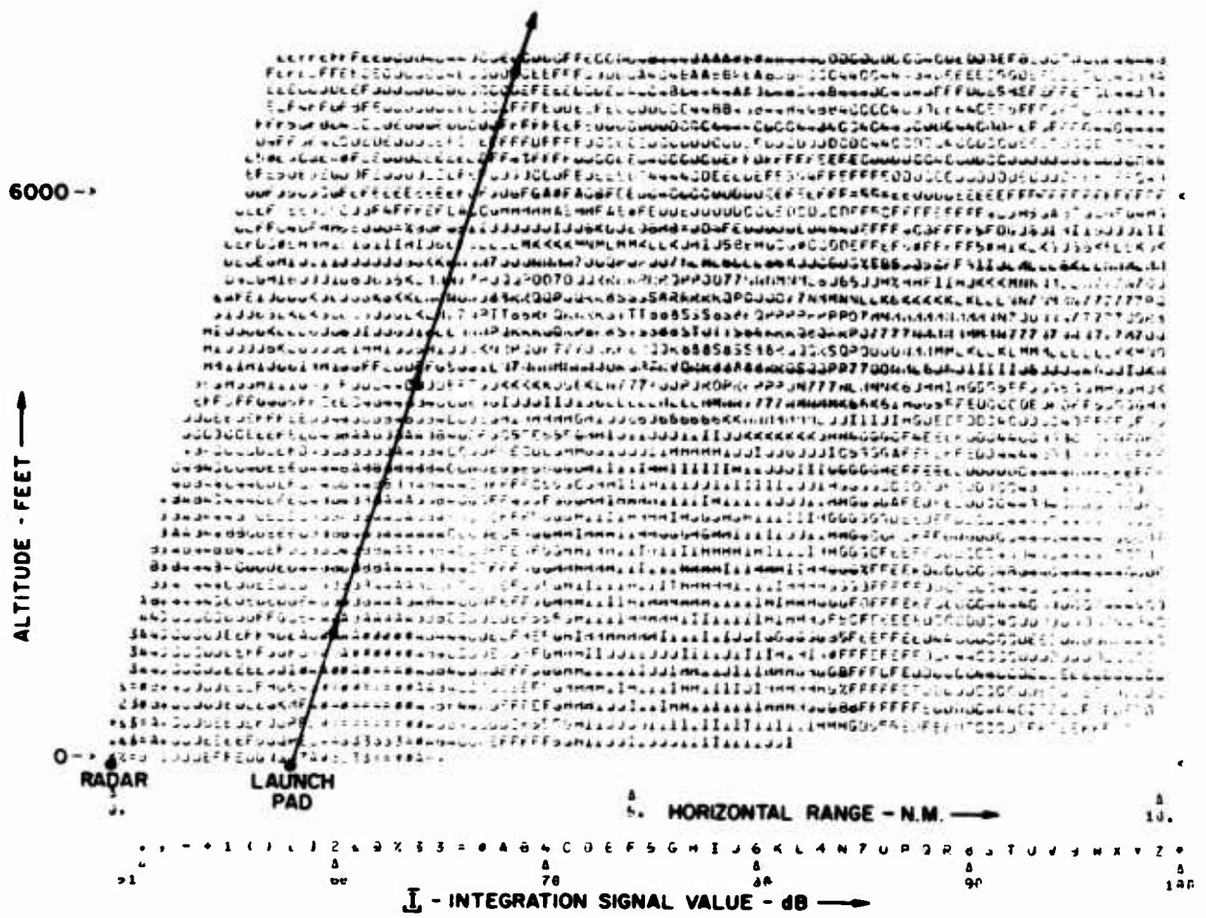

Figure 2. Portion of Range-Altitude Cross Section Showing Symbol-Coded Values of Radar-Integration Signal I With Superimposed Missile Trajectory. The symbol key is indicated along the lower abscissa scale

Radar calibration in the 1972-73 season was accomplished only by the sphere method. Data were acquired to permit calibration by the disdrometer method but, as mentioned earlier, preliminary analyses revealed discrepancies between the sphere and disdrometer values for the day of 27 February 1973, which have not yet been resolved.

Determination of the Z_W and Z_I values from the $\overline{I}$ trajectory data was accomplished as described in Section 3.6. The altitudes of the melting zone boundaries and storm top were obtained from the AFCRL, C-130 aircraft and/or from a Navajo aircraft flown contractually by MRI.

4.1 Plans for the 1973-74 Season

New, three-stage, TATER (Talos-Terrier-Recruit) missiles will be flown in the 1973-74 season. The trajectories of these missiles will be lower (more horizontal) than those of the previous two-stage missiles and the total path distance through the Wallops storms will be extended appreciably. This imposes the requirement that the radar measurements for the new trajectories will have to be extended to greater radar ranges, than for the old trajectories. It also imposes a radar detectability problem, since the detection capabilities of the FPS-18 radar for the small-snow particles and ice crystals in the uppermost portions of the storms is marginal, at best, even with the prior trajectories.

Computations indicate that a 5 dB increase in the sensitivity of the FPS-18 radar is needed to obtain measurement data for the new trajectories that are equivalent, in terms of minimum detectable values of the reflectivity factor, to the trajectory data obtained previously. A 10 dB increase is needed to ensure the consistent detection of the small-snow particles and ice crystals at the storm top extremities of the new trajectories.

To meet these needs, the Weather Radar Branch of AFCRL plans to increase the sensitivity of the FPS-18 radar by about 12 dB. Three dB will be obtained by doubling the pulse length of the radar. The other 9 dB improvement will be achieved by compensating for the non-logarithmic performance of the radar receiver at power levels below about -90 dBm. Such compensation, made electronically or by computer processing of data, will permit the integrated received power $\overline{P}_r$, see Eqs. (42) and (50), to be accurately determined down to levels of approximately -101 dBm rather than -92.3 dBm, as at present, in the 1972-73 season.

The Spandar radar in the 1973-74 season will be used for three purposes. It will be operated to secure contoured PPI photographs of the Wallops storms at about five minute intervals during periods before and after the launch time of the missile. Between the times of these photographs, the antenna will be pointed over the disdrometer sites to obtain calibration data. At the launch time of the missile,

the radar will be operated in the RHI mode and five RHI photographs, plus recorded video data, will be obtained for a 5^{o} azimuth sector symmetrical about the azimuth angle of the missile trajectory.

The Spandar radar, for some or all of these measurements, will be operated in a frequency-diversity mode in which the wavelength of transmission and reception is changed from pulse to pulse of the radar, sequentially increased then decreased, by an amount slightly exceeding the bandwidth of the radar receiver. This mode of operation is advantageous in that there is then no need, in the video integration, to "wait for" the hydrometeors to redistribute themselves naturally (through turbulent and differential fall-velocity mechanisms) to secure independent samples. Rather, independent, non-autocorrelated samples of the hydrometeors are obtained for each pulse of the radar. Hence, with frequency diversity the Atlas equation, Eq. (41) specifying the "reshuffling time" of the hydrometeors no longer pertains, and the number of independent samples per integration period for the case of a stationary antenna is given by

$$n_i = \Delta t_I \, prf \ , \tag{103}$$

instead of by Eq. (A7) of Appendix A, as formerly provided. Likewise, the other equations of Appendix A, which contain n_i as an independent variable, namely Eqs. (A13), (A14), (A16), (A18), (A19), (A24) and (A26), are all modified accordingly.

The representativeness of the Spandar data acquired with frequency diversity will be considerably improved, as compared to previous data. The number of independent samples per integration period will be increased by the approximate factor τx prf. Consequently, some 17 times more independent samples will be included in the integration than formerly (for a prf of 960 pps, which is commonly used).

The $\underline{I}$ data from the FPS-18 radar for the missile trajectories will be analyzed in a manner similar to that described for the 1972-73 season. The trajectory data from the Spandar radar will be analyzed contractually by API.

The altitudes of the melting zone boundaries and storm top will be determined by the AFCRL, C-130A aircraft and/or by Navajo or Citation aircraft operated by MRI. A second AFCRL, C-130E aircraft should be available for the SAMS observation-measurement program about March 1974.

References

1. Kerr, D.E. (1951) Propagation of Short Radio Waves, McGraw-Hill, New York.

2. Austin, P.M., and Williams, E.L. (1951) Comparison of Radar Signal Intensity with Precipitation Rate, Technical Report No. 14, Weather Radar Research Project, M.I.T., Cambridge, Massachusetts.

3. Probert-Jones, J.R. (1962) The radar equation in meteorology, Quart. J. Roy. Meteorol. Soc. 88:485-95.

4. Silver, S. (1951) Microwave Antenna Theory and Design, McGraw-Hill, New York.

5. Marshall, J.S., Langille, R.C., and Palmer, W.M.K. (1947) Measurement of rainfall by radar, J. Meteorol. 4(No. 6):186-192.

6. Atlas, D. (1964) Advances in radar meteorology, from Advances in Geophysics, 10:317-478, Academic Press, New York.

7. Bartnoff, S., Atlas, D., and Paulsen, W.H. (1952) Experimental Statistics in Cloud and Rain Echoes, Proceedings 3rd Weather Radar Conference, McGill University, 15-17 Sept 1952, G1 to G7.

8. Fleisher, A. (1953, 1954) Information Contained in Weather Noise, M.I.T. Department of Meteorology, Weather Radar Research Technical Report No. 22 A,B.

9. Stone, M.L., and Fleisher, A. (1956) The Measurement of Weather Noise, M.I.T. Dept. of Meteorol, Weather Radar Res, Report No. 26.

10. Williams, E.L. (1949) The Pulse Integrator, Part A: Description of the Instrument and its Circuitry, Technical Report No. 8A, Weather Radar Research Project, M.I.T., Cambridge, Massachusetts.

11. Austin, P.M., and Richardson, C. (1952) A Method of Measuring Rainfall Over an Area by Radar, Proceedings 3rd Weather Radar Conference, McGill University, 15-17 Sept 1952, D-13 to D-20.

12. Farnsworth, G.W., and Mueller, E.A. (1953) Radar Rainfall Area Integrator, Proceedings Conference on Radio Meteorology, Art. IX-3, University of Texas, Austin.

13. Marshall, J.S., and Hitchfield, W. (1953) The interpretation of the fluctuating echo for randomly distributed scatterers, Part I, Can. J. Phys. 31:962-994.

14. Lindgren, B.W., and McElrath, G.W. (1963) Introduction to Probability and Statistics, The Macmillan Company, New York.

15. Schaffner, M. (1966) A Digital Sweep Integrator for Weather Radar, Proceedings 12th Conference on Radar Meteorology, 17-20 October 1966, Norman, Oklahoma.

16. Groginsky, H.L. (1966) Digital Processing of the Spectra of Pulse Doppler Radar Precipitation Echoes, 12th Conference on Radar Meteorology, 17-20 October 1966, Norman, Oklahoma.

17. Kodaira, N. (1960) The Characteristics of the Averaged Echo Intensity Received by the Logarithmic I.F. Amplifier, Proceedings 8th Weather Radar Conference, Am. Meteorol. Soc., Boston, Massachusetts, pp. 255-261.

18. Austin, P.M., and Schaffner, M.R. (1970) Computations and Experiments Relevant to Digital Processing of Weather Radar Echoes, Proceedings 14th Weather Radar Conference, 17-20 November 1970, Tucson, Arizona.

19. Glover, K.M. (1972) A Precision Digital Video Integrator, Proceedings 15th Weather Radar Conference, Am. Meteorol. Soc., Boston, Massachusetts, p. 193-198.

20. Ryde, J.W. (1946) Echo Intensities and Attenuation Due to Clouds, Rain, Hail, Sand and Dust Storms at Centimetre Wavelengths, GEC Report No. 7831, October 1941, also GEC Report No. 8516, Aug. 3, 1944, by J.W. Ryde and D. Ryde, corrections.

21. Gunn, K.L.S., and East, T.D.R. (1954) The microwave properties of precipitation particles, Quart. J. Roy. Met. Soc. 80:522(427-8).

22. Debye, P. (1929) Polar Molecules, Chemical Catalog Co., New York, Section 8.1 and Chapter V.

23. Mason, B.J. (1971) The Physics of Clouds, Second Edition, Clarendon Press, Oxford, England.

24. Joss, J., and Waldvogel, A. (1970a) A Disdrometer for Raindrops, Instruction Manual, Marc Weibel Dipl. Ing., ETH, Kapellenstrasse 20, 4000 Basel, Switzerland.

25. Joss, J., and Waldvogel, A. (1970b) Disdrometer RD-69, Instruction Manual, Marc Weibel Dipl. Ing., ETH, Kapellenstrasse 20, 4000 Basel, Switzerland.

26. Joss, J., and Waldvogel, A. (1970c) Analyses AD-69, Instruction Manual, Marc Weibel Dipl. Ing., ETH, Kapellenstrasse 20, 4000 Basel, Switzerland.

27. Spilhaus, A.F. (1948) Raindrop size, shape, and falling speed, J. Meteorol. 5:108-110.

28. Gunn, R., and Kinzer, G.D. (1949) The terminal velocity of fall for water droplets in stagnant air, J. Meteorol, 6:243. (565, 594, 596-7).

29. Liu, J.Y., and Orville, H.D. (1968) Numerical Modelling of Precipitation Effects on Cumulus Cloud, Report 68-9 Inst. Atmos. Sci., South Dakota School of Mines and Technology, Rapid City, South Dakota.

30. Lhermitte, R.M. (1963) Motions of Scatterers and the Variance of the Mean Intensity of Weather Radar Signals, Research Report 63-57, Sperry Rand Research Center, Sudbury, Massachusetts.

31. Lhermitte, R. M., and Kessler, E. (1966) Estimation of the Average Intensity of Precipitation Targets, Proceedings 12th Conference on Radar Meteorology, 17-20 October 1966, Norman, Oklahoma.

32. Meyer, J. H. (1971) Precipitation Rates and Liquid Water Content Measured by the JAFNA X-band Radar for the Rain Erosion Test, 26 March 1971, Informal Report, Applied Physics Laboratory, Johns Hopkins University, BPD714-19, 24 June 1971.

Appendix A

Other Considerations Involving Pulse and Video Integration

1. INTRODUCTION

When radar data are acquired by use of a pulse or video integrator, it is essential, as noted in Section 2.4, to have quantitative information concerning (1) the temporal and spatial resolution of the measurements, (2) the independence and representativeness of the hydrometeor samples included in the integration, and (3) the variance of the measurement values about the probable "true values".

The above topics are discussed herein. The discussion provides background information regarding radar measurements obtained with pulse or video integrators which is directly pertinent to the subject of measurement uncertainties (a subject considered in Appendix B).

2. THE TEMPORAL-SPATIAL RESOLUTION OF RADAR MEASUREMENTS MADE WITH PULSE OR VIDEO INTEGRATION

The signal stability that is achieved by video integration is a desirable and essential feature of weather-radar measurements. It permits the average signal levels within storms to be determined and displayed in contoured form without the presence of a lot of fine-scale, echo detail, which otherwise would make contouring difficult, if not impossible.

It must be emphasized, however, that this signal stability is achieved at the cost of a degradation of both the temporal and spatial resolution of the radar measurements (relative to their non-integrated counterparts).

The fundamental time resolution of a radar with hydrometeor targets is the time duration of the backscattered pulse, which, reference Section 2.4.1, is

$$\Delta t = \frac{h}{2}, \tag{A1}$$

where h' is the pulse duration, specified in time units.

The fundamental spatial resolution of the radar is that of the pulse volume, which, from Eq. (28) rewritten, is

$$V = \frac{\pi (r\theta)^2 h}{8}, \tag{A2}$$

where h is the pulse length in length units. The relation between h and h' is given in Eq. (24).

With pulse integration, or video integration, the time resolution of the measurements becomes

$$\Delta t_I = \frac{n_p}{prf}, \tag{A3}$$

where n_p is the number of radar pulses included in the integration and prf is the pulse repetition frequency of the radar.

Ignoring derivation details, the spatial resolution of measurements made with a pulse or video integrator is

$$V_I = n_c V \left[1 + \frac{4}{\pi\theta} \tan (\beta \Delta t_1) \right], \tag{A4}$$

where n_c is the number of range cells integrated and β is the antenna scan rate (for example β, for RHI scan, is the rate of change of the elevation angle, whereas, β, for PPI scan, is the rate of change of the azimuth angle). This equation applies only to a parabolic antenna.

Resolution values, both fundamental and with integration, are shown in Table A1 and were computed from Eqs. (A2) through (A4) for a radar having $h' = 0.5\ \mu$sec, $\theta = 0.48^{\circ}$, prf 960 pulses/sec and $\beta = 1^{\circ}$/sec. (This corresponds to the FPS-18 radar of the SAMS program in RHI scan, see Section 4 and Table 3.) It was also assumed that the integration was performed for 256 pulses and over 8 range cells. (These are typical, normal values for the AFCRL integrator.) The resolution values of the table are shown for five different radar ranges.

Table A1. Comparison Example of the Temporal and Spatial Resolution of the Wallops Island, FPS-18 Radar in RHI Scan, With and Without Video Integration [ref. Table 3 and Eqs. (A2) through (A4)]

Slant Range r		Fundamental Radar Resolution		Resolution With Video Integration (for n_p = 256, n_c = 8 and β = 1° sec)	
(NM)	(m)	Time Duration of Back-Scattered Return Pulse Δt (sec)	Pulse Volume V (m^3)	Integration Time Δt_I (sec)	Integration Volume V_I (m^3)
5	9,260	0.25×10^{-6}	0.35×10^{6}	0.267	4.78×10^{6}
10	18,530	0.25×10^{-6}	1.42×10^{6}	0.267	19.41×10^{6}
15	27,800	0.25×10^{-6}	3.19×10^{6}	0.267	43.59×10^{6}
20	37,060	0.25×10^{-6}	5.68×10^{6}	0.267	77.62×10^{6}
25	46,330	0.25×10^{-6}	8.87×10^{6}	0.267	121.20×10^{6}

It is seen that the temporal resolution of the radar measurements is degraded from 0.25 μsec to 0.267 sec, with integration, a factor of approximately 10^6, and that the spatial resolution at all ranges is degraded by about a factor of 14. The specific amounts of the degradation for any radar and integrator, are given by the ratios $\Delta t / \Delta t_I$ and V / V_I, which from Eqs. (A1) through (A4), are

$$\frac{\Delta t}{\Delta t_I} \quad \frac{h' prf}{2n_p} \tag{A5}$$

and

$$\frac{V}{V_I} \quad \frac{1}{n_c}\left[1 + \frac{4}{\pi\theta}\tan(\beta\Delta t_1)\right]^{-1} . \tag{A6}$$

3. INDEPENDENCE AND REPRESENTATIVENESS OF THE HYDROMETEOR SAMPLES OBTAINED BY PULSE OR VIDEO INTEGRATION*

Assuming for the moment that the antenna is stationary and that there is no wind, for any single range cell of the integrator, the "reshuffling time" of the hydrometeors required to give non-autocorrelated, independent data is the time τ

*These subjects are treated in brief, summary fashion herein. For a detailed discussion, reference Sirmans and Doviak.[1]

1. Sirmans, D., and Doviak, R.J. (1973) Meteorological Radar Signal Intensity Estimation, NOAA T. M. ERL NSSL-64, National Severe Storms Lab., Norman, Oklahoma, September 1973

specified by Eq. (41) which is based on the work of Atlas.[2] Therefore, if the integration period is Δt_I, it follows that

$$n_i = \frac{\Delta t_I}{\tau}, \tag{A7}$$

where n_i is the number of independent samples. Hence, from Eq. (41) and Eq. (43),

$$n_i = \frac{585\, n_p}{prf\, \lambda}, \tag{A8}$$

for λ specified in centimeters. It also follows that the number of radar pulses per independent sample is

$$r_i = \frac{n_p}{n_i} = 0.00171\ prf\ \lambda, \tag{A9}$$

from Eq. (A8).

For the radar example cited earlier, which reflected the SAMS conditions of operation with the FPS-18 radar and AFCRL integrator, the number of independent samples with a stationary antenna and no wind is 14.6, from Eq. (A8), for $n_p = 256$, prf = 960 and $\lambda = 10.7$ cm, and the number of pulses per independent sample is 17.6 from Eq. (A9). This indicates the magnitude of the n_i and r_i values for a single range cell.

We may now consider the situation when the antenna is moving.

If the radar antenna moves with a scan rate β, new, independent samples are acquired at any given range distance whenever the angular travel of the antenna, relative to some starting reference, has become equal to the beamwidth. Hence, with the antenna in uniform motion, new, independent samples are acquired at the rate β/θ* and, during the integration period Δt_I, the number of new samples acquired is

$$\Delta n_{i_m} = \frac{\beta \Delta t_I}{\theta}. \tag{A10}$$

---

* The acquisition rate is β/θ to a close approximation, ignoring second order terms of minor contribution.

2. Atlas, D. (1964) Advances in radar meteorology, from Advances in Geophysics, 10:317-478, Academic Press, New York.

The wind movement through any single range cell will also introduce new, independent samples of hydrometeors. The rate of introduction is given approximately by

$$R_T \simeq \frac{4|\vec{V}_H|}{h + 2r\theta}, \tag{A11}$$

where $|\vec{V}_H|$ is the magnitude, or "speed", of the horizontal wind vector. This equation assumes that the wind transports the hydrometeors across the "average" dimension of the radar range cell, which has the range-length $h/2$ and the beam-cross-section-diameter $r\theta$. (Such assumption is justified because the number of independent samples introduced by wind translation is relatively small and of second order contribution.)

During the integration period Δt_I, the number of new, independent samples acquired by wind transport is

$$\Delta n_{i_w} \simeq R_T \Delta t_I . \tag{A12}$$

The total number of independent samples per single range cell, in the case of both antenna motion and wind translation, is given by

$$n_{i_{mw}} = n_i + \Delta n_{i_m} + \Delta n_{i_w} , \tag{A13}$$

which, from Eqs. (A3), (A8) and (A10) through (A12), becomes

$$n_{i_{mw}} \Delta t_I \left[\frac{585}{\lambda} + \frac{\beta}{\theta} + \frac{4|\vec{V}_H|}{h + 2r\theta}\right]. \tag{A14}$$

The number of radar pulses that pass through each of the independent samples, for the moving antenna, wind translation case, is

$$n_m = \frac{n_p}{n_{i_{mw}}} , \tag{A15}$$

or, from Eqs. (A3) and (A14),

$$n_m = \frac{prf}{\frac{585}{\lambda} + \frac{\beta}{\theta} + \frac{4|\vec{V}_H|}{h + 2r\theta}} . \tag{A16}$$

Limits are imposed on the number of pulses per independent sample per integration period that can be obtained by pulse or video integration. If we recognize that a certain minimum number of pulses per sample per integration period is required for data representativeness this, in turn, imposes limits on the antenna scan rate that can be used under different conditions of wind translation. These limitations may be demonstrated as follows:

If it is stipulated that

$$\nu_m \geq \nu_{min}, \tag{A17}$$

where ν_{min} is the minimum number of radar pulses per sample per integration period needed for representativeness, then, from Eqs. (A16) and (A17), the representativeness requirement for any given radar and wind condition is,

$$\nu_{min} \leq \frac{prf}{\frac{585}{\lambda} + \frac{\beta}{\theta} + \frac{4|\vec{V}_H|}{h+2r\theta}}, \tag{A18}$$

and the associated limitation on the antenna scan rate is, from Eq. (A18), solved for β,

$$\beta \leq \theta \left[\frac{prf}{\nu_{min}} - \frac{585}{\lambda} - \frac{4|\vec{V}_H|}{h+2r\theta} \right]. \tag{A19}$$

The maximum number of radar pulses per independent sample per integration period that can be obtained with a given radar is the number for the case of a stationary antenna with no wind. This maximum, from Eq. (A16), is specified by

$$\nu_{max} = \frac{\lambda prf}{585}, \tag{A20}$$

which shows that a change in the maximum can only be effected by changing either the prf or the wavelength of the radar.* It is also seen, by reference to Eq. (A16), that any antenna motion or wind translation of the hydrometeors will cause ν_m to have values smaller than this maximum.

---

*One method of increasing this maximum value is by "frequency diversity", in which the wavelength is changed by an amount exceeding the receiver bandwidth from pulse to pulse of the radar. Reference Section 4 for additional comments.

The significance of the above equations may be illustrated by citing a particular example. Assume, first, that at least 15 radar pulses per independent sample are required for representativeness, such that $n_{i_{min}} = 15$. Assume, next, that the radar of concern has $\lambda = 10.7$ cm, $\theta = 0.48^{o}$, h = 150 m and prf = 960 pulses/sec (corresponding to the FPS-18 radar of the SAMS program).

For this radar, Eq. (A20) shows that the maximum obtainable number of pulses per independent sample is 17.6, which exceeds the number $n_{i_{min}} = 15$ that we assumed were required for representativeness.

Suppose, now, that the antenna is moving but there is no wind. Then, Eq. (A19), for $n_{i_{min}} = 15$, becomes

$$\beta = 4.48^{o}/\text{sec} \tag{A21}$$

which stipulates that the antenna cannot be scanned more rapidly than this, if representative data are to be acquired.

Assume, finally, that the speed of the horizontal wind at the altitude of a particular range cell, located r = 5 km from the radar site, is 30 m/sec. Equation (A19), for this wind situation, specifies that

$$\beta < 4.23^{o}/\text{sec}\ , \tag{A22}$$

to obtain representative data. The change in β from Eq. (A21) is very slight, emphasizing the fact that the wind translation term in the previous equations is of second order, at least for the FPS-18 radar of our example.

The discussion thus far has been limited to the case of a single range cell.

If multiple range cells are included in the integration, then, since each cell has been defined and set equal to the range extent of the pulse volume, the data for any individual cell are independent of the data for adjacent cells.

Therefore, the total number of independent samples included in the pulse or video integration is the multiple of the number of cells, n_c, times the number of independent samples per single cell, or

$$n_{i_T} = n_c n_{i_{mw}}\ , \tag{A23}$$

which, from Eqs. (A3) and (A14), becomes

$$n_{i_T} = \frac{n_c n_p}{prf}\left[\frac{585}{\lambda} + \frac{\beta}{\theta} + \frac{4\left|\vec{V}_H\right|}{h \div 2r\theta}\right] \tag{A24}$$

for λ in centimeters.*

The other equations, Eqs. (A15) through (A20), regarding the number of radar pulses per independent sample per integration period and the restrictions on the antenna scan rate, remain unchanged for the case of integration over multiple range cells.

I. VARIANCE EQUATIONS

The importance of the equations just derived to the estimation of the variance, and uncertainties, or radar measurements made with pulse or video integration will now be discussed.

Marshall and Hitchfield[3] have shown that the distribution of the averages of n independent samples of a parameter, such as $\overline{P}_r$, which is the parameter measured by the pulse or video integrator, reference Section 3.2, will vary with n as illustrated in Figure A1. The dashed and dotted lines show the envelopes of the first and second standard deviation of the $\overline{P}_r$ averages about the $n = \infty$ value of $\overline{P}_r$, which is shown by the solid horizontal line. It is seen that the variation of the $\overline{P}_r$ averages decreases with n, as would be expected.

If the standard deviation of any large, unspecified number of single independent radar samples of hydrometeors is $\sigma_{\overline{P}_{r_1}}$, and if n such independent samples are group-averaged by a pulse or video integrator, the standard deviation of the integrated values of $\overline{P}_r$ will vary with n approximately as

$$\sigma_{\overline{P}_r} \cong \frac{\omega \sigma_{\overline{P}_{r_1}}}{\sqrt{n}} \quad . \tag{A25}$$

Reference Atlas[2] or Sirmans and Doviak,[1] for example, where ω is a constant of proportionality (having values close to unity) that depends on such things as the type of radar receiver used, the particular nature of the integration process, etc.

There are two points we wish to emphasize by writing the above equation. The first is that the standard deviation, or other statistical measure of the variance of $\overline{P}_r$ (or $\overline{I}$), will decrease approximately as $n^{-1/2}$ for hydrometeor targets in atmospheric clouds or storms. The second is that Eq. (A25) provides

*Actually, this will differ somewhat, from integrator to integrator, dependent on the details of the input quantization and averaging processes, reference Sirmans and Doviak.[1]

3. Marshall, J.S., and Hitchfield, W. (1953) The interpretation of the fluctuating echo for randomly distributed scatterers, Part I, Can. J. Phys. 31:962-994.

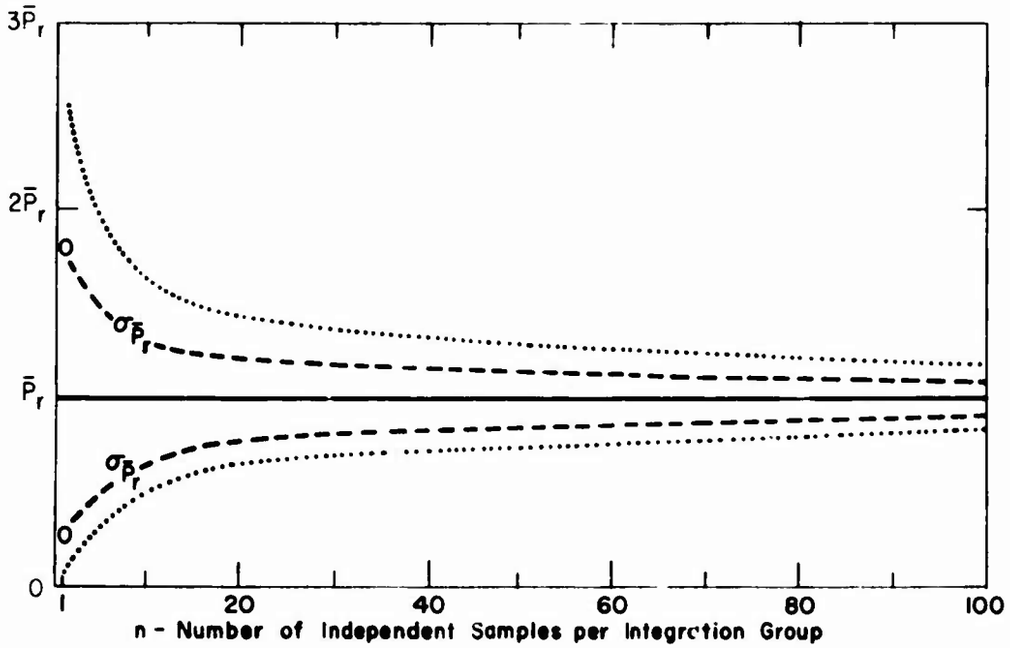

Figure A1. Standard Deviation of the Distribution of Averages of n Independent Values of P_r. The horizontal solid line shows the average corresponding to $n \to \infty$. The dashed isolines labeled $\sigma_{\overline{P}_r}$ show the envelope of the first standard deviation of the $\overline{P}_r$ averages for grouped independent samples containing n samples per group, for n values ranging from 1 to 100. The dotted isolines show the envelope of the second standard deviation. The two open circles show the particular $\sigma_{\overline{P}_{r_1}}$ values, referenced in the text, which pertain to the $\overline{P}_r$ averages for single independent samples. The scale values of the ordinate are arbitrary; they will differ from one averaging or integration situation to another. Derived from Atlas [2]

a means of estimating the uncertainties (indeterminancies) of radar integration data that were acquired for known, or ascertainable, values of n.

To be more specific concerning the latter point, it was demonstrated previously that the number of independent samples for pulse or video integration with a moving antenna was given by Eq. (A24). We may substitute this equation into Eq. (A25), replacing n by n_{i_T}, to obtain

$$\sigma_{\overline{P}_r} \approx \frac{\omega \sigma_{\overline{P}_{r_1}}}{\sqrt{\frac{n_c n_p}{prf}\left(\frac{585}{\lambda} + \frac{\beta}{\omega} + \frac{4|\vec{V}_H|}{h + 2r_0}\right)}} \quad . \tag{A26}$$

This shows that, for any given radar having a particular wavelength λ, beamwidth θ, and pulse repetition frequency (prf), the standard deviation of the $\overline{P}_r$ (or $\overline{\Gamma}$) values measured with a pulse or video integrator will decrease (1) with the number of pulses integrated, that is, with the integration period, see Eq. (A3), (2) with the number of range cells included in the averaging and (3) with the scan rate of the antenna and the wind-transport function [within the scan rate limitations of Eq. (A19)].

If a given radar has a selectable prf, it is likewise apparent from Eqs (A3) and (A26), that since the integration period $\Delta t_I = n_p/\text{prf}$, then the largest selectable prf—when combined with a long integration period (which is a matter of integrator design and/or operational choice)—will tend to minimize the $\sigma_{\overline{P}_r}$ deviations, assuming that the values of the other parameters in Eq. (A26) are held constant. Conversely, the selection of a small prf combined with a short Δt_I will tend to maximize the $\sigma_{\overline{P}_r}$ values. These statements, although true for the restricted, normal range of integrator operation, do have limitations and should not be assumed to hold generally.

Equation (A26) can be employed to estimate the uncertainties, or indeterminancies, of integrator measurements acquired from hydrometeor targets. For example, if $\sigma_{P_{r_1}}$ can be evaluated for single independent samples, and if ω is known, reasonable estimates of $\sigma_{\overline{P}_r}$ can be acquired from Eq. (A26). Alternately, if σ_{P_r} can itself be established for a particular integration situation of known n, then Eq. (A26) can also be solved. These possibilities are merely suggested here and will not be elaborated (see Appendix B for additional discussion). One of the problems involved is that the atmospheric volumes used for such estimates must contain hydrometeors that are relatively homogeneous in type, quantity and size distribution. Otherwise, the $\sigma_{P_{r_1}}$ or $\sigma_{\overline{P}_r}$ values will reflect real atmospheric variability, rather than just the uncertainty values desired.

The work of this appendix is summarized in Section 2.7.4 of the main text.

Appendix B

Parameters Contributing to the Uncertainties of Radar Measurement and Proposed Uncertainty Analysis

The parameters that contribute to the uncertainties of radar measurement may be identified by writing the equations of relationship between the basic measured parameter of the radar, $\overline{P}_r$, and the desired end-product parameters, reflectivity factors Z_W and Z_I, for water and ice hydrometeors.

As noted in Sections 2.7.1 and 2.7.2, the AFCRL integrators employed with the RARF radars basically measure the average power of the backscatter signals received from the hydrometeor particles that exist within the integration volume of the radar beam during the particular period of integration. This average received power, $\overline{P}_r$, is related to the true average received power, $\overline{P}_{r_t}$, as specified by Eq. (43). The integration signal, $\overline{I}$, produced by the video integrator, is related to $\overline{P}_r$ as

$$\overline{I} = c\overline{P}_r r^2 \quad . \tag{B1}$$

See Eq. 51. The volume reflectivity, η, is dependent on $\overline{I}$ in the manner

$$\eta \quad \frac{\overline{I}}{\kappa} . \tag{B2}$$

See Eq. (49). Finally, the end-product parameters of the SAMS radar measurements program, the reflectivity factors Z_W for water hydrometeors and Z_I for

ice hydrometeors, are related to η as specified respectively by Eqs. (57) and (64).

By the successive substitution of Eq. (43) into Eq. (B1), Eq. (B1) into Eq. (B2) and Eq. (B2) into Eq. (57), first, and Eq. (B2) into Eq. (64) second, it is readily demonstrated that

$$Z_W \quad \frac{c\lambda^4 \gamma \overline{P}_{r_t} r^2}{\pi^5 k |K|^2_w} \times 10^{12} \left(\frac{mm^6}{m^3}\right) , \tag{B3}$$

for water hydrometeors, and

$$Z_I \quad \frac{c\lambda^4 \gamma \overline{P}_{r_t} r^2}{\pi^5 k |K|^2_w} \times 10^{12} \left(\frac{mm^6}{m^3}\right) \tag{B4}$$

for ice hydrometeors. The multiplying factor 10^{12} has been incorporated in these equations so that Z_W and Z_I will be given in the conventional units of mm^6/m^3, for λ in cm and r in NM.

Equations (B3) and (B4) show the relationships between Z_W and $\overline{P}_{r_t}$, and Z_I and $\overline{P}_{r_t}$, which contain all of the factors of dependence. These are the factors that are individually subject to uncertainty and that, in their total uncertainty effects, will cause uncertainty of the Z_W and Z_I values for the SAMS missile trajectories. Each of these factors will be discussed, in turn, in the following paragraphs.

The factors r, λ and c are subject to only minor uncertainties and can be regarded as essentially devoid of error contribution. The radar range r, is determinable to at least a tenth of a microsecond in time or 15 m in range distance. The radar wavelength λ, during radar operation, does not vary by more than about 1 or 2 percent. When the video integrator is coupled to the radar receiver, the coupling constant, c, can be set to within at least a tenth of a decibel accuracy, which is about ± 1 percent. These uncertainties are definitely of second order compared to the other uncertainties that enter Eqs. (B3) and (B4).

The numerical values of the averaging factor, γ, used in the computational equations of the main text, stem from the work of Kodaira, [1] Austin and Schaffner, [2] and perhaps others. The values depend on assumptions regarding

---

1. Kodaira, N. (1960) The Characteristics of the Averaged Echo Intensity Received by the Logarithmic I.F. Amplifier, Proceedings 8th Weather Radar Conference, Am. Meteorol Soc., Boston, Massachusetts, pp 255-261.

2. Austin, P.M., and Schaffner, M.R. (1970) Computations and Experiments Relevant to Digital Processing of Weather Radar Echoes, Proceedings 14th Weather Radar Conference, 17-20 November 1970, Tucson, Arizona.

the probability that the average of n independent samples of hydrometeors detected by radar, which have a mean-square-voltage return $\overline{E}^2$ (or average received power $\overline{P}_r$) will exceed a certain threshold level, which lies a dB amount, γ_1, below the true average value $\overline{E}_t^2$ (or $\overline{P}_{rt}$). Thus, γ, or γ_1, depends on the number of independent samples integrated and also depends on the particular types, and instrumental characteristics, of the radar receivers and video integrators employed. The estimation of the assumptive errors involved in the choice of a specific value of γ is, therefore, seen to involve considerable complexity. The errors are probably of the order of ±0.2 to ±1.0 dB and it is apparent that these will be "bias errors", that will act to shift all of the Z_W or Z_I trajectory values either upward or downward by some ±5 to ±23 percent (about an assumed typical value of γ 0.537).

The hydrometeor shape factor k (see Section 2.8) was assumed equal to unity in the present report, both for water hydrometeors and ice hydrometeors. For water, that is water cloud or rain, this means that the water drops are assumed to have spherical shape. Studies have shown that cloud and raindrops up to about 1-mm diameter size are spherical within close tolerance. From the 1 mm size up to the "drop breakup size" of approximately 5 mm, however, the falling drops tend to depart more and more from sphericity and to develop oscillatory characteristics in which their dimensions, vertical versus horizontal, become variable with fall distance. On the average, though, even for these larger droplets, the k 1.0 assumption would appear to hold quite well. For example, Newell and Geotis,[3] from backscatter measurements made with horizontally and vertically polarized radiation, found no discernable differences attributable to shape factor in any hydrometeor region other than the melting zone. (There was a 1 db difference in this zone indicating preferential horizontal orientation.) Other information concerning this subject undoubtedly exists in the literature.

Likewise, the values of the refractive-index-factor, $|K|^2$, for water hydrometeors, are known with considerable precision. The values vary with the radar wavelength, as discussed by Gunn and East,[4] but there is little question about their accuracy and theoretical justification.

For all intents and purposes, then, the k and $|K|^2$ parameters for water hydrometeors may be regarded as devoid of important error contribution to Z_W.

---

3. Newell, R.E., and Goetis, S.G. (1955) Meteorological Measurements With a Radar Provided With Variable Polarization, M.I.T. Dept. of Meteorol. Weather Radar Res., Tech. Note No. 8.

4. Gunn, K.L.S., and East, T.D.R. (1954) The microwave properties of precipitation particles, Quart. J. Roy. Met. Soc. 80:522, (427-8).

In the case of ice hydrometeors, particularly ice crystals, it is not a-priori apparent that the shape factor, k, and the density-modified-refractive-index-factor, $|K'|^2$, are devoid of uncertainties. The particle shapes, except for some grauple particles and hail, are mostly non-spherical. The ice crystals have various needleform, columnar, platelet, dendritic and irregular shapes, and the snow particles are composed of aggregates of such crystals. The $k = 1.0$ assumption, as noted in Section 2.8, is contended to be justified for these non-spherical particles on the basis that they, while falling within the radar pulse volume, or integration volume, are probabilistically likely to have random orientations in space. This assumption, however, at least for the case of a stable atmosphere with little atmospheric turbulence such as would be expected to prevail in the Wallops storms desired for SAMS missile launch purposes, is in conflict with various observational and laboratory findings that ice crystals and single-crystal-snow particles, except for the irregular and dendritic forms, have preferential fall orientations. Thus, it would appear that, although the $k = 1.0$ assumption should be reasonably valid for all types of ice particles under turbulent conditions, it might be questionable for particles with preferred fall-orientations under stable, relatively nonturbulent conditions. The errors would conceivably be as large as a factor of two, in the author's opinion.* Detailed data concerning the horizontally-polarized versus vertically-polarized signal returns from such ice crystals under stable conditions should be acquired to provide the necessary, error-assessment information.

The density-modified-refractive-index-factor $|K'|^2$ for ice hydrometeors, which was assigned the value 0.209 herein and was based on the work of Mason[6] (see Section 2.8), would seem subject to relatively minor uncertainty perhaps of the order of ±4 percent. The cited value was obtained under the assumption that the ratio of the refractive index of ice, K_I, to the density of ice, ρ_I, would be constant for ice of all densities (that is, for ice containing different amounts of entrained air bubbles). The assumption, for single-particle, ice crystals, is quite valid (see Atlas et al[7]) since the values of K_I/ρ_I only vary from 0.46 to 0.50

---

* Based on the work of Atlas et al,[5] concerning scattering from non-spherical particles in the Rayleigh region, also based on the comments of Mason.[6]

5. Atlas, D., Kerker, M., and Hitschfeld, W. (1953) Scattering and attenuation by non-spherical atmospheric particles, J. Atmos. Terr. Phys. 3: 108. (406-13).

6. Mason, B.J. (1971) The Physics of Clouds, Second Edition, Clarendon Press, Oxford, England.

7. Atlas, D., Cunningham, R.M., Donaldson, R.J., Jr., Kantor, G., and Newman, P. (1965) Some aspects of electromagnetic wave propagation, Handbook of Geophysics and Space Environments, 9-1 through 9-26, AFCRL, Bedford, Massachusetts.

for ρ_I values spanning the normally-observed, ice-density range from 0.22 to 0.97 gm cm^{-3}. The approximation is also valid for Rayleigh scattering from snow, since snow may be considered to be a mixture of the two dielectrics, ice and air. The composite K/ρ ratio for such mixture is given by the mass-weighted sum of each substance. Hence, since K/ρ for air is negligible compared to that for ice, the assumptive uncertainties for snow particles are not appreciably larger, theoretically, than for single-particle, ice crystals.

The uncertainties in the system calibration constant, κ, were discussed previously in Section 3.5. The difficulties of assessing the uncertainties were pointed out and methods for acquiring appropriate uncertainty information were suggested. As a first, gross estimate, it was contended that the uncertainties were probably of the order of ±0.5 dB to ±3.5 dB (~ ±12 percent to ±120 percent).* This contention is in reasonable accord with the Stout and Mueller[8] estimation that under ideal, careful conditions of radar calibration, the accuracy is about ±3.0 dB. Mason[6] cites accuracies of approximately ±2 dB. It should be noted that these calibration uncertainties are of "bias type", which, for any given day of radar operation, will cause all of the Z_W or Z_I values for the missile trajectories to be either too large or too small.

To this point, we have considered the uncertainty status of all factors entering Eqs. (B3) and (B4) except that of the basic parameter of measurement, $\overline{P}_{r_t}$. It will be convenient at this time to rewrite Eqs. (B3) and (B4) and make a clear distinction between those parameters which are not subject to important uncertainty and those that are. Thus, Eq. (B3) may be written as

$$Z_W = \frac{c\lambda^4 r^2 \times 10^{12}}{\pi^5 k |K|^2} \times \frac{\gamma \overline{P}_{t_r}}{\kappa}, \tag{B5}$$

where γ, κ and $\overline{P}_{r_t}$ are the uncertain parameters, and Eq. (B4) may be written as

$$Z_I = \frac{c\lambda^4 r^2 \times 10^{12}}{\pi^5 |K|^2} \times \frac{\gamma \overline{P}_{r_t}}{\kappa k}, \tag{B6}$$

where k is an additional factor of uncertainty (for the particular case of ice crystals crystals having preferential fall orientations).

---

*Reference footnote on page 102, concerning percentage uncertainties.

8. Stout, G.E., and Mueller, E.A. (1968) Survey of relationships between rainfall rate and radar reflectivity in the measurement of precipitation, J. Appl. Meteorol. 7:465-74.

The total variation in Z_W resulting from component variation of γ, κ and P_r is

$$dZ_W = \frac{\partial Z_W}{\partial \gamma} d\gamma + \frac{\partial Z_W}{\partial \kappa} d\kappa + \frac{\partial Z_W}{\partial \overline{P}_r} d\overline{P}_{r_t} , \tag{B7}$$

while that for Z_I, for the added component variation of k, is

$$dZ_I = \frac{\partial Z_I}{\partial \gamma} d\gamma + \frac{\partial Z_I}{\partial \kappa} d\kappa + \frac{\partial Z_I}{\partial k} dk + \frac{\partial Z_I}{\partial \overline{P}_r} d\overline{P}_{r_t} . \tag{B8}$$

When the partial derivatives of the above equations are evaluated, from Eqs. (B5) and (B6), we obtain

$$dZ_W = \frac{c\lambda^4 r^2 \times 10^{12}}{\pi^5 k |K|^2_\kappa} \left(\overline{P}_{r_t} d\gamma - \frac{\gamma \overline{P}_{r_t}}{\kappa} d\kappa + \gamma d\overline{P}_{r_t} \right) \tag{B9}$$

and

$$dZ_I = \frac{c\lambda^4 r^2 \times 10^{12}}{\pi^5 k |K'|_\kappa} \left(\overline{P}_{r_t} d\gamma - \frac{\gamma \overline{P}_{r_t}}{\kappa} d\kappa - \frac{\gamma \overline{P}_{r_t}}{k} dk + \gamma d\overline{P}_{r_t} \right) . \tag{B10}$$

The derivatives $d\gamma$, $d\kappa$, dk and $d\overline{P}_{r_t}$ of these equations may be identified and associated with the uncertainty variations of the parameters γ, κ, k and $\overline{P}_{r_t}$. Their total contributions to the uncertainties of the reflectivity factors for water and ice hydrometeors, that is dZ_W and dZ_I, are then specified by Eqs. (B9) and (B10).

We turn, now, to a discussion of the uncertainties, or indeterminancies, of the true received power, $\overline{P}_{r_t}$.

An equation was presented in Appendix A, Eq. (A25), which specified how the standard deviation of the integrated received power would vary (approximately) with the number of independent hydrometeor samples included in the integration. Another equation, Eq. A26, was also written which described how the standard deviation of the received power would vary with the particular characteristics of a given radar and with the integration and wind-translation parameters.

For the purposes of the uncertainty analyses of this appendix, we may assume that the uncertainty parameter $d\overline{P}_{r_t}$, of Eqs. (B9) and (B10), is given approximately by

$$d\overline{P}_{r_t} \cong d\overline{P}_r \cong \sigma_{\overline{P}_r} , \tag{B11}$$

where $\sigma_{\overline{P}_r}$ is as specified by Eq. (A26). This assumption permits Eqs. (B9) and (B10) to be written as

$$dZ_W = \frac{c\lambda^4 r^2 \times 10^{12}}{\pi^5 k |K|^2 \kappa} \left[\overline{P}_{r_t} d\gamma - \frac{\gamma \overline{P}_{r_t}}{\kappa} d\kappa + \sqrt{\frac{\gamma \omega \sigma_{\overline{P}_{r_1}}}{\frac{n_c n_p}{prf} \left(\frac{585}{\lambda} + \frac{\beta}{\theta} + \frac{4|\vec{V}_H|}{h + 2r\theta} \right)}} \right] \quad \text{(B12)}$$

and

$$dZ_I = \frac{c\lambda^4 r^2 \times 10^{12}}{\pi^5 k |K|^2 \kappa} \left[\overline{P}_{r_t} d\gamma - \frac{\gamma \overline{P}_{r_t}}{\kappa} d\kappa - \frac{\gamma \overline{P}_{r_t}}{k} dk \right.$$

$$\left. + \sqrt{\frac{\gamma \omega \sigma_{\overline{P}_{r_1}}}{\frac{n_c n_p}{prf} \left(\frac{585}{\lambda} + \frac{\beta}{\theta} + \frac{4|\vec{V}_H|}{h + 2r\theta} \right)}} \right], \quad \text{(B13)}$$

where $\sigma_{\overline{P}_{r_1}}$, as defined in Appendix A, is the standard deviation of the received power for single independent samples.

These are the final uncertainty equations for dZ_W and dZ_I.*

To illustrate the nature of the uncertainty analyses permitted by these equations, the following example is presented.

Assume that we wish to assess the uncertainties of the Z_W and Z_I values for the missile trajectories that were determined by the FPS-18 radar and integrator of the 1972-73 season of SAMS operations. For this radar and season, $\lambda = 10.7$ cm, $\theta = 0.48^o$, $h = 150$ m, $\gamma = 0.537$ and $c = 8.42 \times 10^{11}$ $mw^{-1} cm^{-1} (NM)^{-2}$, see Tables 3 and 4. The radar calibration constant, κ, for the season had an average value of about $8.0 \cdot 10^{17}$, see Table 9. The integration parameters assumed were $n_p = 256$, $prf = 960$, $\beta = 1^o$ sec, and $\omega = 1.0$. The number of range cells integrated, n_c, is left unspecified at the moment, for uncertainty investigation.

---

*It should be noted that, if frequency diversity is used in the video integration, as planned for the Spandar radar in the 1973-74 season, the number of independent samples integrated will be increased considerably. Such change will affect the last terms of Eqs. (B12) and (B13) and the modifications indicated in Section 3.7.4 will have to be accomplished to obtain new, appropriate, uncertainty equations.

If, in addition to the values of these cited parameters, we presume that the normal, average wind speed in the Wallops storms is $|\vec{V}_H| = 15\ \text{m sec}^{-1}$, the uncertainty equation for water hydrometeors, Eq. (B12), for which k 1.0 and $|K|^2 = 0.93$, reduces to

$$dZ_W = 1.41 \cdot 10^7 r^2 \left[\overline{P}_{r_t} d\gamma - 6.71 \cdot 10^{-19} \overline{P}_{r_t} dk + \frac{0.537\, \sigma_{\overline{P}_{r_1}}}{\sqrt{0.267\, n_c \left(56.7 + \frac{60}{150 + 16.7r}\right)}} \right] \quad \text{(B14)}$$

for r specified in km and $\overline{P}_{r_t}$ in mw.

For snow hydrometeors, or for ice crystals that do not have preferred fall orientation, for which k 1.0, $|K|^2$ 0.209, and dk ~ 0, the uncertainty Eq. (B13) becomes

$$dZ_I \quad 6.28 \cdot 10^7 r^2 \left[\overline{P}_{r_t} d\gamma - 6.71 \cdot 10^{-19} \overline{P}_{r_t} dk + \frac{0.537\, \sigma_{\overline{P}_{r_1}}}{\sqrt{0.267\, n_c \left(56.7 + \frac{60}{150 + 16.7r}\right)}} \right] \quad \text{(B15)}$$

For that special class of ice crystals which do have preferred fall orientation, that is, for which dk ≠ 0, Eq. (B13) reduces to

$$dZ_I \quad 6.28 \cdot 10^7 \frac{r^2}{k} \left[\overline{P}_{r_t} d\gamma - 6.71 \cdot 10^{-19} \overline{P}_{r_t} dk - \frac{0.537}{k} \overline{P}_{r_t} dk + \frac{0.537\, \sigma_{\overline{P}_{r_1}}}{\sqrt{0.267\, n_c \left(56.7 + \frac{60}{150 + 16.7r}\right)}} \right] \quad \text{(B16)}$$

The individual term contributions to the total uncertainties, dZ_W and dZ_I, are assessed in Tables B1 through B4 for four hydrometeor types: (1) rain, (2) snow, (3) ice crystals without preferential fall orientation, and (4) ice crystals with preferential fall orientation.

Table B1. Estimated Term Contributions and Total Uncertainties of the Radar Reflectivity Factor for Rain, as Assessed From Eq. (B14)

Radar Range r		Integration Signal L	Corresponding		Uncertainty Contributions of Terms of Equation B14							Approximate Total Uncertainty (P. E. Summation) dZ_w	
					First Term		Second Term		Third Term				
			$\bar{P}_{r_t}$	Z_w	Assumed d_γ	Uncertainty Contribution to dZ_w	Assumed d_κ	Uncertainty Contribution to dZ_w	Assumed $\sigma_{\bar{P}_{r_I}}$	n_c	Uncertainty Contribution to dZ_w		
(NM)	(km)	(dB)	(mW)	(mm^6m^{-3})		(mm^6m^{-3})		(mm^6m^{-3})			(mm^6m^{-3})	(mm^6m^{-3})	(percent)
5	9.27	80	4.75×10^{-6}	3092	±0.062	±357	$\pm 3.87 \times 10^{17}$	±1468	$\pm 2.35 \cdot 10^{-5}$ (±10 dB)	1	±3923	±4204	±136*
									$\pm 2.35 \cdot 10^{-5}$ (±10 dB)	8	±1387	±2051	±66.3
									$\pm 6.75 \cdot 10^{-6}$ (±5 dB)	1	±1127	±1885	±61.0
									$\pm 6.75 \cdot 10^{-6}$ (±5 dB)	8	± 398	±1562	±50.5
5	9.27	60	4.75×10^{-8}	30.92	±0.062	±3.57	$\pm 3.8 \times 10^{17}$	±14.68	$\pm 2.35 \cdot 10^{-7}$ (±10 dB)	1	±39.23	±42.03	±136
									$\pm 2.35 \cdot 10^{-7}$ (±10 dB)	8	±13.87	±20.51	±66.3
									$\pm 6.75 \cdot 10^{-8}$ (±5 dB)	1	±11.27	±18.84	±61.0
									$\pm 6.75 \cdot 10^{-8}$ (±5 dB)	8	± 3.98	±15.62	±50.5
10	18.53	80	1.19×10^{-6}	3092	±0.062	±357	$\pm 3.8 \times 10^{17}$	±1468	$\pm 5.9 \cdot 10^{-6}$ (±10 dB)	1	±3938	±4218	±136
									$\pm 5.9 \cdot 10^{-6}$ (±10 dB)	8	±1392	±2054	±66.4
									$\pm 1.7 \cdot 10^{-6}$ (±5 dB)	1	±1135	±1889	±61.1
									$\pm 1.7 \cdot 10^{-6}$ (±5 dB)	8	±401	±1563	±50.5
10	18.53	60	$1.19 \cdot 10^{-8}$	30.92	±0.062	±3.57	$\pm 3.8 \times 10^{17}$	±14.68	$\pm 5.9 \cdot 10^{-8}$ (±10 dB)	1	±39.38	±42.20	±136
									$\pm 5.9 \cdot 10^{-8}$ (±10 dB)	8	±13.92	±20.54	±66.4
									$\pm 1.7 \cdot 10^{-8}$ (±5 dB)	1	±11.35	±18.90	±61.1
									$\pm 1.7 \cdot 10^{-8}$ (±5 dB)	8	± 4.01	±15.63	±50.5

*These percentage uncertainties are presented for qualitative, comparison purposes only. See footnote comment on page 102 concerning percentage uncertainties.

Table B2. Estimated Term Contributions and Total Uncertainties of the Radar Reflectivity Factor for Snow, as Assessed From Eq. (B15)

Radar Range r		Integration Signal L_t	Corresponding		Uncertainty Contributions of Terms of Equation B15							Approximate Total Uncertainty (P. E. Summation) dZ_1	
					First Term		Second Term		Third Term				
(NM)	(km)	(dB)	$\bar{P}_{r_t}$ (mW)	Z_1 (mm^6m^{-3})	Assumed $d\gamma$	Uncertainty Contribution to dZ_1 (mm^6m^{-3})	Assumed $d\alpha$	Uncertainty Contribution to dZ_1 (mm^6m^{-3})	Assumed $\sigma_{\bar{P}_{r_1}}$	n_c	Uncertainty Contribution to dZ_1 (mm^6m^{-3})	(mm^6m^{-3})	(percent)
5	9.27	80	4.75×10^{-6}	13,760	±0.062	±1590	$\pm 3.8 \times 10^{17}$	±6540	$\pm 2.35 \times 10^{-7}$ (±10 dB)	1	±17,470	±18,725	±136*
									$\pm 2.35 \times 10^{-7}$ (±10 dB)	8	±6180	±9136	±66.4
									$\pm 0.75 \times 10^{-6}$ (±5 dB)	1	±5020	±8396	±61.0
									$\pm 0.75 \times 10^{-6}$ (±5 dB)	8	±1775	±8960	±50.6
5	9.27	60	4.75×10^{-8}	137.6	±0.062	±15.90	$\pm 3.8 \times 10^{17}$	±65.40	$\pm 2.35 \times 10^{-7}$ (±10 dB)	1	±174.7	±187.7	±136
									$\pm 2.35 \times 10^{-7}$ (±10 dB)	8	±61.80	± 91.4	±66.4
									$\pm 0.75 \times 10^{-8}$ (±5 dB)	1	±50.20	± 84.0	±61.0
									$\pm 0.75 \times 10^{-8}$ (±5 dB)	8	±17.75	± 69.6	±50.6
10	18.53	80	1.19×10^{-6}	13,760	±0.062	±1590	$\pm 3.8 \times 10^{17}$	±6540	$\pm 5.9 \times 10^{-6}$ (±10 dB)	1	±17,540	±18,785	±136
									$\pm 5.9 \times 10^{-6}$ (±10 dB)	8	±6200	±9152	±66.5
									$\pm 1.7 \times 10^{-6}$ (±5 dB)	1	5050	±8420	±61.2
									$\pm 1.7 \times 10^{-6}$ (±5 dB)	8	±1790	±6965	±50.6
10	18.53	60	1.19×10^{-8}	137.6	±0.062	±15.90	$\pm 3.8 \times 10^{17}$	±65.40	$\pm 5.9 \times 10^{-8}$ (±10 dB)	1	±175.4	±187.8	±136
									$\pm 5.9 \times 10^{-8}$ (±10 dB)	8	±62.0	±91.5	±66.5
									$\pm 1.7 \times 10^{-8}$ (±5 dB)	1	±50.5	±84.2	±61.2
									$\pm 1.7 \times 10^{-8}$ (±5 dB)	8	±17.9	±69.6	±50.6

*These percentage uncertainties are presented for qualitative, comparison purposes only. See footnote comment on page 102 concerning percentage uncertainties.

Table B3. Estimated Term Contributions and Total Uncertainties of the Radar Reflectivity Factor for Ice Crystals Without Preferential Fall Orientations as Assessed From Eq. (B15)

Radar Range r (NM)	Radar Range r (km)	Integration Signal $\perp$ (dB)	Corresponding P_{r_t} (mW)	Corresponding Z_1 ($mm^6 m^{-3}$)	Uncertainty Contributions of Terms of Equation B15: First Term, Assumed $d\gamma$	First Term, Uncertainty Contribution to dZ_1 ($mm^6 m^{-3}$)	Second Term, Assumed $d\alpha$	Second Term, Uncertainty Contribution to dZ_1 ($mm^6 m^{-3}$)	Third Term, Assumed $\sigma_{P_{r_1}}$	n_c	Third Term, Uncertainty Contribution to dZ_1 ($mm^6 m^{-3}$)	Approximate Total Uncertainty (P. E. Summation) dZ_1 ($mm^6 m^{-3}$)	Approximate Total Uncertainty (P. E. Summation) dZ_1 (percent)
5	9.27	50	4.75×10^{-9}	13.76	±0.062	±1.59	$\pm 3.8 \times 10^{17}$	±6.54	$\pm 2.35 \cdot 10^{-8}$ (±10 dB)	1	±17.46	±18.72	±136*
									$\pm 2.35 \cdot 10^{-8}$ (±10 dB)	8	± 6.18	± 9.14	±66.4
									$\pm 6.75 \cdot 10^{-9}$ (±5 dB)	1	± 5.02	± 8.40	±61.0
									$\pm 6.75 \cdot 10^{-9}$ (±5 dB)	8	± 1.77	± 6.96	±50.6
5	9.27	40	4.75×10^{-10}	1.38	±0.062	±0.16	$\pm 3.8 \times 10^{17}$	±0.65	$\pm 2.35 \cdot 10^{-9}$ (±10 dB)	1	± 1.75	± 1.87	±136
									$\pm 2.35 \cdot 10^{-9}$ (±10 dB)	8	± 0.62	± 0.91	±66.4
									$\pm 6.75 \cdot 10^{-10}$ (±5 dB)	1	± 0.50	± 0.84	±61.0
									$\pm 6.75 \cdot 10^{-10}$ (±5 dB)	8	± 0.18	± 0.70	±50.6
10	18.53	50	1.19×10^{-9}	13.76	±0.062	±1.59	$\pm 3.8 \times 10^{17}$	±6.54	$\pm 5.9 \cdot 10^{-9}$ (±10 dB)	1	±17.47	±18.72	±136
									$\pm 5.9 \cdot 10^{-9}$ (±10 dB)	8	± 6.18	± 9.14	±66.4
									$\pm 1.7 \cdot 10^{-9}$ (±5 dB)	1	± 5.02	± 8.40	±61.0
									$\pm 1.7 \cdot 10^{-9}$ (±5 dB)	8	± 1.77	± 6.96	±50.6
10	18.53	40	1.19×10^{-10}	1.38	±0.062	±0.16	$\pm 3.8 \times 10^{17}$	±0.65	$\pm 5.9 \cdot 10^{-10}$ (±10 dB)	1	± 1.75	± 1.87	±136
									$\pm 5.9 \cdot 10^{-10}$ (±10 dB)	8	± 0.62	± 0.91	±66.4
									$\pm 1.7 \cdot 10^{-10}$ (±5 dB)	1	± 0.50	± 0.84	±61.0
									$\pm 1.7 \cdot 10^{-10}$ (±5 dB)	8	± 0.18	± 0.70	±50.6

These percentage uncertainties are presented for qualitative, comparison purposes only. See footnote comment on page 102 concerning percentage uncertainties.

Table B4. Estimated Term Contributions and Total Uncertainties of the Radar Reflectivity Factor for Ice Crystals With Preferential Fall Orientation, as Assessed From Eq. (B16)

Radar Range r		Integration Signal L	Corresponding		Uncertainty Contributions of Terms of Equation B16									Approximate Total Uncertainty (P. E. Summation) dZ_1	
					First Term		Second Term		Third Term		Fourth Term				
					Assumed	Uncertainty Contribution to dZ_1	Assumed	Uncertainty Contribution to dZ_1	Assumed	Uncertainty Contribution to dZ_1	Assumed		Uncertainty Contribution to dZ_1		
(NM)	(km)	(dB)	$\bar{P}_{r_t}$ (mW)	Z_1 ($mm^6 m^{-3}$)	$d\gamma$	($mm^6 m^{-3}$)	$d\alpha$	($mm^6 m^{-3}$)	$d\alpha$	($mm^6 m^{-3}$)	$\sigma_{\bar{P}_{r_1}}$	n_c	($mm^6 m^{-3}$)	($mm^6 m^{-3}$)	(percent)
5	9.27	50	4.75×10^{-9}	13.76	±0.062	±1.59	$\pm 3.8 \times 10^{17}$	±6.54	±0.48	±6.60	$\pm 2.35 \times 10^{-8}$ (±10 dB)	1	±17.46	±19.85	±144*
											$\pm 2.35 \times 10^{-8}$ (±10 dB)	8	± 6.18	±11.27	±81.9
											$\pm 6.75 \times 10^{-9}$ (±5 dB)	1	± 5.02	±10.68	±77.6
											$\pm 6.75 \times 10^{-9}$ (±5 dB)	8	± 1.77	± 9.59	±69.7
5	9.27	40	4.75×10^{-10}	1.38	±0.062	±0.16	$\pm 3.8 \times 10^{17}$	±0.65	±0.48	±0.66	$\pm 2.35 \times 10^{-9}$ (±10 dB)	1	± 1.75	± 1.99	±144
											$\pm 2.35 \times 10^{-9}$ (±10 dB)	8	± 0.62	± 1.13	±81.9
											$\pm 6.75 \times 10^{-10}$ (±5 dB)	1	± 0.50	± 1.07	±77.6
											$\pm 6.75 \times 10^{-10}$ (±5 dB)	8	± 0.18	± 0.96	±69.7
10	18.53	50	1.19×10^{-9}	13.76	±0.062	±1.59	$\pm 3.8 \times 10^{17}$	±6.54	±0.48	±6.60	$\pm 5.9 \times 10^{-9}$ (±10 dB)	1	±17.47	±19.85	±144
											$\pm 5.9 \times 10^{-9}$ (±10 dB)	8	± 6.18	±11.27	±81.9
											$\pm 1.70 \times 10^{-9}$ (±5 dB)	1	± 5.02	±10.68	±77.6
											$\pm 1.70 \times 10^{-9}$ (±5 dB)	8	± 1.77	± 9.43	±68.5
10	18.53	40	1.19×10^{-10}	1.38	±0.062	±0.16	$\pm 3.8 \times 10^{17}$	±0.65	±0.48	±0.66	$\pm 5.90 \times 10^{-10}$ (10 dB	1	± 1.75	± 1.99	±144
											$\pm 5.90 \times 10^{-10}$ (10 dB)	8	± 0.62	± 1.13	±81.9
											$\pm 1.70 \times 10^{-10}$ (5 dB)	1	± 0.50	± 1.07	±77.6
											$\pm 1.70 \times 10^{-10}$ (±5 dB)	8	± 0.18	± 0.96	±69.7

*These percentage uncertainties are presented for qualitative, comparison purposes only. See footnote comment on page 102 concerning percentage uncertainties.

The equations are evaluated for two radar ranges, r = 5 NM and r = 10 NM, which correspond approximately to the mid-range and extreme range of the missile-trajectory measurements of the 1970-73 seasons. Two values of the integration signal level, $\underline{\bar{I}}$, are specified in each table which span the normally-observed $\underline{\bar{I}}$ values of the particular hydrometeor type in the Wallops storms. The corresponding $\bar{P}_{r_t}$ and Z_W, or Z_I, values are indicated which were computed from Eq. (51) and Eqs. (B3) and (B4).

The assumptions about the mean values and uncertainties of the independent parameters of Eqs. (B14) through (B16) are consistent with the previous text discussion of this appendix. Specifically, it was assumed:

(1) That the averaging factor, γ, is uncertain to ±0.5 dB, giving $d\gamma \simeq \pm 0.062$ about an average γ of 0.537.

(2) That the calibration constant, κ, is uncertain to ±2.0 dB, giving $d\kappa \simeq 3.8 \times 10^{17}$ about an average κ of 8.0×10^{17}.

(3) That the particle shape factor, k, is devoid of uncertainty for rain, snow and ice crystals without preferential fall orientation; but that it is uncertain to ±2.0 dB for ice crystals with preferential fall orientation under stable atmospheric conditions, giving $dk \simeq \pm 0.48$ about an average k of unity.

(4) That the standard deviation of the integrated received power for single independent samples, $\sigma\bar{P}_{r_1}$, is uncertain to ±10 dB, as the first assumption indicated in the tables, and is uncertain to ±5 dB, as the second assumption indicated to the tables; the uncertainties being with respect to the $\bar{P}_{r_t}$ values shown in the third columns.

The table computations were also performed for two different values of range-cell integration, for single range cells, $n_c = 1$, and for eight cell integration, $n_c = 8$. Single range-cell integration was used with the FPS-18 radar in the 1970-71 season; eight range-cell integration was used in the 1971-73 seasons.

The estimated total uncertainties, dZ_W (or dZ_I) of the next to the last columns of Tables B1 through B4 were computed as the probable error (P.E.) summation of the separate term contributions. Actually, for any given period and day of SAMS radar measurements at Wallops Island, the uncertainty factors $d\gamma$ and $d\kappa$ will impose bias errors on the measurements. But, since we cannot assume a-priori knowledge of the signs of these factors in the table-estimations herein, they are treated as random uncertainties and summed in the P.E. fashion.

The table results reveal that the percent uncertainties of Z_W (or Z_I) vary from about ±51 percent to ±136 percent, for rain, snow and ice crystals without

preferential fall orientation, and from about ±70 percent to ±144 percent, for ice crystals with presumed, preferential fall orientation.*

The percent uncertainties for $n_c = 8$ are seen to be some 60 percent to 70 percent smaller than those for $n_c = 1$, in the case of $\sigma_{P_{r_1}} = \pm 10$dB, and some 10 to 11 percent smaller, in the case of $\sigma_{P_{r_1}} = \pm 5$dB.

It should be reiterated that Tables B1 through B4 are presented primarily to illustrate the techniques of uncertainty analyses based on Eqs. (B12) and (B13). The particular table values are merely first, gross estimates of possibility. For any refined uncertainty-assessment, specific data will have to be acquired for each of the Wallops storms, concerning the values of the independent parameters that enter Eqs. (B12) and (B13).

Note Added Following Manuscript Completion

The careful reader will note that the $\bar{P}_{r_t}$ values of Tables B1 through B4 differ somewhat from those specified by the equation

$$\bar{P}_{r_t} = \frac{\bar{I}}{c\gamma r^2}, \tag{B17}$$

which stems from the combination of Eq. (43) and Eq. (B1). The $\bar{P}_{r_t}$ values of the tables should have been computed from the table $\bar{I}$ values using this above equation (with appropriate dB to absolute conversion). In actual fact, however, they were inadvertently computed from the relationship

$$\bar{P}_{r_t} = \frac{\bar{I}}{c r^2}, \tag{B18}$$

which neglects the γ factor of Eq. (B17).

The effect of this error on the final uncertainty values of the tables is rather slight and inconsequential, particularly in view of the fact that the table uncertainties are merely gross estimates.

---

*Although it is convenient to cite percentage uncertainties for qualitative comparison purposes, it should be noted that large uncertainties, such as the above, which are expressed in percent, are highly non-symmetric in their positive versus their negative values. For example, the positive numerical value can exceed 100 but the negative numerical value cannot. The meaningful uncertainty values of Tables B1 through B4 are the dZ values of the next to the last columns, the percent uncertainty values of the last columns are merely indicative and must be interpreted with care.

References

1. Kodaira, N. (1960) The Characteristics of the Averaged Echo Intensity Received by the Logarithmic I.F. Amplifier, Proceedings 8th Weather Radar Conference, Am. Meteorol. Soc., Boston, Massachusetts, pp 255-261.

2. Austin, P.M., and Schaffner, M.R. (1970) Computations and Experiments Relevant to Digital Processing of Weather Radar Echoes, Proceedings 14th Weather Radar Conference, 17-20 November 1970, Tucson, Arizona.

3. Newell, R.E., and Geotis, S.G. (1955) Meteorological Measurements With a Radar Provided With Variable Polarization, M.I.T. Dept. of Meteorol. Weather Radar Res., Tech. Note No. 8.

4. Gunn, K.L.S., and East, T.D.R. (1954) The microwave properties of precipitation particles, Quart. J. Roy. Met. Soc. 80:522. (427-8).

5. Atlas, D., Kerker, M., and Hitschfeld, W. (1953) Scattering and attenuation by non-spherical atmospheric particles, J. Atmos. Terr. Phys. 3:108. (466-13).

6. Mason, B.J. (1971) The Physics of Clouds, Second Edition, Clarendon Press, Oxford, England.

7. Atlas, D., Cunningham, R.M., Donaldson, R.J., Jr., Kantor, G., and Newman, P. (1965) Some aspects of electromagnetic wave propagation, Handbook of Geophysics and Space Environments, 9-1 through 9-26, AFCRL, Bedford, Massachusetts.

8. Stout, G.E., and Mueller, F.A. (1968) Survey of relationships between rainfall rate and radar reflectivity in the measurement of precipitation, J. Appl. Meteorol. 7:465-74.

List of Symbols

Arabic Symbols

a	decimal attenuation, per unit path length
A	attenuation factor
A_e	effective antenna area
A_p	actual cross-sectional area of parabolic antenna
A_s	sampling area of disdrometer instrument
A_t	geometric cross-section of a scattering target
c	coupling constant
C	calibrated constant of the radar equation pertaining to hydrometeor targets with video integration
C_r	constant of reference performance for the radar equation pertaining to hydrometeor targets with video integration
D	diameter of water droplets
D_e	equivalent, melted diameter of ice crystal or snow particles
D_I	physical measure of the actual size of ice crystals or snow particles
dB	decibel
dBm	decibels below 1 milliwatt, of reference power

$\bar{E}^2$	mean square voltage amplitude
G_r	gain of a receiving antenna
G_t	gain of a transmitting antenna
h	pulse length, in length units
h'	pulse duration, or "pulse length" in time units
$\bar{I}$	integration signal, from video integrator
$\underline{\bar{I}}$	10 log $\bar{I}$, that is, decibel value of $\bar{I}$
$\bar{I}^*$	reference integration signal, of threshold setting
k	shape factor, for hydrometeor particles
k'	microwave absorption coefficient for water
K_a	antenna calibration constant, of "pattern function" equation
K_o	antenna calibration constant, of "effective area" equation
$\lvert K \rvert^2$	refractive index factor, for water hydrometeors
$\lvert K' \rvert^2$	density-normalized refractive index factor, for ice hydrometeors
k_r	sphere calibration constant of radar reference performance
k_s	sphere calibration constant of actual radar performance
$\underline{k_s}$	10 log k_s, that is, decibel value of k_s
L	radar system-loss-factor, as specifically defined in the text
M	precipitation liquid water content
n	number of independent samples, general
n_c	number of range cells included in pulse or video integration
n_i	number of independent samples, in the case of a stationary antenna and no wind
$n_{i_{mw}}$	number of independent samples, with antenna motion and wind
n_{i_T}	total number of independent samples included in the pulse or video integration
n_p	number of radar pulses per integration period
N	number of hydrometeor particles per unit volume
N_f	number of hydrometeor particles per unit area per unit time
NM	nautical miles

P_r	received power
$\overline{P}_r$	pulse-integrated received-power
$\overline{P}_{r_t}$	true pulse-integrated received-power
$\overline{P}_{r_{min}}$	minimum, integrated-received-power, of threshold setting for the video integrator
P_t	transmitted power
prf	pulse repetition frequency
R	rainfall rate
R_T	wind transport rate, of hydrometeors into radar range cell
r	radar range
r	correlation coefficient
S	power density in space, or field strength
S_B	beam shape factor, of Probert-Jones
t	time
Δt	fundamental time resolution of the radar
Δt_I	time resolution with pulse or video integration
U	units conversion factor for radar equation for hydrometeor targets
U_s	units conversion factor for radar equation for single targets
v_p	velocity of microwave propagation (3.0×10^{10} cm sec^{-1})
V	pulse volume
V_I	integration volume, for pulse or video integration
$\lvert\vec{V}_H\rvert$	magnitude, or speed, of the horizontal wind vector
z	circuit impedance
Z	radar reflectivity factor, general
Z_W	radar reflectivity factor for water hydrometeors, determined from radar measurements
Z_{W_D}	radar reflectivity factor for water hydrometeors, determined from surface disdrometer measurements
Z_I	radar reflectivity factor for ice hydrometeors

Greek Symbols

α	wavelength dependent parameter entering the calibration equation of the disdrometer method
β	angular scan rate of the antenna
γ	averaging factor, relating mean square voltage amplitude, measured by pulse or video integrator, to average received power
ϵ	dielectric constant, for hydrometeor particles
η	volume reflectivity
$\overline{\eta}$	average volume reflectivity, as measured with a video integrator
θ	antenna beamwidth, for parabolic antenna
κ	radar calibration constant, for disdrometer method of calibration
$\underline{\kappa}$	10 log κ, that is, decibel value of κ
$\underline{\kappa}_m$	the mean value of $\underline{\kappa}$, determined from disdrometer calibration
λ	radar wavelength
ν	number of radar pulses per independent sample per integration period
ρ_I	density of ice
ρ_t	reflectivity of scattering particles for microwaves
ρ_w	density of water
σ	back scattering cross section of radar targets
$\sigma_{\overline{P}_r}$	standard deviation of pulse or video integrated received power for any given number, n, independent samples
$\sigma_{\overline{P}_{r_1}}$	standard deviation of pulse or video integrated received power for single independent samples
τ	"reshuffling time", or time required for hydrometeors in the radar pulse volume to redistribute themselves sufficiently to give non-autocorrelated, independent data
ψ	factor specifying fraction of radar pulse volume filled with scatterers
ω	constant of proportionality in standard deviation versus number of independent samples equation
Ω	general symbol for solid angle

Other Symbols

$\underline{\ }$	when used to "underline" any given Arabic or Greek symbol, represents the decibel equivalent value of the parameter. For example, $\underline{X} = 10 \log X$.

★ U.S. GOVERNMENT PRINTING OFFICE: 1974 704-205 58